Inaugural dissertation

for

obtaining the doctoral degree

of the

Combined Faculty of Mathematics, Engineering and Natural Sciences

of the

Ruprecht-Karls-University

Heidelberg, Germany

Presented by

Marianne Papagrigorakes

(**2023**, MSc Biochemistry and Molecular Biology)

born in Hamburg, Germany

Oral examination: 20.03.2023

Tools to study cytoadhesion of *P. falciparum*-infected erythrocytes under flow

Referees:

Prof. Dr. Michael Lanzer

Prof. Dr. Ulrich Schwarz

Ich erkläre hiermit, dass ich die vorliegende Doktorarbeit selbständig unter Anleitung verfasst und keine anderen als die angegebenen Quellen und Hilfsmittel benutzt habe. Ich erkläre hiermit, dass ich an keiner anderen Stelle ein Prüfungsverfahren beantragt bzw. die Dissertation in dieser oder anderer Form bereits anderweitig als Prüfungsarbeit verwendet oder einer anderen Fakultät als Dissertation vorgelegt habe. Die vorliegende Arbeit wurde am Department für Infektiologie, Abteilung Parasitologie des Universitätsklinikum Heidelberg in der Zeit von November 2018 bis Dezember 2022 unter der Leitung von Prof. Dr. Michael Lanzer ausgeführt.

....	....
Datum	Marianne Papagrigorakes

Acknowledgements

I would like to sincerely thank Prof. Dr. Michael Lanzer for providing me with the tools and opportunities to grow and learn and for opening up his lab doors to me. I greatly appreciate the support, guidance, suggestions and time spent navigating me through such a rich and interesting topic.

I would also like to thank the members of my TAC committee, Prof. Dr. Ulrich Schwarz, Dr. Dr. Ada-Cavalcanti Adams and Dr. Dimitris Missirlis for their valuable feedback during our yearly meetings. I am also thankful to Prof. Dr. F. Nina Papavasiliou for participating in my PhD examination committee.

My sincere gratitude also goes to all the collaborator scientists, whose contributions were essential for the development of this work. Big thanks to Dr. Pintu Patras, for providing the analysis script for my data and all the discussions, help and advice that he offered. My sincere gratitude also goes to Dr. Dimitris Missirlis, for his mentoring, patience, dedication and sharing of his expertise. A great big thanks also to Dr. Anil Dasanna for his excellent scientific ideas,discussions and keen insight that supported me during this time. I am extremely grateful to Dr.Dr. Ada Cavalcanti-Adams for all the support, discussions and feedback, as well as opening up her lab doors for me. Thanks to Federica Penarola and Joel Christian for all the brainstorming, discussions, technique teachings and help. Thank you to Prof. Dr. Motomu Tanaka for allowing me usage of his lab and microscope and for the discussions and feedback. Thank you to Judith Thoma for introducing me to RICM and all the hours spent in cheerful company during measurements. Thanks to Dr. Benjamin Fröhlich for introducing me to flow chamber measurements and to Maya Harms for her dedication and hard work.

Thanks to Dr. Cecilia Sanchez for her help with different techniques and feedback. Thanks to Prof. Dr. Alexandra Rowe, Prof. Dr. Alister Craig,Dr. Benoit Gamain and Jean-Philippe Semblat for all the help, feedback and materials provided to me. Special thanks to Dr. Sylvia Olberg for introducing me to TIRF microscopy and for her troubleshooting assistance.

I would also like to thank all members, current and past, of the department of Parasitology that helped me, discussed with me, provided a friendly atmosphere and supported me all this time. Especially, thanks to Romina Celada, Fiona Berger, Guillermo Gomez, Violetta Pancakova, Monika Jankovska-Dölken, Christine Lansche, Marina Müller and Sophia Frangos. Thanks to Miriam Griesheimer and Sandra Niebel, I would be lost without your support and cheerful disposition. Thanks to HBIGS and SFB1129 for all the training opportunities, guidance and support.

Last but not least, an enormous thanks to my family and friends and especially my husband Jochen for the unwavering support, encouragement and help.

Table of Contents

List of abbreviations

AFM	Atomic force microscopy
APTES	3-Triethoxysilylpropylamine
BSA	Bovine serum albumin
cDNA	complementary DNA
CHO	Chinese hamster Ovary cells/ aldehyde
CIDR	Cysteine-rich interdomain region
CO_2	Carbon dioxide
CSA	chondroitin 4-sulfate
C-terminal	carboxy terminal
DBL	Duffy-binding like
ddH_2O	distilled water
DIC	Differential interface contrast
DNA	Deoxyribonucleic acid
DNase	Deoxyribonuclease
dNTP	Deoxyribonucleoside triphosphate
dsDNA	Double stranded DNA
EDTA	Ethylenediaminetetraacetic acid
ELISA	Enzyme linked immunosorbent assay
Em	Emission
EPCR	Endothelial protein C receptor
Ex	Excitation
FACS	Fluorescence activated cell sorter
FCR3	*P. falciparum* adapted lab strain
FCS	Foetal calf serum
gDNA	Genomic DNA
HA	Hyaluronic acid
Hb	Haemoglobin
HDMEC	Human dermal microvascular endothelial cells
HEPES	2-[4-(2-hydroxyethyl)piperazin-1-yl] ethanesulfonic acid
hpi	hours post invasion
ICAM	Intracellular adhesion molecule
IF	Immunofluorescence
IFN	Interferon
Ig	Immunoglobulin
iRBC	Infected red blood cell
KAHRP	Knob associated histidine rich protein
MACS	Magnetic activated cell sorter
MAL	Maleimide
mRNA	Messenger RNA
NHS	N-hydroxysuccinimide
NO	Nitric oxide
NPP	New permeation pathways
N-terminus	Amino-terminus
NTS	N-terminal sequence
O_2	Oxygen
OD	Optical density
P.	Plasmodium
PBS	Phospahte buffer saline

PCR	Polymerase chain reaction
PECAM	Platelet endothelial cell adhesion molecule
PEG$_{5000}$	Polyethylene glycol (5000 kDa long)
PFA	Paraformaldehyde
PfEMP1	*P. falciparum* erythrocyte membrane protein
pH	Power of hydrogen
PSGL-1	P-selectin glycoprotein ligand 1
RBC	Red blood cell
RICM	Reflection Interference Contrast Microscopy
RNA	Ribonucleic acid
Rpm	Revolutions per minute
RPMI	Roswell Park Memorial Institute
RT	Room temperature
SMCC	Succinimidyl 4-(N-maleimidomethyl)cyclohexane-1-carboxylate
SMFS	Single molecule force spectroscopy
SD	Standard deviation
SDS	Sodium dodecyl sulfate
SEM	Standard error of mean
SVS	Succinimidyl valerate
TIRF	Total Internal Reflection Fluorescence
TAE	Tris-acetate EDTA
Taq	Thermus aquaticus
TM	Transmembrane
TNF-α	Tumour necrosis factor alpha
Tris	Tris(hydroxymethyl-)aminomethane
Ups	Upstream promoter sequence
uRBC	Uninfected red blood cell
UV	Ultraviolet
v/v	Volume per volume
VCAM-1	Vascular cell adhesion molecule 1
w/v	Weight per volume
WBC	White blood cell
WHO	World health organization

Measuring units and symbols

%	Percent
°C	Degree Celsius
∞	Infinite
A	Ampere or Absorbance
au	Arbitrary units
cm	Centimeter
Da	Dalton
g	Gram
h	Hour
k	Kilo
kb	Kilobasepair
L	Litre
M	Molar
m	Meter or milli
min	Minute
n	Nano
N	Newton
p	Pico
Pa	Pascal
s	Second
U	Unit(s)
V	Volt
x g	Times gravitational force
α	Alpha or anti
β	Beta
Δ	Delta or difference or change
κ	Kappa
µ	Micro
τ	Tau or sheer stress

Summary

Plasmodium falciparum infected erythrocytes are able to bind to a multitude of extracellular receptors through adhesins expressed on their membrane. The molecular interactions involved in parasite binding to these receptors are only partly understood, although the trait itself is well-known and used as an early indicator of severe malaria diagnosis and progress of infection.

Binding to the microvasculature of blood vessels or the intervillous spaces of the placenta, ensures the survival of the parasite as it avoids splenic clearance in the later stages of maturation. In this thesis, the importance of sheer flow and cell morphology in binding dynamics of parasitized erythrocytes is further highlighted. While static adhesion assays would showcase similar amounts of cells adhering in different maturation stages, when observed in flow, this picture changes drastically. Trophozoite stage parasites seem to bind less frequently but more efficiently onto the simulated endothelium. In the last stage of maturation, schizont stage parasites alter the cell morphology to such an extent that adhesion is more likely but with less contact area and density of involved receptors. Changes in the membrane morphology between AA and AS erythrocytes also underline the significance of receptor presentation and accessibility influencing binding efficiency.

The effects of a *P. falciparum* infection during primigravida are threatening to both the mother and the foetus, as infected erythrocytes sequester to the maternal side of the syncytiotrophoblast that lines the placenta. Despite the tremendous efforts in the field, the adhesive tropism of infected erythrocytes that leads to placental sequestration remains unsolved. In this thesis, I determined that measurements are not possible without the full length protein and interactions between the receptor and its erythrocyte-expressed ligand are not specific enough to distinguish from negative control experiments.

Another form of cell adhesion investigated in this thesis is the formation of so-called rosettes, that form when an infected erythrocyte binds to non-infected erythrocytes. Rosette formation is considered either an indication of severe malaria or a symptom of progressed infection and is believed to propagate the severity of infection by obstructing smaller vasculature and normal blood flow. in this thesis, I developed a platform to study the position of rosettes within a channel in flow, in order to determine their margination tendance. In those experiments, I verified that regardless of haematocrit value and size of rosette, rosettes remain in flow and do not marginate towards the walls of the flow chamber.

Zusammenfassung

Plasmodium falciparum infizierte Erythrozyten sind in der Lage, durch Adhäsine, die auf ihrer Membran exprimiert werden, an eine Vielzahl von extrazellulären Rezeptoren zu binden. Die molekularen Wechselwirkungen, die an der Parasitenbindung an diese Rezeptoren beteiligt sind, sind nur teilweise verstanden, obwohl das Phänomen selbst bekannt ist und als früher Indikator für die Diagnose einer schweren Malaria und das Fortschreiten der Infektion verwendet wird.

Die Bindung an die Mikrovaskulatur von Blutgefäßen oder die intervillösen Räume der Plazenta sichert das Überleben des Parasiten, da er die Filtrierung durch die Milz in den späteren Stadien der Reifung vermeidet. In dieser Arbeit wird die Bedeutung des bloßen Flusses und der Zellmorphologie in der Bindungsdynamik von parasitierten Erythrozyten weiter hervorgehoben. Während statische Adhäsionsassays ähnliche Mengen an Zellen zeigen würden, die in verschiedenen Reifungsstadien anhaften, ändert sich dieses Bild drastisch, wenn sie im Fluss beobachtet werden. Parasiten im Trophozoitenstadium scheinen weniger häufig, aber effizienter an das simulierte Endothelium zu binden. Im letzten Reifungsstadium verändern Parasiten im Schizontenstadium die Zellmorphologie in einem solchen Ausmaß, dass eine Adhäsion wahrscheinlicher ist, jedoch mit weniger Kontaktfläche und Dichte der beteiligten Rezeptoren. Veränderungen in der Membranmorphologie zwischen AA- und AS-Erythrozyten unterstreichen auch die Bedeutung der Rezeptorpräsentation und -zugänglichkeit für die Beeinflussung der Bindungseffizienz.

Die Auswirkungen einer P. falciparum-Infektion während der Primigravida sind sowohl für die Mutter als auch für den Fötus bedrohlich, da infizierte Erythrozyten auf der mütterlichen Seite des Syncytiotrophoblasten, der die Plazenta auskleidet, sequestrieren. Trotz der enormen Anstrengungen auf diesem Gebiet bleibt der adhäsive Tropismus infizierter Erythrozyten, der zur Plazenta-Sequestrierung führt, ungelöst. In dieser Dissertation stellte ich fest, dass Messungen ohne das Volllängenprotein nicht möglich sind und die Wechselwirkungen zwischen dem Rezeptor und seinem Erythrozyten-exprimierten Liganden nicht spezifisch genug sind, um von Negativkontrollexperimenten zu unterscheiden.

Eine weitere in dieser Arbeit untersuchte Form der Zelladhäsion ist die Bildung sogenannter Rosetten, die entstehen, wenn ein infizierter Erythrozyten an nicht infizierte Erythrozyten bindet. Die Rosettenbildung wird entweder als Hinweis auf schwere Malaria oder als Symptom einer fortschreitenden Infektion angesehen und es wird angenommen, dass sie die Schwere der Infektion durch Behinderung kleinerer Gefäße und des normalen Blutflusses fortpflanzt. In dieser Arbeit habe ich eine Plattform entwickelt, um die Position von Rosetten innerhalb eines Strömungskanals zu untersuchen, um ihre Randneigung zu bestimmen. In diesen Experimenten habe ich verifiziert, dass die Rosetten ungeachtet des Hämatokritwerts und der Größe der Rosette im Fluss bleiben und nicht zu den Wänden der Flusskammer hin angrenzen.

1. Introduction

1.1 Malaria as a disease

The unicellular parasite that causes the disease known as malaria belongs to the genus *Plasmodium*, with its most common deadly variant being *Plasmodium falciparum* [1, 2]. Five other known variants that can infect humans are *P. vivax, P. ovale curtisi, P. ovale wallikeri, P. malariae* and *P. knowlesi* [2]. Through the adaptation of improved prevention measures such as insecticide-soaked bed nets and seasonal chemoprevention, reported numbers of infection and deaths linked to malaria have decreased over the last few years [1]. Malaria infection can manifest in an uncomplicated manner causing non-specific symptoms such as fever, diarrhoea, headaches and chills. If untreated, the disease can progress to more severe symptoms, ultimately resulting in death. Severe malaria can manifest as cerebral malaria, severe anaemia, metabolic acidosis and respiratory distress caused by the infection [1, 3]. Other severe malaria symptoms include abnormal bleeding, acute kidney failure, hyperlactatemia, impaired consciousness and hypoglycaemia [3, 4]. Selection and timing of treatment [5] as well as the level of immunity (acquired or innate) [4, 6] are crucial factors that determine the outcome of the disease.

Africa remains the continent affected the most by the disease and makes up 82% of all reported cases. Moreover, 95% of reported deaths due to malarial infection are reported in Africa [1, 7]. Despite the steady decline reported over the past 20 years, the number of malaria deaths has increased in 2020 [1], from 560000 to 630000 deaths (12% increase), in part due to the disruption of services caused by the global COVID-19 pandemic. In high transmission areas [7], the risk of severe malaria is mostly concentrated to children under 5 years old, with a more increased risk of death in children under 3 years. Other groups that are most at risk during a malaria infection are pregnant women and non-immune travellers. In low transmission areas [7], such as Central and South America and Asia, infection occurs to all age groups and is more unstable [6].

Despite continuous efforts, malaria still poses a major threat to global health. Besides socio-economic factors, other major obstacles in reduction of morbidity and mortality caused by malaria are the emerging resistance to antimalarial drugs, resistance of the mosquito vector to insecticides, as well as the difficulty of vaccine development that elicits a long-lasting, protective immune response to infection.

1.2 Biology of *P. falciparum*

The life cycle of *P. falciparum* is complex and entails both asexual replication within a human host and sexual replication within mosquito vectors (Figure 1.1). The parasite is transmitted to the human host through a female *Anopheles* mosquito. During blood feeding, the motile form of the parasite, termed sporozoites, is inoculated into the host skin [8, 9]. These crescent-shaped parasites, move rapidly through the connective tissue and into the blood capillaries and are then passively carried towards the liver [9]. A successful hepatocyte invasion is followed by the formation of a parasitophorous vacuole around the sporozoite and the asexual replication of the parasite into infective daughter cells, termed merozoites [10]. After the liver development stage, which takes approximately 10 days, merozoites are released into the blood stream [11] and invade erythrocytes, which function as hosts during the intraerythrocytic replication cycle of the parasite (Figure 1.1).

Merozoites are exposed to the host immune system prior to invasion. Therefore invasion of erythrocytes only takes up to maximum 2 min and initializes the 48 h replication cycle within the host cell. The three major stages that the parasite develops into, are in a subsequent manner: ring stage (up to 16 h post invasion ;hpi), trophozoite (20-36 hpi), and lastly schizont (40-48 hpi). During the schizont stage, the nucleus divides asynchronously forming merozoites and eventually the infected erythrocyte ruptures. Merozoites are ejected and able to disperse in less than a second after rupture and infect nearby erythrocytes, initializing a new cycle of replication. Clinical manifestations of the disease are present during the intra-erythrocytic stage of infection, with synchronous erythrocyte rupture and merozoite release linked to periodic fever in patients.

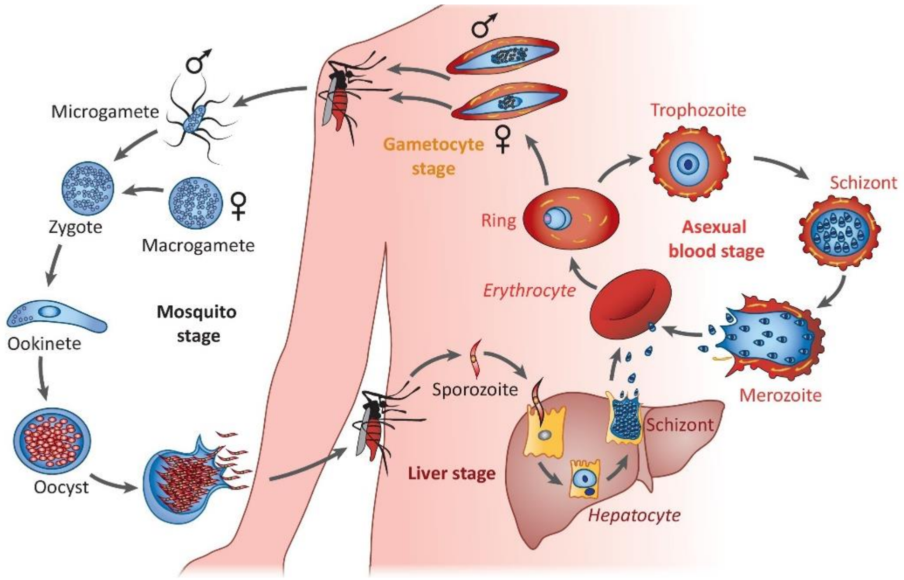

Figure 1.1: *Plasmodium falciparum* replication cycle in human and mosquito host. The mosquito takes up gametocytes during a blood meal and these sexually replicate to produce sporozoites. These are then transferred during a blood meal to the human host and first infect the liver. Maturation in the liver stages produces merozoites that release in the blood stream and infect erythrocytes. The parasite replicates asexually in the blood stages maturing from ring to trophozoite to schizont stage and rupturing producing merozoites that reinvade erythrocytes in the human blood stream. Blood stage parasites can also develop into gametocytes that are then again taken up by the mosquito closing the cycle. Image adapted from [12].

A small fraction (less than 10%) of intraerythrocytic parasites develop into gametocytes, a sexual form of the parasite that commits to sexual development within vectors. Gametocytes mature within erythrocytes and circulate in the vasculature until taken up by a female Anopheles mosquito, during a blood meal. Female gametocytes, termed macrogametes, are fertilized by microgametes, a term describing male gametocytes, and form a zygote. Through sexual replication, an ookinete forms and migrates through the mosquito midgut endothelium to develop into an oocyst on the outside of the mosquito gut. Within the oocyst, thousands of sporozoites form through asexual replication and after approximately 17 days are released and move with the haemolymph to the salivary glands. This concludes the cycle within the vector and motile sporozoites are once more transmitted to a human host through a blood meal [13], and perpetuate the parasite´s replication and prevalence.

1.3 Cytoadherence and antigenic variation

1.3.1 Endothelial cell adhesion

In order to evade the human host immune system and avoid splenic clearance the parasitized erythrocyte is able to adhere to the endothelial cell wall of blood vessels (Figure 1.2). This sequestration is also a prominent pathological feature in severe malaria cases, as late-stage parasites adhere and sequester in capillaries and post-capillary venules of organs such as the brain, heart, eyes, liver, kidneys and placenta of infected individuals.

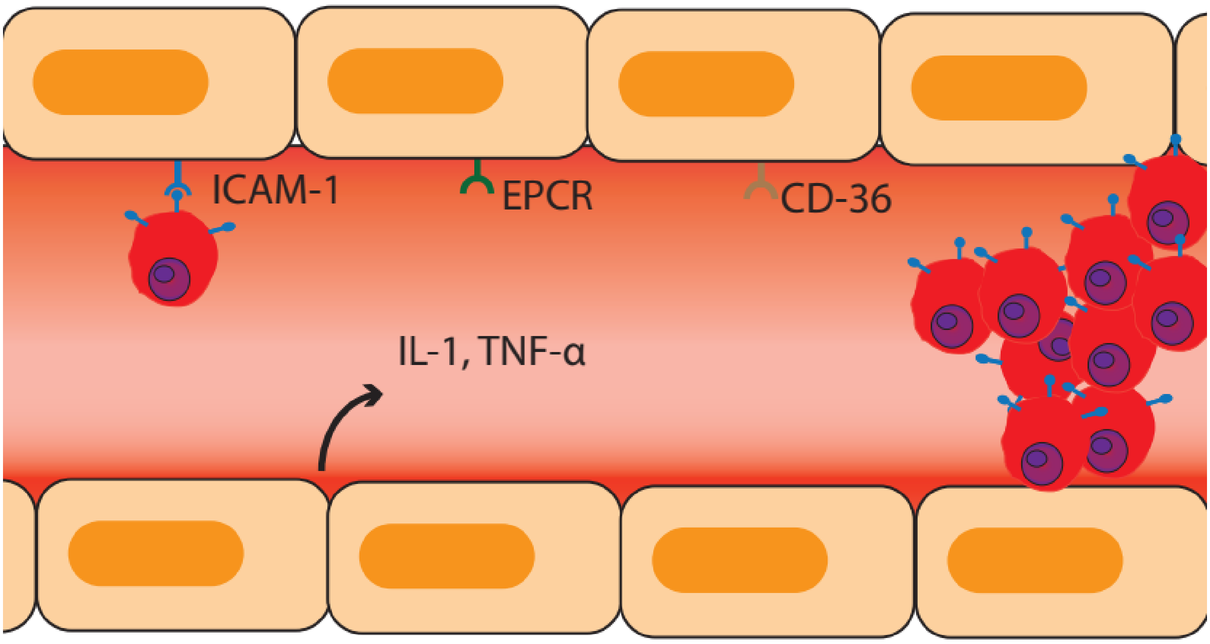

Figure 1.2: Sequestration and vascular occlusion by *Pf*-infected erythrocytes. Adherence to ICAM-1, EPCR and CD-36 receptors leads to sequestration of RBCs infected with mature stage (trophozoite and schizont stage) parasites onto the endothelium. This can cause secretion of pro-inflammatory factors such as IL-1 and TNF-α or cause a vascular occlusion.

This phenomenon not only contributes to the survival of the parasite, but it can also lead to a multitude of pathogenic consequences. Sequestered cells can obstruct normal blood perfusion, which in turn leads to ischemia, acidosis and organ damage [2]. Oxygen delivery is also further compromised by increasing numbers of parasites in the blood. Increasing numbers of sequestered infected erythrocytes also leads to lactic acidosis, due to the increased anaerobic glucose metabolism during cytoadherence and a resulting decrease in blood flow perfusion into the tissues [14, 15]. Some researchers have also reported the apoptosis of endothelial cells following interaction with infected erythrocytes *in vitro*, as well as a drop in nitric oxide levels, an important signalling molecule for proper endothelial cell function [15-18].

Activation of endothelial cells is often included as a symptom of severe malaria, as parasite sequestration upregulates vascular endothelial cell receptors, in turn potentiating parasite survival as well as vascular obstruction [19, 20]. Increased binding to the ICAM-1 receptor on the surface of endothelial cells is associated with increased secretion of the nuclear factor kappa beta (NF-κβ) as well as the tissue factor (TF) [21]. Rapid translocation of this factor upon cytoadhesion of *P. falciparum (Pf)* infected erythrocytes induces the transcription of genes encoding cytokine, chemokines and cell adhesion molecules. In the case of cerebral malaria, loss of tight junctional proteins such as vinculin, in areas where infected erythrocytes adhered, was shown [19, 22, 23]. The blood brain barrier also seems to weaken and allows an easier passage once it has come in contact with parasitized erythrocytes [24, 25]. Another factor that seems to be upregulated during cytoadhesion onto endothelial cells in the brain of hosts, is the tumour necrosis factor alpha (TNFα) [26, 27]. While excretion of the factor seems to be normal response of the host during infection, fatal cases displayed a tenfold increase in its production. These effects are devastating in the case of placental malaria leading to premature delivery, low birth weight and increased mortality of the new-born as well as anaemia for the mother [28].

The molecular interactions involved in parasite binding to the microvasculature are only partly understood, although the trait itself is well-known and used as an early indicator of severe malaria diagnosis and progress of infection [14]. This discrepancy is mainly due to the complexity of the *Pf* erythrocyte membrane protein 1 (PfEMP1) family that mediates most of endothelial cell binding processes, and which is encoded by the *var* genes. Each parasite genotype codes for a total of 60 *var* genes per haploid genome and parasites are able to switch between *var* genes in order to modify antigenic and binding properties of the infected erythrocyte [29, 30]. These pressures have resulted in a diversification of PfEMP1 adhesion domains during the process of antigenic variation, and are responsible for the persistent nature of the disease [31, 32]. All *var* genes consist of a 5´- upstream promoter sequence (Ups), a first exon, an intron and a second exon. The first exon is highly variable, as it encodes the extracellular portion of the protein as well as the trans membrane domain [33]. The second exon on the other hand is highly conserved and encodes the cytoplasmic tail of the PfEMP1 protein [33, 34]. *Var* genes have been split into three major groups (A, B and C) based on the conserved upstream sequence (Ups) regions. Group A genes are transcribed towards the telomere in the opposite direction as UpsB *var* genes. UpsC *var* genes are located in the centre of chromosomes in tandem arrays with other UpsB or UpsC *var* genes, while UpsB genes are either subtelomeric or chromosome central [30, 35, 36]. Each *var* gene also harbours an intrinsic promoter driving transcription of an antisense long non-coding RNA with a yet unknown function, which seems to be simultaneously upregulated at 8-18 hpi if the corresponding *var* gene is expressed [37]. The overall conservation of *var* gene organisation might reflect recombinational constrains based on host selection pressures [30].

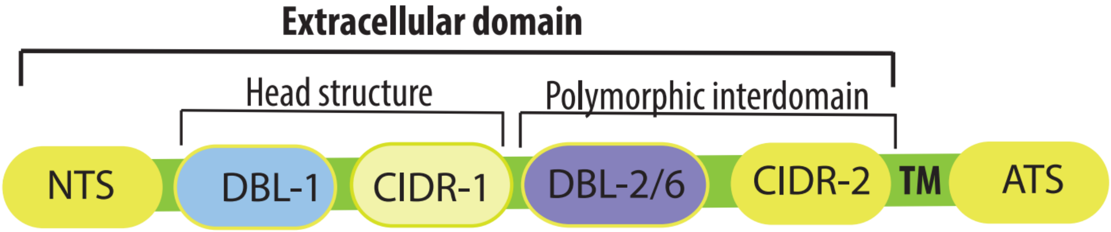

Figure 1.3: Typical PfEMP1 block structure. The extracellular domain of this proteins consists of an N-terminal sequence (NTS), followed by Duffy-binding like domain 1 (DBL-1), Cysteine-rich interdomain region 1 followed by DBL2 through 6 and CIDR-2. The transmembrane domain (TM) is then followed by intracellular domain termed acidic terminal segment (ATS). Adapted from [38]

All PfEMP1 proteins share some conserved structural features, such as the N-terminal segment (NTS), Duffy Biding like domains (DBL), cysteine-rich interdomain regions, a trans membrane domain (TM), a constant2 (C2) domain and an intra-cellular acidic terminal segment (ATS) (Figure 1.3) [39-42]. The size of PfEMP1 molecules is as diverse as their binding properties ranging from 200-350 kDa [31]. While the extracellular domain is highly variable [43], the TM and ATS domains are conserved across the variants. The TM domain anchors the molecules to the cell membrane while the ATS anchors them to the cytoskeleton of the host erythrocyte.

Six major classes of DBL domains have been proposed based on amino acid similarity (DBL α, β, γ, δ, ζ and ε). These are further characterized by definition of 10 semi-conserved homology blocks (HB a-j) [44-46] and by definition of three structural subdomains [47]. There are three proposed classes for CIDR (α, β and γ), based on homology [48]. These domains are continuously exposed to selective pressure by the host immune system, and due to the vast recombination possibilities of these building blocks, parasites are able to evade the immune system and maintain long-term infections even in non-naïve individuals [31, 49]. It has been proposed that once the immune system of a host can identify all PfEMP1 molecules expressed by the infecting strain, the infection can be overcome. Most PfEMP1 proteins have a semi-conserved structure of their protein head consisting of NTS-DBL$_{\alpha}$-CIDR1 [42]. However, most PfEMP1 proteins have less than 50% overall amino acid identity overlap, even coming from the same architectural type. The same parasite variant can express different PfEMP1 molecules in different hosts highlighting the regulation of expression by the host and the environment of the parasite.

1.3.2 VAR2CSA and placental malaria

A PfEMP1 protein that is unique both in its target, expression and structure is VAR2CSA. This protein is known to bind to placental tissue [32], by binding to chondroitin sulfate A (CSA) expressed in the intervillous spaces of the placenta (Figure 1.4) [50-52]. VAR2CSA is unusually conserved and structurally and functionally different from other PfEMP1 variants [51, 53, 54], and therefore primarily women during their first pregnancy are more susceptible to placental malaria and immunity is acquired over multiple pregnancies [51].

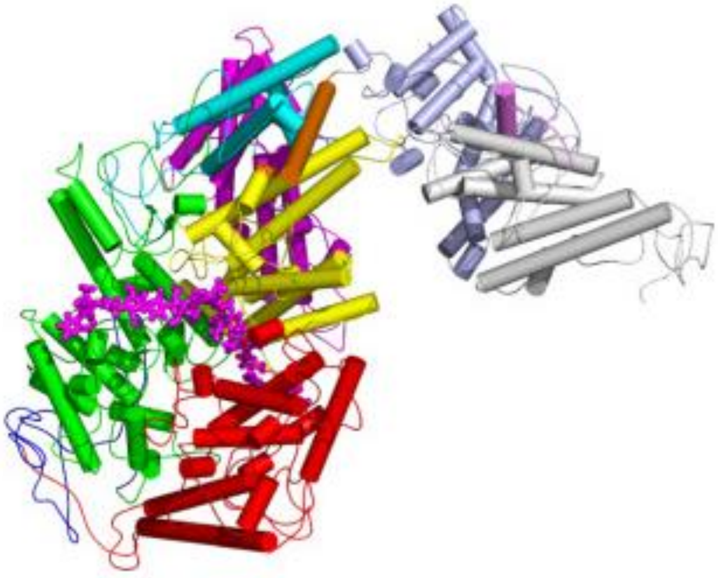

Figure 1.4: VAR2CSA structure with bound chondroitin sulfase A (CSA). Structure as depicted in Wang *et al*. 2021 [55] (RCSB PDB code: 7B52).

The effects of a *P. falciparum* infection during primigravida are threatening to both the mother and the foetus, as infected erythrocytes sequester to the maternal side of the syncytiotrophoblast that lines the placenta [51]. Despite the tremendous efforts in the field, the adhesive tropism of infected erythrocytes that leads to placental sequestration remains unsolved.

The *var* gene encoding this protein is located on the right telomere of chromosome 5 [42]. VAR2CSA is a 318-478 kDa large protein [56, 57] with six DBL domains, a CIDR region between DBL2 and DBL3 and a variable number of interdomains [58]. More specifically, recent studies showed that the ectodomain structure includes a stable core (NTS-DBL1X-Idi-DBL2X-ID2-DBL3X-DBL4e-ID3) flanked by a flexible arm (DBL5e-DBL6e) [55, 59]. Individual domains can also bind to various negatively charged proteoglycans, other than CSA. Researchers have analysed the domains of this protein in order to identify a smaller region that can be targeted for vaccine development, to protect pregnant women from pregnancy associated malaria (PAM) [56, 58, 60]. A study in 2012 identified interdomain1-DBL2x as the minimal binding region having a molecular mass of only 62 kDa [60]. However, the structure solved by Cryo-EM in 2021 has revealed more about the molecular binding of CSA. This highlighted the unusual structure and charge of DBL2 domain. ID1 and ID2 regions are important for forming a slope through the protein core structure and the lysine-rich region of DBL2 *N*-terminus loop provides an ideal interaction point for proteoglycans [55, 59]. A second binding site forms a funnel created by DBL1-4 and ID1-3, to interact with the CSA molecule and show high affinity to it [59].

1.3.3 Rosetting

An additional major form of cytoadhesion of *Pf* infected erythrocytes is the formation of so-called rosettes (Figure 1.5)[61-63]. The rosetting phenotype has been reported for all variants known to infect humans, with schizont stage parasites forming larger rosettes compared to trophozoite stage *Plasmodium* parasites [64, 65]. While the literature is not too specific about the constitution of a rosette, most sources agree that when at least one infected erythrocyte binds two or more uninfected erythrocytes and forms a “cluster”, it constitutes a rosette. It is possible for more than one infected erythrocyte to bind, forming a larger rosette with several uninfected erythrocytes adherent. Causality is also unclear yet, however rosette formation is considered either an indication of severe malaria or a symptom of progressed infection. Rosetting is believed to propagate the severity of infection by obstructing smaller vasculature and normal blood flow [66].

Infected erythrocyte adhesins bind to complement receptor 1 (CR1) which is expressed on the surface of uninfected erythrocytes [61, 67]. Furthermore, it has been proposed that a common African polymorphism of CR1 reduces rosetting and could therefore protect against severe malaria to an extent. Several parasite ligands have been linked to rosetting with the most prominent protein family being PfEMP1 adhesins. However, there is some evidence that another adhesin family present on infected erythrocytes, the STEVOR family and RIFIN family of variant proteins, could also play a part in rosette formation [68-70]. While *var* genes are unique to *P. falciparum*, genes similar to *stevor* and *rif* are found in other malaria parasite species [71-73].

Figure 1.5: Red blood cell aggregate known as rosette. Red coloured cells are uninfected erythrocytes and blue coloured cells are Plasmodium falciparum infected erythrocytes. Figure adapted from Dasanna *et al* (in preparation).

RIFINs are polypeptides encoded by 150 *rif* genes, comprising the largest family of antigenically variable molecules in *P. falciparum* [74-76]. RIFINs are low-molecular weight proteins, with a yet unclear function. Only subtype A of the RIFIN proteins are expressed on the surface of parasitized erythrocytes [76, 77] and those possess an insertion of 25 amino acids at the *N*-terminus, that B subtype RIFINs lack [69]. A-RIFINs are able to bind A-group erythrocytes and form rosettes, while O-group erythrocyte rosetting is primarily mediated by PfEMP1-adhesins [69].

STEVOR proteins are encoded in *stevor* genes, subtelomeric open reading frame genes belonging to a large multigene family. Intensive research on their function has shown that these proteins are expressed in multiple parasite stages including gametocytes, sporozoites, merozoites and cell surface of intraerythrocytic stage parasites [78-81]. It has been hypothesized that due to their expression at the merozoite stage and because anti-STEVOR antibodies inhibit merozoite invasion *in vitro*, STEVOR proteins may modify erythrocyte cell structure to facilitate invasion [68, 82]. STEVOR expressing parasites can also form rosettes in the absence of PfEMP1 adhesins and bind to a protein on the surface of uninfected erythrocytes similar to Glycophorin A or C [68].

1.4 Knobs and KARPH

PfEMP1 molecules are presented on the surface of an infected erythrocyte on nanoscale membrane protrusions termed knobs. Knobs appear prominently from early trophozoite stage onwards and are electron dense, i.e. visible in electron microscopy (EM) [83, 84]. The diameter of a knob is between 50 and 120 nm, while its height varies from 2 to 20 nm and anchor PfEMP1 molecules to the cytoskeleton, while providing an ideal presentation scaffold [83-86]. Sanchez *et al* showed in a study in 2019 that each knob of parasitized erythrocyte (FCR3 strain) expresses 3.3 ± 1.7 VAR2CSA-PfEMP1 molecules [87].

KAHRP is a 59-72 kDa large protein, that is localized with PfEMP1 to the intraerythrocytic side of the membrane. It is predicted to be highly disordered and contains a PEXEL motif that mediates export, an *N*-terminal signal sequence, a histidine-rich region and two variable tandem repeat regions [86, 88-90]. KAHRP was found to interact with and be in close proximity to ankyrin, a key element of the erythrocyte cytoskeleton as well as spectrin [90-92]. Other proteins that are found in the intraerythrocytic part of knobs are *Plasmodium* helical interspersed sub-telomeric (PHIST) protein and PfEMP3, while mature parasite-infected erythrocyte surface antigen (MESA) is found along with PfEMP1 on the outer membrane of infected erythrocytes [89, 93].

It is well established that PfEMP1 molecules are trafficked to knobs via Maurer´s clefts with the help of PfEMP3 [94] and a putative loading complex that includes the protein GEXP07 [95] and PTP7 [96]. Other proteins that assist in the assembly of knobs and transport through the clefts is the family of HSP40 and HSP70 [97]. Disruption or deletion of genes required to transport PfEMP1 molecules causes dramatic reductions in cytoadherence and is linked to loss of virulence for the parasites [97].

1.5 Molecular mechanisms of cytoadherence to host receptors

In order to adhere to the endothelium and successfully evade splenic clearance, the parasite has to express adhesins that interact with receptors of microvascular endothelial cells and uninfected erythrocytes. The parasite is able to express a single PfEMP1 variant that adheres to a target receptor and its adhesion affinity is determining the rheology of parasitized erythrocytes as well as the virulence of the disease.

1.5.1 ICAM-1

Intercellular adhesion molecule -1 (ICAM-1) is a 90-115 kDa transmembrane human protein (Figure 1.6). It expresses five immunoglobulin-like domains and is usually found in a dimer, expressed constitutively on the surface of a wide range of cell types including endothelial cells [98, 99]. Leucocytes interact with ICAM-1 via integrin receptors such as LFA-1 and Mac-1 and this interaction is critical for a cascade pro-inflammatory response. Expression of ICAM-1 is upregulated during inflammation in response to cytokines, such as TNF-α and IL1β [98].

Pathogenesis of cerebral malaria has been linked to sequestration of infected erythrocytes binding to ICAM-1 [98, 100]. This sequestration has been shown to activate endothelial cells *in vivo* [101] and *in vitro* [102, 103], and monocytes were often co-localized with parasites at the sites of microhaemorrhages [104]. Due to the variability of PfEMP1 expression profile, it has been very difficult to link specific variants to ICAM-1 adhesion and pathogenicity making vaccine development against these variants solely based on their target adhesin extremely troublesome. To that end, several attempts to correlate a specific expression motif of PfEMP1 adhesins with function and disease outcome, most notably by developing a system of categorization based on the upstream var gene sequence[39]. PfEMP1 variants are grouped based on their semiconserved promoter sequence, chromosomal location, and amino acid sequence are grouped into A, B and C families of variants [39, 40]. Group A shows less variability and is an easier target for vaccine development and acquired immunity. PfEMP1 molecules belonging in group A and expressing a particular subtype of DBL and CIDR domains in short tandem combinations (DC cassettes) have been shown to primarily bind against ICAM-1 [105, 106]. Leucocyte receptors bind to the external side of the dimer, while PfEMP1 molecules bind to the inner pocket of ICAM-1 making it possible to bind at the same time [98, 99, 107].

Three of the abovementioned DC cassettes DC4 (group A), DC8 (group B/A) and DC13 (group A) were implicated in the pathogenesis of cerebral malaria and severe malaria [40, 108, 109]. More specifically, it has been shown that in the cases where variants of group A were expressed, patients suffered from more severe symptoms. Immunity against these DCs is often acquired in endemic regions [40].

The discovery of an area where a genetic polymorphism of the *N*-terminal Ig-like domain of ICAM-1, designated ICAM-1$^{\text{Kilifi}}$ raised considerable interest, due to a predisposition for cerebral malaria development for individuals presenting this mutation [110]. It is present in approximately 30 % of several African populations and at lower frequencies in other malaria endemic regions but not in Caucasian populations [98, 111-113]. In subsequent studies, it was determined that the mutation causes structural differences, with the ICAM-1$^{\text{Kilifi}}$ carriers showing a reduced binding efficiency of infected erythrocytes [20].

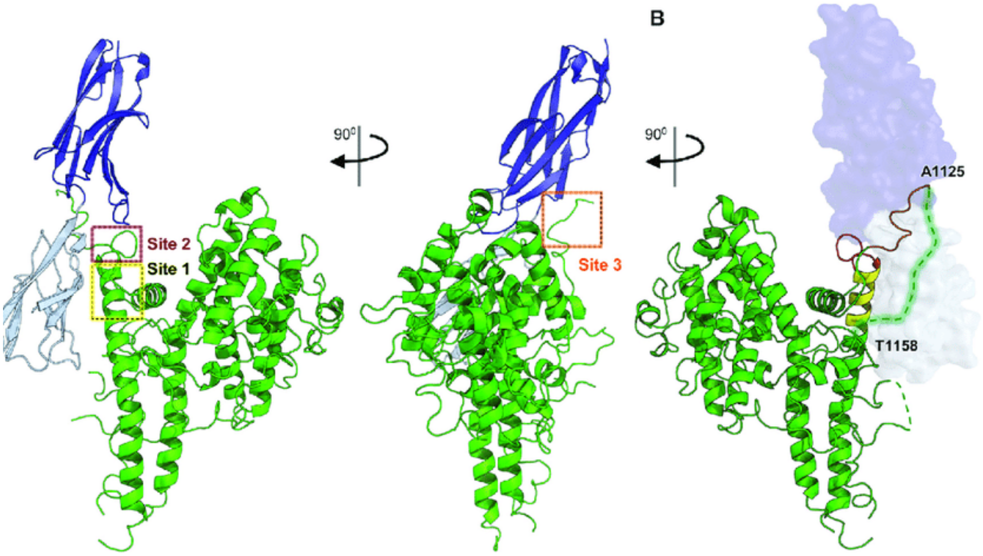

Figure 1.6: ICAM-1 structure and possible adhesion sites for PfEMP1 molecules. Helices are shown in green while beta sheets are shown in blue. Structure taken from Lennarzt *et al*. 2019 (RCSB PDB code: 6S8T and 6S8U). [114]

1.5.2 CD-36

A further commonly investigated glycoprotein receptor is CD-36, an 88 kDa large protein expressed on the surface of endothelial cells, monocytes and some melanoma cell lines [115]. The binding of CD-36 has been linked to group B and group C PfEMP1 expression [45, 115, 116]. These adhesins are linked to uncomplicated malaria and childhood infections [117]. Due to their larger diversity compared to group A variants, group C PfEMP1s are a less likely vaccine candidate.

1.5.3 EPCR

Another receptor that has been recently in the focus of research to determine its correlation with severity of infection is the endothelial protein C receptor (EPCR) [26, 118-120]. The group B/A PfEMP1 receptors bind to EPCR via CIDRα1 domains while group B and C PfEMP1 tend to bind to CD-36 and their expression is mutually exclusive [57, 121]. This specific subtype expresses a DC8 cassette and particularly a CIDRα1 domain expression at the N-terminal region is shown to interact with EPCR. The bound parasite blocks the binding of protein C to the receptor, resulting in anti-inflammatory response and barrier-disruptive events [122, 123]. As mentioned before, binding of DC8 cassette expressing parasites has been linked to severe malaria and therefore could constitute a vaccine development target.

1.5.4 Chondoritin sulphate A (CSA)

CSA is a glycosaminoglycan (GAG) composed of repeating dimeric units of *N*-acatyl-D-galactosamine (GalNAc) and glycoronic acid (GlcA). It is commonly expressed by syncitioblasts that extend to the intervillous spaces of the placenta.VAR2CSA is the PfEMP1 variant that is able to recognize and interact with CSA [52]. A CSA dimeric unit can be sulphated at the carbon 2 (C2) position of GlcA and/or the carbon 4 (C4) and carbon 6 (C6) position of GalNAc and studies performed to GAGs expressed on syncitioblasts displayed that there is presence of low sulphated C4-sulphated (4-8 %) CSA that is recognized by VAR2CSA.

1.5.5 Other receptors mediating cytoadhesion

Further endothelial cell receptors such as P-selectin, E-selectin, PCAM-1, CD9 and CD151 and thrombospondin (TSP) have also been studied for their roles in mediating cytoadhesion of infected erythrocytes, but have not resulted in a specific adhesion type or severity [124-127].

1.6 Mechanics and remodelling of infected red blood cells

Theoretical predictions as well as experimental observations have shown that the parasite alters the mechanical deformability of its host cell.

1.6.1 Erythrocyte shape

Erythrocytes are naturally able to change their shape in response to mechanical stress, in order to allow passage through the vascular system and intra-endothelial fenestrations in the spleen. Normally, erythrocytes are found in a unique, characteristic biconcave geometry [128-130]. The average cell size lies between 6-9 µm in diameter and 2-3 µm in thickness [131]. The observed deformability of red blood cells is attributed to the fluid nature of the plasma membrane, a high plasticity of the underlying cytoskeleton, the homogeneous cytoplasm consisting primarily of haemoglobin and a high surface area to volume ratio. Due to their biconcave shape, the mean volume of approximately 90 fl corresponds to 135 μm^2 surface area, which is significantly higher than the surface area of a sphere with the same volume (97 μm^2). The high (up to 95%) content of haemoglobin in mammalian erythrocytes results in a low viscosity of the cytoplasm, also contributing to a higher flexibility of the cell [132].

The dominant regulators of the ability of erythrocytes to deform are the membrane and cytoskeletal components. It is important that surface area and cell volume are maintained, even during passage through narrow micro-vessels to retain the cell´s natural form and connected functions [133, 134]. The erythrocyte membrane consists of a carbohydrate-rich glycocalyx on the outer layer and a 5 nm-thick phospholipid bilayer with equal weight of cholesterol, that is supported by a pseudohexagonal meshwork of primarily actin and spectrin [128, 129, 135]. Other important components of the erythrocyte cytoskeleton are protein 4.1R, ankyrin, tropomyocin, adducin and tropomyosin [129]. The cytoskeleton is the most essential structure that maintains the mechanical stability, durability and flexibility and prevents membrane rupture. The skeletal integrity is also crucial for fast recovery of the discoid shape after mechanical stress has been applied, with fast recovery times being an indication of proper cell function [136].

Genetic or acquired red blood cell disorders as well as malaria infection interfere with the structure of erythrocytes and impact its function. The effects of these disorders can be divided into two classes, the first being disorders due to a mutation of membrane or skeletal protein, as observed in hereditary elliptocytosis, ovalocytosis, spherocytosis, and hereditary pyropoikilocytosis [133, 137]. The second category observes altered function of erythrocytes due to secondary effects on the membrane components, mainly caused by mutations in the globin genes. Primary examples of this category are sickle cell disease, Hb SC or CC disease and thalassemia [133, 137, 138]. Clinical presentations of these diseases are most commonly haemolytic anaemia resulting in jaundice, fatigue, splenomegaly, gallstones and cholecystitis [137]. Another drastic effect of these diseases is the impairment in blood flow and tissue perfusion.

1.6.2 Balanced polymorphism for adult haemoglobin

Adult haemoglobin (HbAA) is a tetramer of two α- and two β-globin chains, attached to a heme group containing an Fe(II) ion that when bound to oxygen changes to Fe(III) and back when oxygen is released. Hemoglobinopathies caused by mutations in the globin gene are one of the most common monogenic disorders. Thalassemias is a class of hemoglobinopathies where synthesis of α- or β- structurally correct globin chains are produced in reduced amounts. Qualitative hemoglobinopathies is a second overall class of hereditary globin mutation where structurally abnormal variants of globin are produced.

Haemoglobin S (HbS) is a single amino acid polymorphism of the β-globin chain of Hb, where the glutamic acid in position 6 is substituted by valine. This substitution affects cell shape as well as its physiological properties and functions. Submotted to de-oxygenation HbS polymerizes and sticks to other HbS chains causing the shape of the erythrocyte to sickle [139]. This state is somewhat reversible upon oxygen binding, however a population of cells remains sickled irreversibly, causing vascular stasis and occlusion [140]. Even in the reversibly sickling cells, deformability is greatly reduced and viscosity is increased due to impaired ion transport, increased production of reactive oxygen species (ROS), and increased haemoglobin concentration [139, 141]. HbS de- and repolymerises upon oxygen release and binding respectively. These multiple cycles render the molecule unstable leading to changes inthe physiology of HbS-carrying erythrocytes [142].

In haemoglobin C (HbC), glutamic acid in position 6 is substituted by a lysine. This results in less severe clinical complications and erythrocyte phenotype, such as reduced cell deformability and dehydration. HbC occurrence is primarily restricted to West Africa [143]. Haemoglobin E (HbE) is the result of a single point mutation of glutamic acid in position 26 to lysine and can be mainly found in Southeast Asia [144]. Structural hemoglobinopathies prevail in malaria endemic regions, despite the drawbacks that HbS, HbE and HbC cause the carrier, thanks to the protection that they confer against malaria and anaemia [144-146]. This trade-off between heterozygous advantage and homozygous fitness cost was termed balanced polymorphism. HbAS allele confers up to 60% protection against clinical malaria and up to 90% protection from severe symptoms and death [138, 147].

1.6.3 Infection and cell morphology

During an infection with *P. falciparum*, parasitized erythrocytes become increasingly spherical, as the parasite modulates the cytoskeleton and membrane to accommodate its growth [130, 148]. Osmotic pressure increases due to induction of new permeation pathways (NPPs) in the membrane and subsequent increase in solute traffic of nutrients, waste products, and cations by the parasite [149-151]. However, Waldecker *et al.* (2017) showed that critical haemolytic volume is only reached at the end of the 48h cycle of parasite maturation and that rupture is prevented by the increased trafficking of Hb and release of its degradation products into the extracellular environment [150]. Furthermore, parasitized erythrocytes become more rigid and less deformable with increasing sphericity [148, 152-155] partly due to the presence of the parasite, which can be seen as a solid mass within the cell that impacts volume and viscosity [156]. Rigidity of parasitized erythrocyte membrane might also be amplified by oxidative damage as well as the presence of knobs [90, 157]. Knobby parasite lines showed increased rigidity compared to knobless lines and insertion of proteins in the erythrocyte membrane such as KAHRP, PfEMP3 and PfEMP1 is changing the properties of the membrane itself. One should also take into account the introduction of more anchoring points between the cytoskeleton and knobs that also affects its plasticity [157, 158]. Knob-density vertical coupling increase the structural strength of the spectrin cytoskeleton while knob-free regions show elevated shear strain [157].

The exact mechanism of protection by haemoglobin mutants is not clear yet. Parasite growth rates in HbAS and HbAC heterozygotes were comparable in field studies, however there were significant differences in clinical complications and severity[146, 159-161]. Infected haemoglobinopathic erythrocytes displayed aberrant development of the parasite, knob distribution and size as well as PfEMP1 presentation [87, 150, 162-165]. Lansche *et al.* (2017) demonstrated *in vitro* that there are significant differences in dynamic cytoadhesion between parasitized HbAS and HbAA [102]. Rosetting frequency also seems to be reduced or not-present in heterozygous carriers [66, 166, 167].

Differences in presentation of knobs, amount of PfEMP1 molecules present and shape of *Pf* -infected parasite could be the driving factor for protection of heterozygotes [87, 102, 155, 168, 169]. Reduced cytoadhesion might result in a higher splenic clearance rate and contribute to less severe manifestation of malaria infection [170].

1.7 Interaction with host cells and dynamic adhesion

For leucocytes and single infected erythrocytes, margination is the key step for cytoadhesion. However, larger aggregates of cells such as rosettes or clusters with platelets seems to disrupt flow only in post-capillary venules and micro vessels where they are able to obstruct flow.

1.7.1 Leucocyte adhesion dynamics in flow

Leucocytes usually flow passively in the circulatory system and only adhere to the endothelium after activation through an inflammatory stimulus [171]. These chemokines trigger the expression of glycoprotein ligands on the tips of microvilli membrane protrusions. These bind to sulphated sugars and activate P- and E- selectin expression, which in turn activate leucocyte surface expression of ligands such as P-selectin ligand -1 (PSGL-1) [172]. Weak bonds form and the leucocyte rolls getting into contact with inflammatory signals such as IL-8 [173] . This triggers expression of integrins that bind firmly to ICAM-1 and the activated leukocyte finally tethers onto the endothelium. Once firmly attached, leucocytes can slowly extravasate onto the site of inflammation, either through the paracellular or transcellular route [174].

Adhesion dynamics can be classified in rolling adhesion, firm adhesion and transient adhesion [175, 176]. These are directly influenced by molecular association and dissociation rates between ligands and the strength of the bonds that form in these processes. During transient and rolling adhesion, the cell constantly forms new bonds at the front end while breaking existing bonds at the back end in order to maintain velocity. Firm adhesion is achieved when the bonds formed are strong and do not break, keeping the cell at almost zero velocity.

To further investigate these interactions between adhesion receptors and ligands that facilitate rolling adhesion, Li et al developed a platform using dark-field imaging and particle tracking [177]. However, due to the flexible nature of microvilli, analysis of such a complex movement is rather difficult to track and analyse [174]. It has also been demonstrated that the bonds formed between a rolling leucocyte and endothelial receptors displays sheer enhanced tethering [172, 178].

1.7.2 Infected erythrocytes in flow

While uninfected erythrocytes remain in flow and only marginate or aggregate in pathological conditions, *Pf*-infected erythrocytes marginate and are able to cytoadhere as covered in Section 1.3 Cytoadherence and antigenic variation. The dynamic states of these adhesion processes have been the focus of recent studies, displaying complex phenotypes of tumbling, rolling and firm adhesion. Interestingly, there are several similarities between the dynamic adhesion processes of leukocytes and Pf infected erythrocytes. Both are governed by the bond formation and the strength of ligands expressed on elevated platforms present on the cell surface. Another similarity between the two cell types is that they employ tension-enhanced adhesion systems in order to marginate to the blood vessel walls under sheer stress.

It has been suggested that adhesion against specific endothelial cell receptors (covered in section 1.3.1), facilitates different cytoadhesive phenotypes. VAR2CSA and CSA adhesion has been shown to be firm, with binding strength decreasing upon increased tensile stress However, under physiological venular pressures, these bonds provide stationary adherence and result in parasite accumulation when shear stress due to flow is low [179, 180]. Contradicting results report CD-36 or ICAM-1 binding to its respective PfEMP1 can facilitate either firm or rolling adhesion of the parasitized erythrocyte, arguably influenced primarily by shear force during flow [102, 180-183].

1.7.3 Correlation between haemoglobinopathies and cytoadhesion in flow

Knob formation, cell shape and flexibility as well as the binding affinity and strength are all important parameters that influence the phenotype of dynamic adhesion onto the endothelium [184, 185]. Therefore, it is not surprising that cytoadhesion of sickle cells and the effects of this mutation on parasite fitness during dynamic binding have been of great interest to experts [45, 102, 150, 168, 186]. Though it is well established that cytoadhesion of sickle cells is reduced compared to the HbAA phenotype, it is still disputed whether this is the primary benefit the disease offers. Arguably due to decreased cytoadherence, phagocytosis, and splenic clearance of infected erythrocytes are increased leading to a reduction in parasite load and eventually thus avoiding severe disease presentation. 1.8 Aims

This thesis is challenging three major questions regarding cytoadhesion of *Plasmodium falciparum* infected erythrocytes.

Aim 1: In order to study adhesion patterns of mature stage parasites in HbAA and HbAS infected erythrocytes with the endothelium during dynamic adhesion, a platform had to be developed, adapted or optimized. Standardizing this platform for different stages will enable evaluation of the effect of parasite maturation and cell morphology on cell adhesion to endothelial receptor ICAM-1.

Aim 2: The second target of this thesis was to determine the dynamics of a single-molecule interaction between a fragment of PfEMP1 receptor, VAR2CSA and its ligand (CSA) in force spectroscopy measurements. Using atomic force microscopy (AFM) to determine adhesion strength and performing measurements for different retraction speeds, will provide information regarding the influence of flow on the longevity and strength of interaction.

Aim 3: It is not yet known what triggers the rosetting phenotype during a *Plasmodium falciparum* infection. Since a rosette cluster has a larger gravitational pull than a single infected erythrocyte, it could be plausible to assume that rosettes form in order to marginate the parasitized erythrocytes to the blood vessel wall. For this last project, my goal was to develop a platform to investigate the effect of flow and different haematocrit values on rosette margination and relative position within the blood vessel.

2. Materials and Methods

2.1 Materials

2.1.1 Equipment

Equipment	Model	Manufacturer
Analytical balance	ABT 120-5DM	Kern&sohn, Ballingen, Germany
Atomic force microscope	NanoWizard3	JPK instruments, Berlin, Germany
Autoclave	ABT 120-5DM	Kern&sohn, Ballingen, Germany
Balance		Sartorius GmbH
Centrifuge	Biofuge fresco	ThermoFischer Scientific, Dreieich, Germany
	Biofuge pico	ThermoFischer Scientific, Dreieich, Germany
	Megafuge 1.0 R	Heraeus, Hanau, Germany
	Megafuge 2.0 R	Heraeus, Hanau, Germany
Confocal microscope	LSM510	Zeiss, Jena, Germany
Electrophoresis power	Power Pac 300	Bio-Rad, München, Germany
Supply	Power Pac 200	Bio-Rad, München, Germany
Flow cytometer	FACSCalibur	Becton and Dickinson, Heidelberg, Germany
Syringe pump		
Freezer -20°C	LGex 3410 MediLine	Liebherr, Biberach, Germany
Freezer -80°C	HERAfreeze	ThermoFischer Scientific, Dreieich, Germany
Fridge	LKexv 3910 MediLine	Liebherr, Biberach, Germany
Heating block	NeoBlock Mono I	NeoLab, Heidelberg, Germany
High precision pump	AL-4000	World precision instruments, Florida, USA
Ice machine		Ziegra, Isernhagen, Germany
Incubator	Heraeus cytoperm2	ThermoFischer Scientific, Dreieich, Germany
	HeraCell	ThermoFischer Scientific, Dreieich, Germany
Inverted optical microscope	Zeiss Axio Observer	Carl Zeiss, Oberkochen, Germany
	DM IL	Leica, Witzlar, Germany
Light optical microscope	Axiolab	Zeiss, Jena, Germany

Light optical microscope II		Kern& Sohn, Ballingen, Germany
Liquid nitrogen tank	MVE Cryosystem 6000	ThermoFischer Scientific, Dreieich, Germany
	LS 6000, RS series	Taylor-Wharton, Husum, Germany
Magnetic sorter	VarioMACS	Mitnenyi Biotec, Bergisch Gladbach, Germany
Magnetic stirrer	RCT	IKA,Staufen,Germany
Microwave	Inverter	SHARP, Cologne, Germany
MilliQ water purifier	Purist	Rhephile, Germany
Particle counter	Z1	Beckman Coulter, Krefeld, Germany
pH meter	pH 7110	WTW, Weilheim, Germany
Pipettes	P2 /P10/P20/P1000	Gilson, Limburg an der Lahn, Germany
Pipetus	forty	Hirschmann, Eberstadt, Germany
Adaptors for silicon tubing	Elbow connector	Ibidi, Munich, Germany
	Luer connector male	Ibidi, Munich, Germany
	Luer lock connector male	Ibidi, Munich, Germany
	Luer lock connector female	Ibidi, Munich, Germany
Silicon tubing		
Shaker	KS 501 digital	IKA, Staufen,Germany
Spectrophotometer	UVIKON 923	Kontron instruments, Munich, Germany
Sterile work bench	Herasafe	ThermoFischer Scientific, Dreieich, Germany
	SterilGard Class II	The Baker company, Sanford, ME,USA
	BioGard Class II	The Baker company, Sanford, ME,USA
Thermocycler	GeneAmp® PCR System 9700	PE Applied Biosystems,
TIRF microscopes	Zeiss Axiovert200M, ASI MS-2000 stage, Objective: alpha Plan-Apochromat 100x/1.46, Orbital TIRF	Carl Zeiss, Jena, Germany
	Nikon Ti2, PFS 4th generation, Objective: Nikon Apo TIRF 60x NA 1.49, Orbital TIRF	Nikon GmbH, Düsseldorf, Germany
	Zeiss Axiovert, Objective: Olympus Apo TIRFM 60X/1.49 w/Corr. Collar, Orbital TIRF	ZEISS, Jena, Germany

UV chamber	GS Gene linker	Bio-Rad, Munich, Germany
Vortex	Genie 2	Scientific industries, Bohemia, NY, USA
Waterbath	MP	Julabo, Seelbach, Germany

2.1.2 Disposable material

µ-slide VI$^{0.1}$	Ibidi, Gräfelfing, Germany
µ-slide VI$^{0.4}$	Ibidi, Gräfelfing, Germany
µ-slide VI$^{0.5}$	Ibidi, Gräfelfing, Germany
AFM cantilever NP-S10	Brucker, CA, USA
Aluminium foil	Carl Roth, Karlsruhe, Germany
Cell culture plate	Greiner bio-one, Frickenhausen,Germany
Centrifuge polypropylene (Cellstar) tubes (14 ml, 50 ml)	Greiner bio-one, Frickenhausen,Germany
Coverglass 15 mm	Marienfeld, Lauda-Königshofen, Germany
Filter systems	Corning, Kaiserslautern, Germany
Filters Millex (0.22 µm)	Merck Millipore, Darmstadt, Germany
Filters Millex (0.45)	Merck Millipore, Darmstadt, Germany
Gloves	Ansell, München, Germany
MACS CS column	Miltenyi Biotec, Bergisch Gladbach, Germany
Parafilm	Bemis, Londonderry, UK
Petri dishes (60mm, 100mm, 145 mm)	Greiner Bio-one, Frickenhausen,Germany
Pipette tips	Corning, Kaiserslautern, Germany
Plastic pipettes (1 ml, 2ml, 5 ml, 10 ml, 25 ml, 50 ml)	Corning, Kaiserslautern, Germany
Polystyrene round bottom tubes (5ml)	Corning, Kaiserslautern, Germany
Precision wipes (11x21 cm)	Kimberly Clark, Mainz, Germany
Water bath	

2.1.3 Kits

DNase free kit	Invitrogen, ThermoFischer Scientific, Vilnius, Lithuania
Super Script II first strand synthesis	Invitrogen, ThermoFischer Scientific, Vilnius, Lithuania
EuroTaq Polymerase kit	BioCat, Heidelberg, Germany

2.1.4 Chemicals

2.1.4.1 *Antibodies*

Antibody	Description	clone	Clonality	Company	Use

Alexa Fluor 488 anti-mouse IgG	Goat anti-mouse		Polyclonal	Invitorgen, ThermoFischer	IF
anti-CD54 (ICAM-1)	Mouse anti-human		monoclonal	BioRad	IF
Alexa Fluor-547 anti-human IgG	Mouse anti-human		Polyclonal	Invitorgen, ThermoFischer	IF
Anti-CD54-FITC	Mouse anti-human	1H4	Monoclonal	Merck, Taufkirchen,Germany	IF
Streptavidin-547	AlexaFluor547-conjugated streptavidin				IF

2.1.4.2 Recombinant proteins

Protein	Company	Use
G-protein	Abcam	Surface functionalization
Fc-ICAM	Biolegend,	Surface functionalization
Neutravidin	ThermoFischer	Surface functionalization

2.1.4.3 Dyes

Dye	Ex/Em (nm)	Company	Use
Ethidium bromide	360/590	Roth	DNA staining
Giemsa stain		Roth	Parasite visualisation within host
CellBrite$^{\text{TM}}$, Membrane stain	515/612	Biotium	Cell membrane staining of human erythrocytes

2.1.4.4 Size markers

GeneRuler 1Kb plus DNA ladder (Ambion-Thermo Fisher Scientific, Dreieich Germany).

2.1.5 Organisms and primary cells

Chinese hamster ovary cells, ICAM-1 expressing	Gifted by Arthur Scherf, Director of Institute de Pasteur
Plasmodium falciparum FCR3 strain, IT2 variant	Gambia [],

Rosetting plasmodium falciparum strain	Gifted by Prof. Alexandra Rowe, patient isolate-lab adapted
IT2 variant, ICAM-1 selected	Gifted to us by the lab of Prof. Alistair Craig

2.1.6 Oligonucleotides

N°	Sequence	Concentration	Company
52,rev	TT TGA ATT TCC CTT TTT ATT TCC		Eurofins
63,for	ATG AAA TTC GCA AGT AAA AAA AAT AAT C		Eurofins
Bottom-TGT (12 pN)	/5BiosG/TT TTT TTT TTC ACA GCA CGG AGG CAC GAC AC	250nM	IDT technologies, Coralville, IO, USA
Bottom-TGT			
TGT-cy3 (12pN)	5´- GTG TCG TGC CTC CGT GCT GTG/3cy3Sp/	250nM	IDT technologies, Coralville, IO, USA
TGT-Atto647		250nM	IDT technologies, Coralville, IO, USA
SS-TGT (12pN)	5`-GTG TCG TGC CTC CGT GCT GTG/3ThioMC33-D/	250nM	IDT technologies, Coralville, IO, USA
SS-TGT (56pN)		250nM	IDT technologies, Coralville, IO, USA
SS-TGT (12pN) (2)		250nM	IDT technologies, Coralville, IO, USA

2.1.7 Buffers and solutions

2.1.7.1 P. falciparum cell culture

Complete culture medium	RPMI 1640 (Gibco) medium supplemented with 2 mM L-glutamine, 25 mM HEPES, 100 µM hypoxanthine, 20 µg/ml gentamicin and 10% (v/v) human serum
Albumax® culture medium	RPMI 1640 medium supplemented with 2 mM L-glutamine, 25 mM HEPES, 100 µM hypoxanthine, 20 µg/ml gentamicin, 5% (v/v) human serum, 25mM Albumax® (Gibco) and 10mM Glucose
Freezing solution	6.2 M Glycerol, 140 mM Na-Lactat, 0.5 mM KCl, pH 7.2 adjusted with 0.5 M of NaHCO3 at pH =9
Thawing solution I	12% (w/v) sodium chloride

Thawing solution II	1.8% (w/v) sodium chloride
Thawing solution III	0.9% (w/v) sodium chloride
Sorbitol lysis solution	280 mM D-sorbitol, 0.1M PBS, Heat sterilized
MACS buffer	0.1 M PBS, 2mM EDTA, 0.5% (w/v) BSA
Gelatine solution	0.5% (w/v) gelatine (from porcine skin type A) in RPMI 1640 supplemented with 2mM L-glutamine and 25mM HEPES
RPMI incomplete	RPMI 1640, 2 mM L-glutamine, 25 mM HEPES
Binding buffer	RPMI 1640, 2 mM L-glutamine, 25 mM HEPES, pH=7.2

2.1.7.2 Immunofluorescence methods

FACS buffer	0.1 M PBS, 2% (v/v) FCS
ICAM-1 solution	0.9 mM ICAM-1 in 0.1 M PBS
α-ICAM-1-FITC solution	1000 U/ml in 0.1M PBS

2.1.7.3 Surface preparation chemicals

Chemical	Company	Use
APTES		Surface aminization
CHO-PEG5000-NHS		Bulk pegylation
MAL-PEG$_{5000}$-SVS	LaysanBio, Arab,AL, USA	Crosslinker
MAL-PEG$_{5000}$-biotin	LaysanBio, Arab,AL, USA	Biotin functionalization of surface
Sulfo-SMCC	Life technologies, Darmstadt,Germany	Crosslinker

2.1.7.4 Electrophoresis solutions

DNA/RNA

TAE buffer 1x	40 mM tris, 20mM acetic acid, 1 mM EDTA
DNA loading buffer 20x	60% (v/v) glycerol, 60 mM EDTA / 2.5 mg/ml Bromophenol blue
RNA running buffer (10x)	
RNA loading dye	

2.1.8 Beads

Name	Coating	Magnetic	Size	Company
Dynobeads	A-Protein	Yes	2.8 µm	ThermoFischer Scientific

QSC Microspheres	Fc-specific capture Ab (3/6 kit concentrations)	No	6-9 µm	Bang Laboratories Inc, Quantum ™ Simply Cellular ®

2.1.9 Computer software and databases

Program	**Company**
Adobe Illustrator	Adobe ®
Cellquest	Becton and Dickinson, Heidelberg, Germany
EndNote X9-10	Clarivate™, London, UK
FIJI	National Institute of Health, Bethesda, MD, USA
Flowing Software 2	Turku Bioscience, University of Turku, Finnland
JPK	JPK Instruments, Berlin, Germany
Microscope VIS	Kern and Sohn,
LSM imaging software	Zeiss, Jena, Germany
ImageJ 2.0	LOCI, Neubias &Wisconsin university, USA
SigmaPlot 14.0	Systat, CA, USA
Resolve3D	Soft worx-Aquire, Version 5.6
VisiView imaging software	Visitron, Puchheim, Germany

2.2 Methods

2.2.1 Ethical clearance

This study was approved by the ethics committee of Heidelberg University, Mannheim University Hospital and the Biomolecular Research centre (CERBA/Labiogene). Blood samples were collected by venipuncture after obtaining written consent from volunteers.

2.2.2 Blood collection and genotyping

Whole blood was collected by venipuncture into citrate tubes and centrifuged at 800xg for 10 min at RT. The erythrocyte pellet was washed with RPMI1640 medium supplemented with 2 mM L-glutamine and 25 mM HEPES. Packed erythrocytes were stored at 4 °C prior to use. Packed erythrocytes were used within 2 weeks after collection.

2.2.3 Cell culture methods

2.2.3.1 P. falciparum cell culture

Plasmodium falciparum IT2 variant was cultured in HbAA and HbAS erythrocytes as described previously reference. Shortly, cultures were maintained at 3.7 % haematocrit, in RPMI 1640 media supplemented with 2 mM glutamine, 25 mM HEPES, 100 µM Hypoxanthine and 20 µg/ml gentamycin. Parasitemia was kept below 5 % and the parasites were continuously cultured at 37 °C under controlled atmospheric conditions (3 % CO_2, 5 % O_2, 92 % N_2, 95 % humidity).

2.2.3.2 Rosetting culture

A *P. falciparum* strain that forms clusters with uninfected erythrocytes (rosettes), donated to us by Alexandra Rowe of Edinburgh University, was cultured in HbAA erythrocytes as previously described reference. In short, cultures were maintained at 3.5 % haematocrit and no higher than 5 % parasitaemia. RPMI-1640 (Gibco) culture medium was supplemented with 2 mM L-glutamine, 20 mM glucose, 25 mM HEPES (Gibco), 20 µg/ml gentamycin, 100 µM hypoxanthine and 5 %v/v A+ human serum and 0.25 % v/v Albumax (Gibco). Cultures were grown at 37 °C under controlled atmospheric conditions (3 % CO2, 5 % O2, 92 % N_2, 96 % Humidity).

2.2.3.3 Estimation of the parasite development and multiple infectivity

In order to determine the percentage of parasitized erythrocytes, the developmental stage of the parasite and the occurrence of multiple infectivity, thin blood smears were made. To this end, approximately 50 µL of concentrated blood in culture were spread and air-dried on glass slides and fixed in 100 % methanol for 20 s. These were then air-dried and then stained in 2 % Giemsa solution for 10 min and rinsed with de-ionized water to remove excess staining. The stained thin blood smear was observed under a light microscope, using an oil immersion lens at 100x magnification.

Multiple infection is defined as an erythrocyte containing ≤ 2 parasites. The number of multiply invaded erythrocytes in a total of 500 parasitized cells per slide was counted to provide the rate of multiple infectivity (PMI). The percentage of single, double, triple, quadruple or higher infections were quantified for rosetting cultures at different developmental stages (rings to schizonts).

2.2.3.4 Rosetting frequency

A rosette is defined as at least one infected erythrocyte that adheres firmly to two or more uninfected erythrocytes. Rosetting frequency was counted using a wet slide (20 µL of culture) at 50x magnification and observation through a light microscope, counting at least 500 infected erythrocytes. The percentage of those infected erythrocytes forming a rosette was calculated, giving the rosetting frequency.

2.2.3.5 Synchronization of parasite culture

5 % *D*-sorbitol solution was used for synchronization of parasites at ring stages following the protocol of Lambros and Vanderberg (1979) [187]. Briefly described, after a centrifugation step (1900 rpm, 2 min, RT), 5x its volume of sorbitol solution was added to the pellet, gently resuspending it. The suspension was incubated for 5 min at 37 °C and then centrifuged (1900 rpm, 2min, RT) to isolate ring stage parasites and non-infected erythrocytes found in the pellet from later stages that are hypotonically lysed by sorbitol and found in the supernatant. The pellet was washed once with 1x

PBS solution, centrifuged (1900 rpm, 2min, RT) and then restored to normal culture conditions. While only stages younger than 18 hours post invasion (hpi) survive this treatment, synchronization can be achieved by repeating this protocol after a 12 to 14 h window, depending on the range that is required.

2.2.3.6 Gelatine flotation

A cruder method of synchronization and selection of late stage parasites with higher knob densities is based on the slower sedimentation of the latter in a heated gelatine solution^[188]. This method was used with both rosetting strain and IT2 but to different ends.

This protocol enables the separation of uninfected erythrocytes, ring stage parasites, knobless parasitized erythrocytes and rosettes from knobby late-stage parasites, specifically trophozoite (24-36 hpi) and schizonts (36-48 hpi). In short, cells are pelleted via centrifugation (1900 rpm, 2 min, RT) and the pellet was resuspended in 10x volume of gelatine (0.5 %, experimentally determined value). The mixture was incubated at 37 °C for 1 h.

If rosetting parasites were used for this protocol, the supernatant was removed and the pellet was washed twice in 1x PBS (10x volume) and pelleted cells (1900 rpm,2 min, RT) were restored to normal culture conditions. This protocol was performed every two weeks to ensure >50 % rosetting frequency.

If FCR3 parasites (IT2 strain) were used with the intention of selecting knobby infected erythrocytes with latestage parasites, 2/3 of the supernatant were removed and placed in a falcon tube. After a washing step using 1x PBS to remove gelatine remnants, only mature stage, knobby parasites were resuspended in complete cell culture media and restored to normal culture conditions.

2.2.3.7 Magnetic Cell Sorting (MACS)

A more effective method of late stage parasite enrichment is the use of Magnetic Cell Sorting (MACS). Parasites metabolize heme into hemozoin crystals in the food vacuole as haem is toxic to the parasite. These crystals are paramagnetic and when present in higher concentration, can ensure the retention of parasitized erythrocytes in a metal wool column, in the presence of a magnetic force. As a result, mature stages, which have a higher rate of hemozoin crystal production, are retained in the column when surrounded by a magnet, while non-infected erythrocytes and early-stage parasites flow through.

Shortly, the steel wool column was equilibrated with MACS buffer for at least 20 min, and 14 ml of culture were gradually allowed to pass through the column in the presence of a magnet at a flow rate of maximally 0.5 drop/sec. MACS buffer was added until the flow through turned from red to clear (free of erythrocytes). The column was then removed from the magnetic force and the retained cells were eluted into a falcon tube.

The eluted cells were centrifuged at 1900 rpm, for 2 min at ambient temperature and resuspended for further experiments in either culture medium or binding buffer.

2.2.3.8 Cryopreservation of parasites

Freezing of *Pf* parasites for cryopreservation is only possible for young ring stages, due to the higher elasticity of the membranes that can survive the cycle of freezing and thawing. Monitoring the stage before cryopreservation is therefore critical. Once in the right stage and in high parasitemia, the cells were centrifuged at 1900 rpm for 2 min and the supernatant was discarded. Approximately 1.5 ml of freezing solution, was added slowly, under continuous shaking to the pellet and the mixture was aliquoted into suitable cryovials at maximum 1.5 ml. The vials were first placed at -80°C overnight and then transferred to long-term storage (liquid nitrogen tank).

2.2.3.9 Thawing of parasites

Frozen parasites were stored in cryovials at maximum volume of 1.5 ml. Once removed from liquid nitrogen storage, the vials were shortly warmed at 37 °C. The thawed cells were transferred to a falcon tube and 200 µL of thawing solution I were added slowly dropwise. After 5 min of rest, 9 mL of thawing solution II were added slowly and once the mixture is homogeneous, it was centrifuged at 1900 rpm for 2 min, at ambient temperature. The supernatant was removed and 7 ml of thawing solution III were added to the pellet, under constant gentle shaking. The mixture is centrifuged with the same conditions one more time. The pellet is resuspended gently with complete cell culture media and restored to normal culture conditions.

2.2.3.10 Haemoglobin variants infection

Tightly synchronized parasites at trophozoite stage (26-32 hpi) were magnetically enriched as described above (section 2.2.3.7) in a sterile environment. Eluted trophozoite stage parasites were washed with serum-free culture medium and added to HbAS erythrocytes in culture media containing AB serum. The parasites were cultured to approximately 2 % parasitemia and the haematocrit was kept at 3.5 % at all times. Parasite invasion and development were monitored with thin blood smears and cultures only used AS blood for up to 2 weeks per batch.

2.2.4 Adhesion assays

2.2.4.1 Selection with recombinant ICAM-1

Use of recombinant ICAM-1, as a soluble protein for selection is a more efficient selection method for adherent parasites, as the presence of other proteins on CHO-cells or endothelial cells cannot be excluded.

In short, synchronized IT2/IT4$_{\text{ICAM-1}}$ at approximately 5 % parasitemia, were selected via gelatine flotation (section 2.2.3.6) and resuspended in RPMI binding buffer. On a petri dish, 20 µL spot of recombinant ICAM-1 (ThermoFischer Scientific) in a 10 µg/ml concentration was incubated at 37 °C for 1 h and washed with 1x PBS, at least five times. 1 % BSA solution was used for blocking and incubated for 30 min at 37 °C. The spots were carefully washed with incomplete RPMI medium (RPMI 1640 without serum) and the concentrated yield of gelatine-enriched IT_{ICAM-1} cultures was resuspended in binding buffer and incubated in the ICAM-1 spotted petri dish for 1 h at 37 °C. During incubation, the parasites were carefully rotated clockwise and counter clockwise every 10 min. Cells were washed carefully with RPMI incomplete medium at least 5 times by gently rocking the petri dish to remove any unbound cells. Adherent cells were then washed off by directly aspirating warm binding buffer to the spots and restored to normal culture conditions.

The binding capability of parasite lines was monitored by static binding adhesion assays. Once a high binding population was obtained all further assays were performed. This protocol was performed repeatedly in combination with gelatine-enrichment at least 5 consecutive times before use in other assays.

2.2.4.2 Static adhesion assay

Recombinant ICAM-1 (6xHis) (ThermoFischer Scientific) in 10 µg/ml was spotted in 20 µl droplets on a petri dish for 1 h at room temperature. In parallel, 1 % BSA and CSA (1 mg/ml) 20 µl droplets were incubated in the same dish. After washing each spot carefully with 1x PBS, MACS purified IT_{ICAM-1} parasites were added in a 10^6 concentration to each spot and incubated for 1 h, at room temperature with frequent gentle rocking. The non-adherent cells were washed off with warm (i.e. 37 °C) 1x PBS by adding the solution away from the spots and gently rocking. This was repeated for at least 5 rounds and remaining cells were fixed with 2 % (v/v) glutaraldehyde solution. After 30 min, the fixing solution was washed off with 1x PBS at least two times and stained with Giemsa solution for 15 min at room temperature. Fixed cells were observed in an inverted microscope, with a 20x air objective (KERN, KERN and Sohn, Germany). At least three different fields of view of each spot were captured in brightfield and calculated using Fiji (ImageJ 1.53p). Statistical analysis was performed using SigmaPlot v14.

2.2.4.3 FACS

Flow cytometry is a sophisticated analytical technique that is based on the principle of fluorescence emission and light scattering by cells as they flow in liquid. Depending on the characteristics of the cell and its components as well as the fluorescent labels attached to them, the laser light scattering and fluorescent light emission varies. This is recorded using highly sensitive detectors and allows cell sorting based on physical, biochemical and antigenic traits. Fluorescence activated cell sorting (FACS) can sort up to 300000 cells per second to a very high purity by fluorescently labelling the component that sets apart a subgroup from the total cell population. This population is passed through a narrow channel, one cell at a time and allows for a rapid, accurate and simple measurement of multiple parameters in a heterogeneous mixture.

To verify the presence of ICAM-1 binding receptors for IT_{ICAM-1} parasites, MACS purified infected erythrocytes were washed with PBS and centrifuged at 1400 rpm, for 5 min at ambient temperature. The pellet was collected and resuspended in FACS buffer (1x PBS and 10 % FCS) and counted using a Neubauer chamber. Independent of volume, 10^6 cells were used per staining condition. Parasitized erythrocytes were incubated with 1 ml of ICAM-1 recombinant (10 µg/ml, ThermoFischer Scientific) for 1 h at 37 °C under constant rotation (3 rpm). After washing with 1x PBS and another centrifugation step, the pellet was incubated with mouse anti-ICAM-1 polyclonal antibody in a 1:50 dilution for 30 min in the dark at ambient temperature. The cells were washed with FACS buffer and centrifuged (1400 rpm, 3 min, RT) and goat anti-mouse-Alexa488 in a 1:500 dilution was added for 30 min in the dark at ambient temperature. Labelled cells were then washed with FACS buffer and after one more centrifugation (1400 rpm, 3 min, RT), 2 % formaldehyde in PBS was added to fix them. Always non-labelled and non-fluorescently labelled cells were used as a negative control. These samples were measured at the same fluorescence intensity (Ex: 488 nm, Em: 575 nm) and the corresponding clustering was recorded as a histogram and compared. Post-analysis was performed using CellQuest software or Flow software.

2.2.5 Flow chamber assays

2.2.5.1 Rosette flow chamber assay

Flow chamber measurements were performed as described reference. Briefly, a TCP parallel flow chamber (µ-slide VI 0.1, Ibidi) was glued to a high-resolution glass slide (#1.5, ROTH) using freshly prepared and de-gassed PDMS glue (Silgard^{TM} Silicone Elastomer Kit). BSA (1 % w/v,) was added to the channel and incubated for at least 30 min at RT prior to the experiment. The channel was washed twice with RPMI incomplete media (pH= 7.2, RPMI 1640, Gibco) and mounted on the stage of an inverted microscope (63x magnification, ZEISS, AxioObserver).

Rosettes were separated from the culture using magnetic purification and stained with CellBrite Red membrane dye (Biotium). These cells were adjusted to 10^6 cells/ml in incomplete RPMI medium (pH= 7.2). A total volume of 5 ml cell suspension was perfused at 0.05 Pa wall sheer stress, using the Harvard Apparatus syringe pump connected via silicon tubing with the flow chamber inlet. Measurements in high haematocrit were performed after the addition of packed HbA erythrocytes to the cell suspension and a total volume of 5 ml with 40 % haematocrit was perfused at 0.05 Pa wall sheer stress into the flow chamber. The cell flow was recorded either in Brightfield for low haematocrit or by recording the CellBrite signal with high frame rates (250-1000 fps) using a Zeiss inverted microscope (Axio Observer, 63x magnification, Ex/Em: 644/665, Cy5 filter set) and a high-speed camera (FastCam, Photron).

While recording, the coordinates of the microscope stage could be tracked and were adjusted to correspond to the position of the recorded field within the chamber. Scanning through the height of the channel in 20 µm steps allowed to track the position of rosettes within the channel as well as along the length of the channel between inlets (12 mm).

2.2.5.2 ICAM-1 functionalized flow chamber assay

2.2.5.2.1 Surface functionalization

The flow chamber channels were functionalized for flow assays as follows: Glass slides were incubated in APTES (1:100 in ethanol) for 1h at RT. After several washes with ethanol, the slides were dried with nitrogen gas, sealed with parafilm and stored at -20°C until use. Ibidi µ-slide channels (Ibidi, µ-slide VI0.4) were glued to one glass slide, using PDMS glue. A mixture of PEG_{5000}-NHS/MAL-PEG_{5000}-biotin (1:100, 2 mg/ml) was added to introduce anchoring points for neutravidin (500 µg/ml, 2 h, RT). G-protein (1 mg/ml) was incubated with SMCC crosslinker (2 mg) for 30 min at RT. In parallel, the top-oligonucleotide strand (IDT technologies) was incubated with TCEP for 20 min and then centrifuged at 13000 xg for 10 min in a centrifugation column (Miltenyi). The two solutions were then combined and allowed to react for 30 min at RT. 300 nM of biotin-functionalized bottom oligonucleotide were then added and the mixture was heated at 75 °C, for 5 min to allow the strands to anneal and then added to each channel, for 2 h incubation at RT or 4 °C, overnight. A chimeric Fc-ICAM-1 was added (100 µg/ml) for at least 1 h at room temperature and then washed out with incubation buffer. The buffer used for all components, unless otherwise specified was 0.1 M PBS. To verify each step, respective fluorescent probes were used as follows. IgG-Alexa 488 (1:100, Invitrogen) was used for G-protein detection, streptavidin-Alexa647 was used to detect biotin and probe coupled oligonucleotide (Atto-647) was used to determine annealing of the strands and their anchoring to the substrate.

2.2.5.2.2 Flow chamber experiment /Footprinting flow assay

ICAM-1/TGT chambers were prepared (Ibidi, µ-slide $VI^{0.4}$) as described in section 2.2.5.2.1 and mounted on an AxioObserver Z1 inverted microscope. Tightly synchronized ICAM-1 selected parasites were magnetically enriched, and counted using a cell counter (Beckman Coulter) to adjust to $2x10^6$ cells/ml density in binding medium. 200 µL were perfused over the surface at 0.03 Pa WSS. The cells were allowed to settle for 5 min and then washed with binding medium at the same WSS rate for 5 min. The flow was controlled using a syringe pump (World Precision Instruments) attached to the channel via silicon tubing (Ibidi) and RICM images were recorded as described in section 2.2.10.

Anti-ICAM mouse antibody and anti-mouse goat-Alexa547 were added to control for the presence of ICAM and 300 nM of complimentary oligonucleotide probe (IDT technologies, Atto647/ cy3) were added to detect the footprints of trophozoite stage or schizont stage parasites. For each condition, the fluorescence signals were recorded in at least 6 different fields across the channel using orbital TIRF (section 2.2.9) (TIRF filter 546 Ex/Em: 513/580 nm or TIRF-filter 647 Ex/Em: 615/660 nm, 100x-TIRF lens, ZEISS) (Carl Zeiss). Trophozoite stage (24 hpi) and schizonts (42 hpi) infected HbAA and HbAS cell tracks i.e. footprints, were compared. Developmental stage was monitored with thin Giemsa-stained blood smears. Control experiments were performed with non-infected erythrocytes under the same conditions.

2.2.6 Molecular biology methods

2.2.6.1 Var gene transcriptional profile

The transcriptional profile of var genes was determined as follows: Shortly, total RNA was collected from ICAM-1 selected cultures in trophozoite stages (~24 h post invasion) using TRIzol (Invitrogen), following the manufacturer's instructions. The parasite culture was selected at least 7 times and at least once within 2 cycles before this protocol was applied. The cells were centrifuged (1900 rpm, 2 min, 4 °C) and the pellet was lysed in cold saponin lysis solution (0.1% (w/v) in PBS, 4 °C). The lysate was carefully mixed and centrifuges at 3400 rpm for 8 min at 4 °C to pellet only infected cells. After a wash with 1xPBS the pellet was further processed with addition of TRIzol (10x the pellet volume) and immediately stored at -80°C.

The TRIzol treated cell lysate was thawed at 37 °C and vortexed to ensure adequate mixing. To 1 ml aliquots of the lysate, chloroform (0.2 x the TRIzol volume) was added and vigorously mixed for at least 15 s and then allowed to rest at ambient temperature for 2 min before centrifugation (3800 rpm, 30 min, 4 °C). After this step, two phases form in each vial. The aqueous phase that contains RNA was carefully removed using a clean pipette and DNA/RNAase free tips and transferred into a fresh, DNA/RNAase free tube. RNA is precipitated using cold isopropanol (0.5 x the TRIzol volume, 4 °C). This reaction can be performed on ice for 30 min or overnight at -20 °C (slower precipitation ensures less contaminants co-precipitating). The vial is then allowed to thaw on ice if needed and centrifuged (3800 rpm, 30 min, 4 °C) in a RNAase free centrifuge. The pellet was washed with 75 % ethanol (1x the TRIzol volume), air dried for 10 min and resuspended in 20 µL of RNAase free water. If the pellet is not dissolving, incubation at 60 °C for approximately 10 min can facilitate it. RNA concentration and purity were spectroscopically defined. OD 260/280 ratio for a clean sample is in the range of 1.9 to 2.1 while concentration is defined by the following equation:

$$OD_{260} \times 40 \times \text{Dilution factor of sample} = \text{RNA concentration } (\mu g/ml)$$

RNA integrity was verified via RNA gel electrophoresis using RNAase free reagents (2 % agarose gel, 60 min, 100V) and visualized with ethidium bromide. Possible DNA contaminants were removed by DNase treatment, following the protocol provided by the manufacturer. RNA Superscript II (Invitrogen) was used following instructions by the manufacturer to transcribe cDNA from total RNA (≤ 5 µg initially). Concentration and cDNA purity were spectroscopically determined and samples were stored immediately at -80 °C until further use. cDNA integrity was tested before transport with the following PCR reaction:

Table 2.1: PCR conditions:

Reagent	Volume (µL)
5x PCR Buffer (200 nM Tris-HCl (pH=8.4), 500 mM KCl)	2.5
50 mM $MgCl_2$	1.25
2 mM dNTP Mix	2.5
Forward primer (10 µM)	0.5
Reverse primer (10 µM)	0.5
EconoTaq DNA polymerase	0.25
cDNA (10 %)	0.25
Autoclaved H_2O	10

Samples were heat denatured at 94 °C for 2 min and then the following PCR program was run for 30 cycles.

Table 2.2: PCR program:

	Temperature	Duration
1 cycle	94 °C	4 min
30 cycles	94 °C	45 s
	54 °C	45 s
	68 °C	45 s
1 cycle	68 °C	2 min
1 cycle	4 °C	∞

The resulting product was verified as cDNA via DNA electrophoresis in a 2 % agarose gel (90 V, 60 min) and visualized using ethidium bromide.

All real-time qPCR experiments were performed by Jean-Philippe Semblat under the supervision of Benoit Gamain (Inserm, Paris, France). Samples containing at least 6 µg of cDNA from selected cultures were provided. All reactions were performed on a BioRad CFX96 RealTime system using the 1:1 forward and reverse primer mix in a 1:10 ratio with SYBR Green labelled cDNA in water. In total 62 known primers corresponding to *var* genes were used and quantified.

2.2.6.2 *P. falciparum* genomic DNA extraction

IT2$_{ICAM-1}$ cultures were synchronized and collected at trophozoite stage at a parasitemia of at least 5 %. After centrifugation at 800 xg for 2 min at room temperature, the culture was washed with 1x PBS (4 °C) and lysed in 0.1 % (v/v) saponin for 3 min on ice, followed by a centrifugation at 2600 for 8 min. The pellet was washed three times with 1x PBS and resuspended in 200 µL of 1x PBS. The genomic DNA was isolated following instructions of the manufacturer. The genomic DNA was stored at -20 °C and integrity was assessed with 0.8 % agarose gel electrophoresis.

2.2.7 AFM measurement setup

2.2.7.1 CSA immobilization

PBS (0.1 M) was used to dissolve CSA (2 mg/ml final concentration). Droplets of 70 µL were spotted onto the glass surface of a petri dish (Glass bottom dishes, MatPak, USA) and incubated overnight at 4 °C. Spots were washed with 70 µL of PBS (0.1 M) at least three times at RT. A BSA (1 mg/ml) solution was used for blocking (1 h, RT). The spots were washed with PBS once more. This was done shortly prior to the measurement. The surface was covered by PBS (0.1 M) during the measurement.

On a different approach, I introduced a biotin-functionalized lipid bilayer (DOPC/DOPE-biotin, 0.5 mg/ml). After at least 1 h of incubation at RT, neutravidin (0.5 mg/ml) was added and allowed to adhere to biotin for 1 h at RT. CSA molecules crosslinked to biotin were then added to the surface and allowed to interact for at least 1 h at RT or at 4 °C overnight. Every step was followed by extensive rinsing (at least 5x with PBS, 0.1 M).

In order to crosslink CSA to the substrate, EDC/NHS was used as a crosslinking agent. A glass surface containing free amine groups was prepared, using either a hydrogel or an APTES coating (1:100 in ethanol). EDC/NHS (1:2.5 ratio) in MES buffer (0.1 M, pH= 5.4) were allowed to react with CSA (200 µg/ml) for 15 min. This reaction mixture was then added to the NH_2- containing surface and allowed to react for 2 h at RT in PBS (pH= 7). The surfaces were washed extensively with PBS (pH= 7) and glued to a petri dish.

2.2.7.2. VAR2CSA immobilization

NSP-10 cantilevers (Bruker) were coated with (3-Aminopropyl)triethoxysilane (APTES, 1:10 in ethanol) for 30 min. In order to accelerate the reaction a drop H_2O and a drop of thriethylamine was added to the mixture. After washing (ethanol, 3x), the cantilevers were dried at 80 °C for 30 min and stored in a sealed container for further use. Maleimide-Polyethylenglycol$_{5kDa}$-succinimidil valerate (Mal-PEG-SVA) was diluted in PBS (2 mg/ml) and added directly to the cantilevers (70 µL droplets) for 30 min. After a washing step (70 µL PBS, 0.1 M), a solution of spycatcher protein (100 µg/ml), was diluted (100 pg/ml, PBS) and directly added to the cantilevers. After 1 h incubation at room temperature, the cantilevers were washed with PBS. The spy-tagged VAR2CSA minimal binding region (DBL1-ID2) was diluted in PBS (100 pg/ml) and added to the cantilevers (70 µL/ cantilever). After 1 h of incubation at room temperature (RT) or overnight incubation at 4 °C, the cantilevers were washed and used within 2 days for measurements.

2.2.7.3 AFM microscope setup measurement

Using a JPK Bruker BioAFM atomic force microscope, we inserted the cantilever onto a glass AFM head with one side of at least one preferably two functionalized tips protruding. Using the JPK software, the softest tip (lowest k constant) was put in focus of the camera and slowly sunk into the liquid. Using a slow approach speed (15 µm/s) the surface was detected, with parameters suggested by the manufacturer and a setpoint of 1 nN. In order to minimize drift, we allowed the system to equilibrate for at least 20 min in RT. During this time, the laser was adjusted onto the cantilever in such a way that the vertical and lateral diffraction sum was the highest possible (>1 V).

All cantilevers were calibrated at a setpoint of 0.3 nN to determine the sensitivity (nm/V) and spring constant (k= N/m). For all measurement we used a stepwise approach-retract cycle, with a setpoint of 200-500 pN, resulting in 100-300 force-distance curves. A grid of approximately 20 by 20 µm, with each point´s measurement repeated 10 times. The exact number of obtained curves was determined by the amount of repetitions and the size of the grid (eg. 10x repeated, 5x6 points would result in 300 measurement points).

The approach speed was set to 1-2 µm/s, with an approach length of 500 nm and a sample rate of 2048 Hz. This step is followed by an extended pause between 0-1 s, while the height of the cantilever is kept constant. The cantilever is then retracted at 1-2 µm speed (corresponding to approach speed), 500 nm retraction length and 4000-10000 Hz sample rate. The last step is a short pause between this cycle, and the next set at 100 -500 ms and a sample rate of 2048 Hz.

2.2.7.3.2 Analysis and evaluation of measurements

The resulting force distance curves were analysed using a python script and information such as maximal force (Fmax), break away distance (Llast), distance where Fmax occurred (L), colloidal behaviour or peak/event occurrence were listed using an R script. The software that was used for this purpose was provided by Dr. Dimitris Missirlis and coded by Tamás Haraszti. These results were then grouped in histograms and data files in list formats, which were used to determine event occurrence and frequency for each measurement.

2.2.8. Scanning electron microscopy (SEM)

SEM was performed to resolve knobs presented on the surface of infected HbAA erythrocytes. MACS purified parasitized erythrocytes were fixed in 2 % (v/v) paraformaldehyde and glutaraldehyde solution in 1x PBS for 1 h at ambient temperature. Fixed cells were then loaded onto 0.01 % poly-L-lysine coated coverslips and washed with PBS three times. Samples were dehydrated by immersion for 10 min in a series of stepwise-increasing ethanol concentration solutions (30 %, 50 %, 70 %, 90 %, and 100%). Then slides were immersed in a 1:1 hexamethyldisilazan:ethanol solution for 5 min and overnight in hexamethyldisilazan. Dehydrated cells were sputter-coated with 10 nm gold/palladium (EM MED020 Leica, Germany) and viewed at 10000x magnification on a scanning electron microscope (Leo1530, CarlZeiss, Germany).

2.2.9 Total reflection interference microscopy

Total reflection interference microscopy (TIRF) setup that was used consists of a ZEISS Axiovert200M inverted microscope equipped with a cooled pE-4000 widefield illumination and alpha-Plan Apochromat 100x/1.46 oil-immersion objective. Orbital-TIRF images were captured with a Hamamatsu EMCCD 9100-50 camera.

Images obtained were evaluated using Fiji (ImajeJ version 1.53p) and the custom-made script of Dr. Pintu Patras.

The specifics of the analysis script exceed the scope of this thesis but in short:

Raw images are cropped using Fiji to isolate tracks and tiff files are run through with the script to obtain the parameters described in the next section.

2.2.9.1 Analysis of TIRF images

Track width

For each image, we average the intensity values along the x-axis, i.e., along the track's path, to get an average intensity profile. The profile contains the average intensity for each y-values along the image's width. A typical profile displays a peak centered close to the mid-width of the image. The profile decays towards the edges of the image to the background fluorescent intensity value (close to 20). To estimate the width of the track or the edges of the fluorescence profile, we set an intensity threshold (set manually for each image because of significant heterogeneity in the image data) whose intersection with the average intensity profile provides the width of the track. Next, we repeat the procedure to estimate the track width at each x-values. We calculate the intensity profile at each x-location. First, we smoothen the profile by taking 21 pixels (+/-10) bin around each x-value (and 5 pixels (+/-2) bin for x<10 and x>endpoint-10, i.e., a few pixels at the beginning and end points along the x-axis where 21 pixel is not possible). We smoothen the profile and compute the intersection points to estimate the local width of the track. Further, we use spatial information (values of intersection points from the previous pixel) to reject intersection points that are unrealistically far away (more than 5 pixels). Thus we get the width of the track from the images at each x-values along its path.

Intensity Autocorrelation:

First, we average the intensity values along the y-axis for each x-value. It leads to a profile I(x) for the image. Then we compute a function:

$$C(s) = \sum x\ [(I(x) - I\_mean) * (I(x+s) - I\_mean)]$$

where I_mean is the mean intensity and s ranges from 0 to 400 pixels. The spatial auto-correlation for profile I(x) is defined as:

$$C(s) = \mathrm{Val}(s)/C(0),$$

where C(0) is the value for s=0. The second peak of the auto-correlation defines the periodicity of the spatial pattern. The image is wrapped onto itself using the peak separation to create the 3D image, projected on a cylinder with mean diameter equal to 8 µm.

Patch size

To identify patches, which are the extended regions of high fluorescence intensities in the image, we use the Python library SciPy package Multidimensional image processing (scipy.ndimage). We first threshold the image to remove low-intensity region using a cutoff value of 150. Then we use ndimage.label feature to identify the objects (patches) in the image. Then we draw rectangles around the patches. Rectangles with small dimensions (e.g., width<50 and height<1) are not considered a patch. The remaining rectangles are considered patches.

2.2.10 Reflection Interference contrast microscopy (RICM)

RICM was performed using an AxioObserver Z1 inverted microscope equipped with a mercury-vapor lamp (HXP 120V, LEJ, Jena Germany) and a 63x/1.25 antiflex oil-immersion objective with a built-in quarter-wave plate. A green filter (546 nm) was used. RICM under flow conditions was performed viewing channels of Ibidi VI$^{0.4}$ at shear stress of 0.03-0.3 Pa and images were acquired at 100 fps.

Images were converted to stacks and evaluated using Fiji (ImajeJ version 1.53p).

3. Results

3.1 Aim 1: Adaptation of platform to visualize contact area for mature stage parasites in HbAA and HbAS *Pf* infected erythrocytes.

3.1.1 Selection of parasite strain and adhesion ligand

P. falciparum-infected erythrocytes are able to sequester to a multitude of receptors, mainly expressed on the surface of endothelial cells. As mentioned in section 1.5 receptors such as ICAM-1, CD-36, EPCR and CSA are established binding ligands for PfEMP1 receptors expressed on the surface of infected erythrocytes. The exact mechanism with which the parasites select these receptors and bind during infection, is still not fully understood, with field isolates showing multiple binding phenotypes and ligand preferences.

3.1.1.2 Static adhesion assays and selection process

Due to the absence of selective pressure, an *in vitro* cultured population expresses different *var* gene variants at any given time, similar to field isolates.

In order to select against the protein used in our platform, the *P. falciparum* strain IT2 (Gambia) was exposed for multiple rounds of selection to recombinant ICAM-1. Recombinant proteins were preferred in this approach, as they guarantee that the adhesion molecules are selected against only these specific cell surface receptors, rather than a multitude of receptors usually found on the cell surface. Following the protocol described in section 2.2., IT2-strain parasites were panned for at least 7 rounds in continuous culture. The yield of the first rounds of selection was very low for ICAM-1 and quite satisfactory for CSA. Initially, selection was performed using recombinant ICAM-1 with a 6x-Histidine tag, and at least eight rounds were needed to increase the yield of adherent parasites. The selected population was termed $\text{IT2}_{\text{ICAM-1}}$ and this term was used for all continuous cultures after at least six consecutive selection rounds of this strain. In order to characterize the binding preference of $\text{IT2}_{\text{ICAM-1}}$ to various receptors, I performed static binding assays regularly and used BSA (1 %) as a control (Figure 3.1).

To further characterize $\text{IT2}_{\text{ICAM-1}}$, I extracted total RNA and performed PCR amplification to provide two samples of gDNA as described in section 2. The first sample was taken from an $\text{IT2}_{\text{ICAM-1}}$ culture, two cycles after the 6th round of selection and the second sample two cycles after the 7th round of selection with His-ICAM-1. Jean-Philippe Semblat from the lab of Prof. Gamain, at the French National Institute of Health and Medical Research in Paris, performed q-RT-PCR on those samples and listed the *var* genes expressed in $\text{IT2}_{\text{ICAM-1}}$ cultures and the relative amount (in %) of each gene.

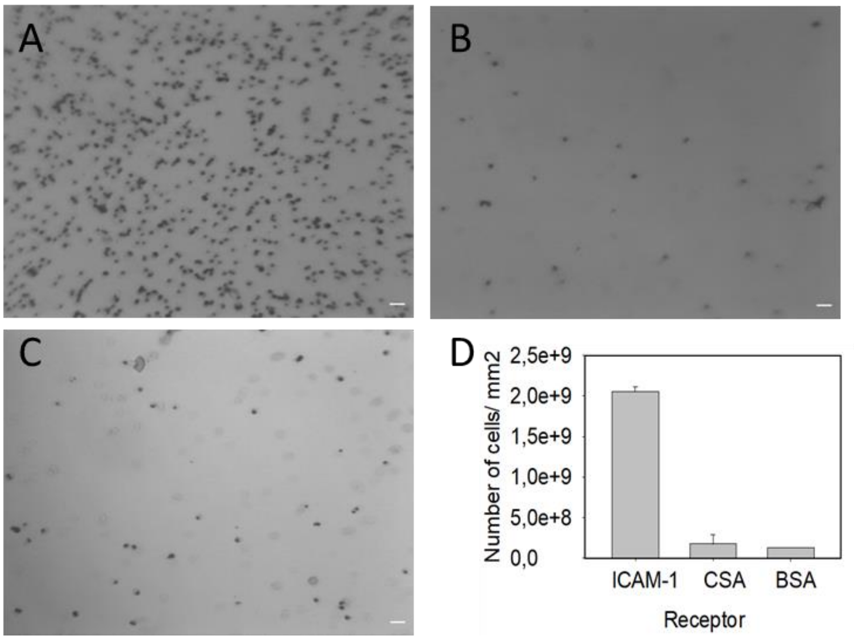

Figure 3. 1: Static adhesion assay of IT2 parasites against receptors. A) ICAM-1 and B) CSA as well as C) BSA as a control. D) Number of cells per mm^2 for all three receptors were counted for 5 individual squares of 5 mm^2 dimensions. Scale bar is 10 µm.

The *var* gene expression profile of IT2$_{\text{ICAM-1}}$ is too diverse to identify a single *var* gene that is primarily expressed to show preferential binding to any receptor, including ICAM-1. Based on information gathered for expressed *var* genes or genes that share a > 70 % identity when put through BLAST sequencing analysis most are classified into Group B & C *var* genes (Figure 3.2). The percentage of *var* gene transcripts remained constant for populations after six and seven rounds of selection respectively, with the highest percentage of a single *var* gene expression amounting to only 20 % of the total expression profile, for IT4var62 (Figure 3.3).

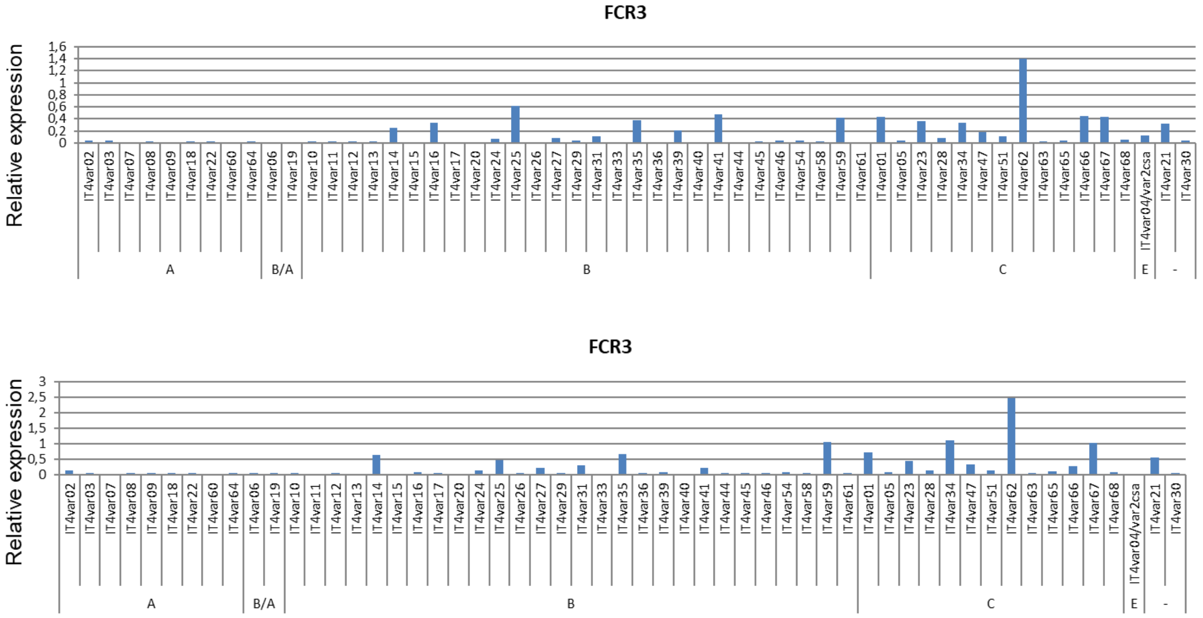

Figure 3. 2: Transcription profile and classification of *var* genes was assessed after multiple selection rounds in IT2$_{\text{ICAM-1}}$ parasites. Relative expression of *var* genes found in IT4 (Gambia) *Pf* strain (blue columns)

calculated by qPRCR and the results are normalised with the housekeeping gene seryl synthetase. Grouping of var genes into groups A,B,C and E is based on their Ups sequence and shown in the graph on the lower x axis.

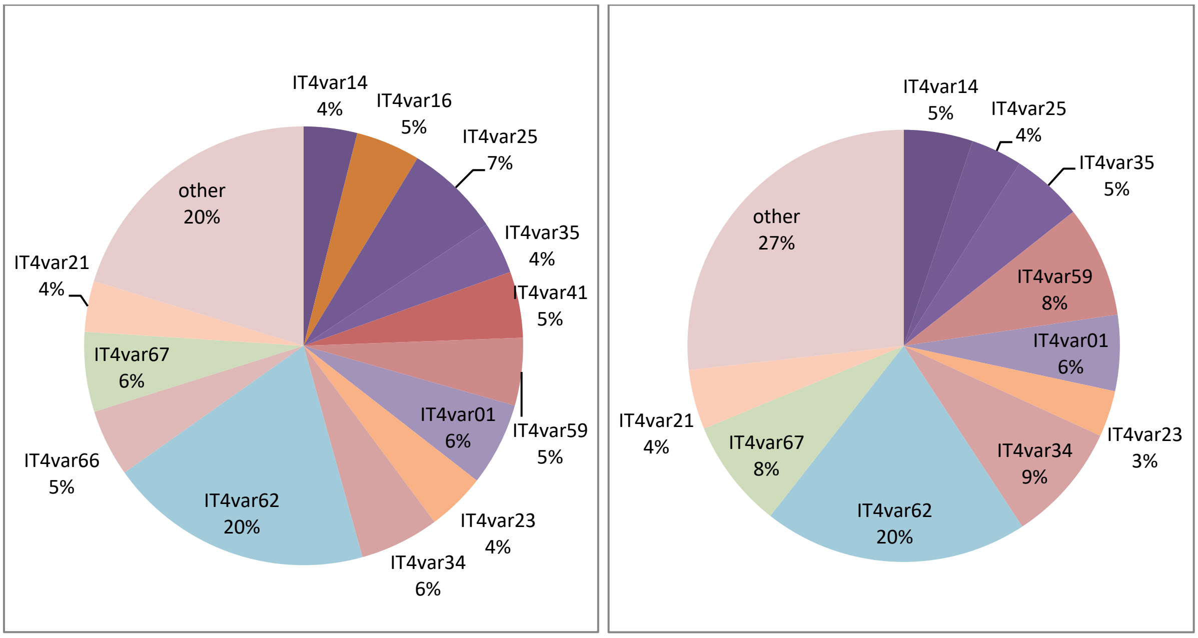

Figure 3. 3: Pie chart of *var* gene transcription profile in IT2ICAM-1 after multiple rounds of selection against ICAM-1 from two independent selection rounds (left and right).

Since expression levels were too low for any specific *var* gene and rather diverse within the selected culture, with no changes between selection rounds, the selection process was deemed unsuccessful.

It could be argued that seven rounds of selection are not sufficient to induce a more stable and less diverse expression profile for this IT2 strain. It seems selection was sufficient to diverge from var2CSA transcription but not as effective in selecting for an uniform transcription of an ICAM-1 binding PfEMP1. While static assays showed a preferred binding after round 8 of selection, the changes induced by a single round of panning are not drastic and shift to expression of different var genes at very low levels. IT4var59 (Group B, no information) and IT4var66 (Group C, non-binder [189]) expression increased by 3 % between rounds, while IT4var41 expression decreased to lower than 3 % expression. The amount of different *var* genes expressed at very low level, under 3 %, increased as well, showing that this selection protocol was ineffective and resulted in diversification of the expression profile rather than exerting selective pressure towards IT4var62. The levels of *var62* expression remained at 20 %, which while the highest percentage expressed, is still corresponding to only 1/5 of the population expressing this PfEMP1.

3.1.1.3 FACS analysis of binding specificity

Due to these issues, a different method for identifying effectively selected parasites is required, in addition to static adhesion assays. Therefore, I also performed FACS measurement using MACS purified parasites after selection. These were incubated as described in Section 2.2.4.3 with 6xHis-ICAM-1 as well as primary antibody against ICAM-1. To identify parasites able to adhere to ICAM-1, I also incubated with a fluorescently labelled secondary antibody and measured immediately after washing. While the percentage of ICAM-1 positive cells was high (71.8 %) compared to a sample of uninfected erythrocytes, the same percentage was gated for IT2$_{\text{ICAM-1}}$ parasites in the absence of ICAM-1 (Figure 3.4).

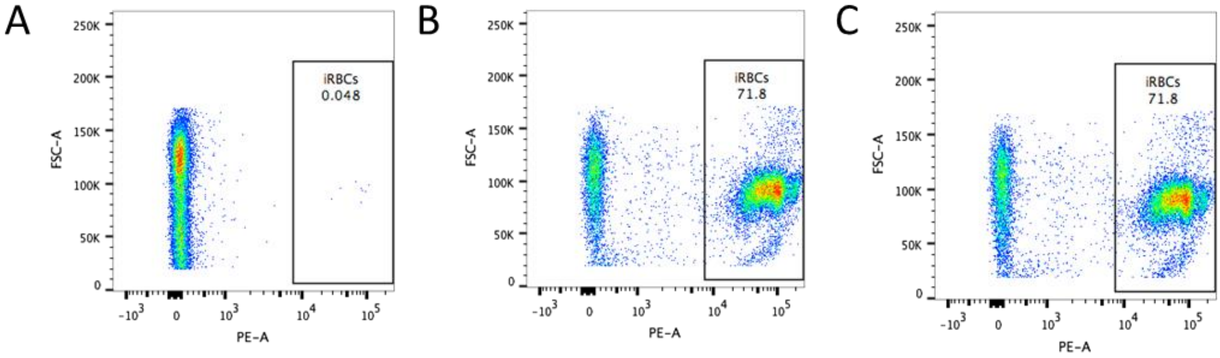

Figure 3. 4: Gated results of FACS measurement of ICAM-1, anti-ICAM-1 and anti-mouse488 incubated samples. A) PE channel measurement of uninfected erythrocytes gated for PE channel and EtBr. B) IT2 infected parasites incubated with and C) without ICAM-1 protein. Heat map of cell number represented by lowest (blue) to highest (red). iRBCs are gated and percentage of population within these gate parameters (fluorescence) can be seen within the black box.

This result was surprising as it indicated that the secondary antibody could possibly be binding more generically than originally anticipated. Changing the clonality from polyclonal to monoclonal did not have an effect. Attempting to identify binding specificity to ICAM-1 using FACS is not a common practise and does require optimization. However, it also needs to be pointed out that this type of measurement assumes a stable and strong bond between PfEMP1 and the antibody-labelled ICAM-1 and no cross-reactivity to the secondary antibody. Since this was not the case, it was not recommended to continue this assay for the purposes of strain characterization.

Selection with His-ICAM-1 resulted in selection against His rather than ICAM-1 while for the platform setup Fc chimeric ICAM-1 was used to ensure correct orientation of ICAM-1 and exposure.

Attempting to select with primary cells constitutively expressing ICAM-1 on their surface to avoid using a recombinant protein for selection did not result in the desired selection. The yield of selected parasites was increased in the case of selection against CHO cells expressing ICAM-1, however static assays performed showed no differences in number of cells adhering to CSA, BSA and ICAM-1. Furthermore, the goal of the selection protocol was to increase affinity to ICAM-1 in its recombinant form and not in its native form as expressed by endothelial cells or CHO-ICAM-1 cells. In addition, a variety of receptors that parasites could possibly also select against are constitutively expressed on the surface of other cell types. Consequently, I opted against a selection protocol using cells in order to increase selection specificity towards ICAM-1 as found in our flow assays.

However, selection with recombinant His-ICAM-1 was also not yielding the expected results. The observed high number of adherent cells seen in the static assay could be the result of selection against the 6-Histidine tag of the recombinant protein used for selection, rather than ICAM-1. In order to circumvent these issues, I selected against an untagged recombinant ICAM-1 protein in static assays. I noticed a significant change in efficiency of the protocol, however more than seven rounds were needed to get a satisfactory yield after performing a panning protocol.

3.1.1.4 Knob characterization

Furthermore, I wanted to determine the knob density of the $IT2_{ICAM-1}$ strain selection, to further investigate the adhesive properties and shed light to the puzzling low affinity and diverse *var* gene expression observed. This was achieved using scanning electron microscopy (SEM).

From these images, we were able to qualitatively determine knob morphology and distribution on preserved HbAA erythrocytes infected with $IT2_{ICAM-1}$ trophozoite stage parasites (Figure 3.5). Erythrocyte diameter determined by these images was 5 µm (n=16), in accordance with literature values. Knob distribution was calculated at 46 knobs/µm^2. Though knob morphology and parasite growth were within the norm [87, 119], issues regarding selectivity and affinity to ICAM-1 still remained.

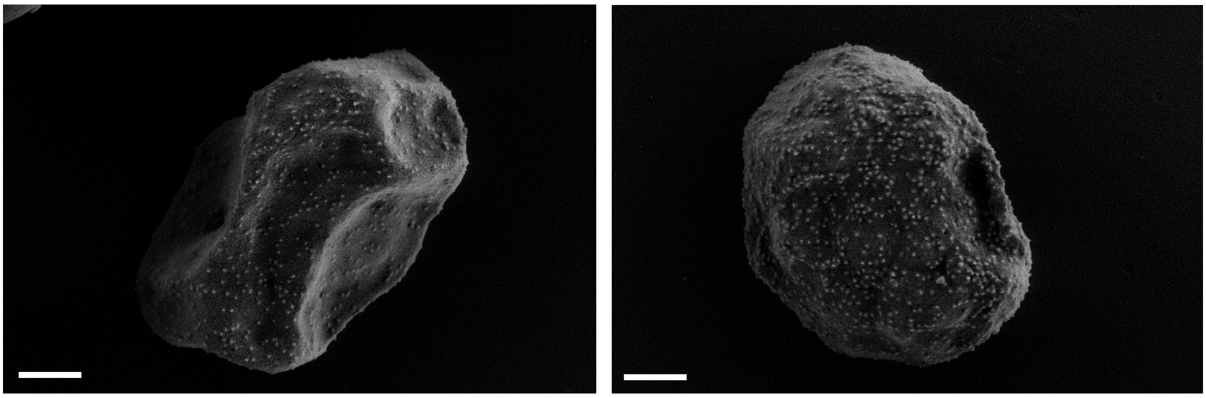

Figure 3. 5: Scanning electron microscopy images of HbAA erythrocytes infected with trophozoite-stage IT2 ICAM-1 parasites. Scale bar 1 µm.

We received an $IT4_{ICAM-1}$ (Gambia) strain from the lab of Prof. Alister Craig, selected against recombinant ICAM-1 for multiple rounds. Due to differences in the panning protocol and changes in the frequency of selection prior to cryopreservation (more than ten rounds), this strain showed a much higher affinity to ICAM-1 and was used to further investigate and characterize adhesion dynamics of HbAA and HbAS infected erythrocytes.

The analysis of the *var* gene expression profile as performed by the group of Prof. Craig ensured an expression of up to 90% of a single *var* gene, known to bind ICAM-

1 (data not provided). Prior to use, this strain was also selected against untagged ICAM-1, for at least five panning rounds before utilization in a flow experiment.

3.1.2 Optimization of flow chamber and ICAM-1 presentation

Parallel to optimizing affinity to ICAM-1 for the IT4 strain in static assays, I also performed experiments to test adhesion of HbAA and HbAS *Pf*- infected erythrocytes in flow chambers with induced shear stresses (Figure 3.6).

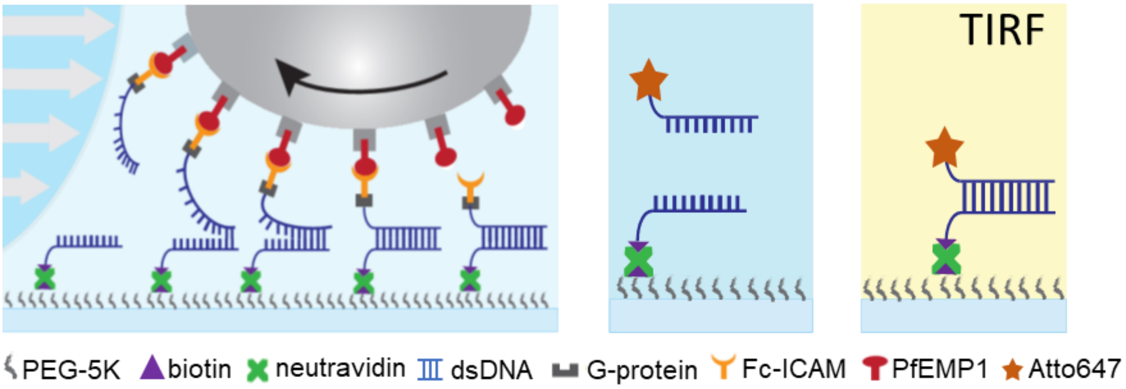

Figure 3. 6: Experimental setup of flow chamber experiment. Mature stage *Pf*-parasitized erythrocytes (grey) come in contact with ICAM-1 attached to a double-stranded oligonucleotide sensor and leave single strands of DNA at the sites of interaction. These are then visualized using a fluorescently-tagged complimentary probe using a TIRF microscope. White arrows indicate the direction of flow, while the black arrow represents the rolling motion of the infected erythrocyte.

The setup of the platform developed by Li *et al* in 2017 [177], was not optimized to observe *Pf*-infected erythrocytes in flow and adjustments had to be performed. Differences in the functionalization between the steps was a concerning result, indicating disproportional spread, signal clumping and formation of bubbles and gaps that impact the readout. To determine the specificity of the fluorescent signal, I performed multiple control experiments parallel to each flow experiment.

A thin glass substrate is the most appropriate material to use in order to obtain microscopic images of high quality. Polyethylene glycol (PEG-MW:5000) functionalized with a substrate tethering unit were used to passivate the silica-NH_2 activated glass substrate. From a variety of options, a succinimidyl-valerate (SV) moiety was chosen, as it is a stable and reliable reagent, that is water-soluble and interacts with free amine groups (NH_2) in pH = 7, forming an ester that crosslinks the PEG- macromolecule to the glass substrate. Mixing biotin-functionalized PEG with a matrix PEG-SV (1:100), to achieve a density of approximately 400 biotin spots/μm^2. As a control for the spread of the PEG molecules, streptavidin-Alexa647 was added and then imaged with a TIRF microscope and the effects of concentration and changes in incubation conditions (time, temperature, solvent) can be clearly seen (Figure 3.7).

After optimizing this step, plastic flow chambers were glued to the PEG-ylated surface using PDMS, a polymer glue that is stable and non-reactive to biological samples, and which can withstand high pressures and is non-toxic for cells. Other glues proved to be ineffective and would dissolve within 24 h or during flow experiments resulting in drying of the sample.

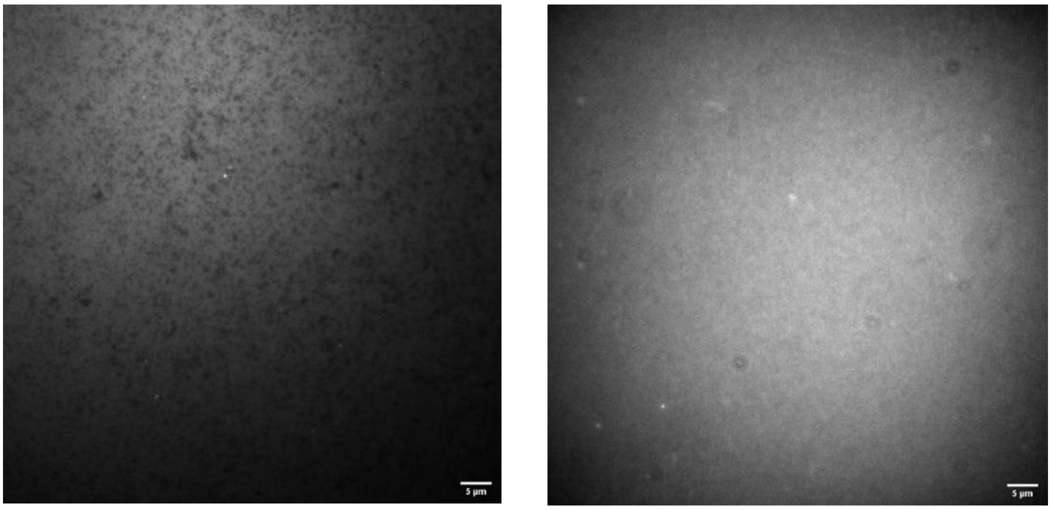

Figure 3. 7: Difference in biotin spread, as detected by the signal of fluorescently labelled streptavidin. Optimization of biotin concentration as well as conditions of incubation. Scale bar is 5 µm.

The next step of the protocol implemented the use of molecular force sensors, hereon referred to as TGTs (Tension Gauther Tethers). These sensors are short double-stranded DNA oligonucleotides, that were functionalized with a biotin molecule at the 5' end of one strand (bottom strand).

This functionalization allowed the tethering of these sensors to a PEG-biotin-neutravidin sandwich, followed by the biotin spread (Figure 3.8 A). The complementary strand (top) was functionalized with a sulfhydryl (SH)- moiety at the 3' end or a fluorescent molecule (cy3 or Atto-647). Complementary strands with the 3´end coupled to a fluorophore were incubated with biotin and neutravidin functionalized substrates to determine spread and binding efficiency (Figure 3.8 B). The possibility of multiple washing steps disrupting the uniform bed of TGT, causing them to unzip randomly was tested (Figure 3.9 A). If that were the case, the signal would not be uniform and gaps in the fluorescent signal would appear. However, the channel subjected to more than double the washing steps, was more uniform and had less gaps in the TGT-signal as seen in Figure 3.9 A.

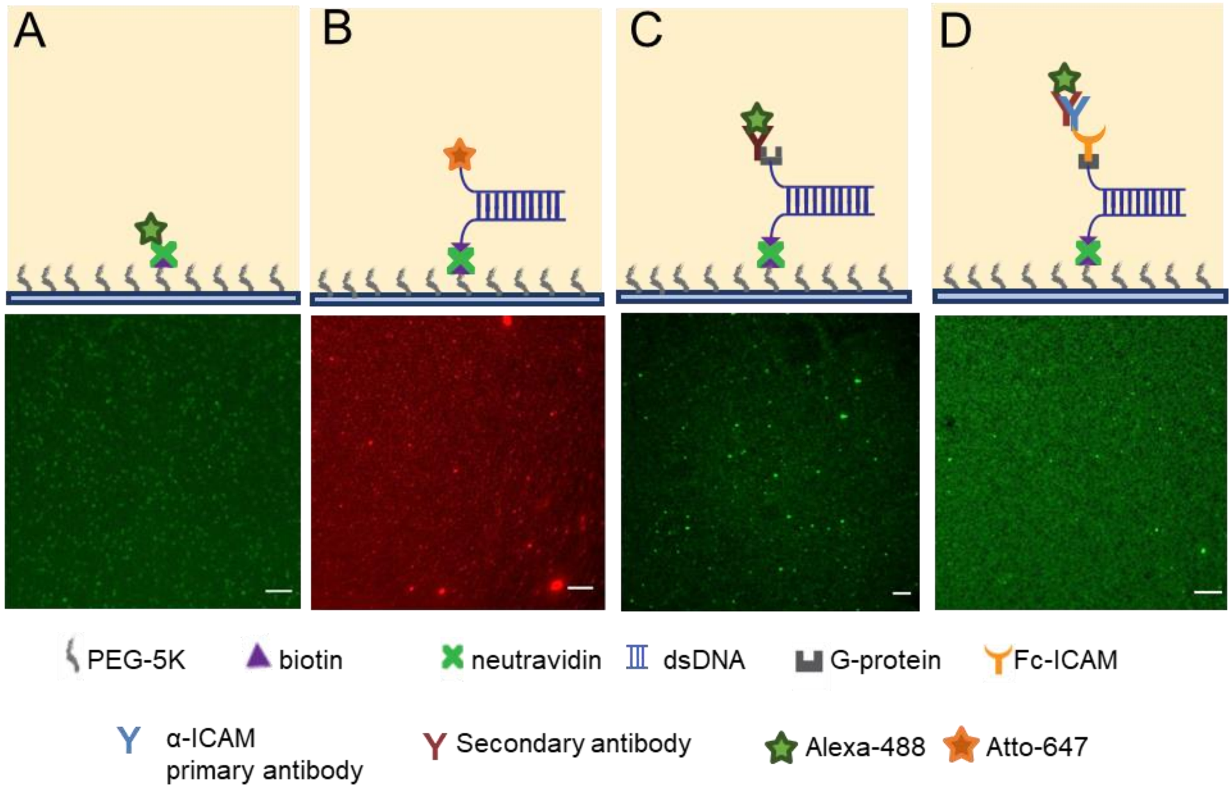

Figure 3. 8: Validation of surface functionalization. A) Biotin spread using streptavidin-488. B) TGT-Atto647 surface functionalization. C) Spread of G-protein-TGT conjugate using goat-Alexa488 antibody. D) ICAM-1 surface functionalization visualized using anti-human ICAM-1 (mouse) and anti-mouse Alexa488 (goat) antibodies. Scale bar is 5 µm.

The top strand of the sensor (topTGT), when not functionalized with a fluorophore, contained a protected SH- group that was crosslinked with G protein. Due to the unstable nature of free SH groups, the compound was produced containing a S-S-H group at the 3´end, that can be de-protected with the use of a strong reducing agent.

To this end, the use of freshly prepared TCEP was preferred due to its high yield and efficiency. The reduction of sulphur bonds resulted in a free -SH group at the 3´end of a single stranded TGT that could form a stable thiol-ester with a maleimide of a short linker molecule (SMCC). This covalent bond is stable and forms under physiological pH (7 to 7.5) and allows for the covalent binding of free amine groups. Recombinant G-protein contains multiple free amine groups and one of them was therefore randomly crosslinked to the top strand through the NHS-moiety of the SMMC linker.

The newly formed topTGT-SMCC-G-protein conjugate (Table 3.1) was then incubated at 65 °C in excess (1.2:1) with a biotin-bottomTGT, in order to form a double stranded (ds)-DNA sensor crosslinked to G-protein. G protein binds with high affinity to human and mouse antibodies [190] and contains four known binding sites for Fc fragments and therefore even if one site is blocked by a crosslinked topTGT, two more possible binding sites remain available [191]. While there were significant losses in terms of concentration during crosslinking and the purification step of the product, I was still able to produce this compound in a satisfactory amount that was subsequently used in the setup of the flow chamber.

This conjugate of G-protein and DNA-oligonucleotide is then able to bind Fc-containing molecule and ensure its correct orientation and positioning away from the glass substrate. The efficiency of this surface functionalization and accessibility of crosslinked G-protein was probed with the use of a fluorescent antibody, naturally containing an Fc region (Figure 3.8 C). The signal is strong and evenly distributed.

Recombinant chimeric Fc-ICAM was then added as a final step of surface functionalization. Ensuring excess amount of recombinant ICAM-1 was crucial to the process. Fc-ICAM-1 is also attached with high efficiency to the G-protein, as evident by the signal-to-noise ratio and uniform spread of a primary mouse anti-human ICAM-1 antibody and a secondary anti-mouse Alexa488 antibody (Figure 3.8 D)

Flow chambers functionalized with ICAM-1 proved to be unstable for longer than two days even when cooled (4 °C) and therefore, the last step was only performed on the day of flow measurement experiments and always validated with anti-ICAM-1 antimouse488 control experiments in each Ibidi slide used.

Table 3.3: Concentration of DNA construct and G-protein before (1, 2) and after (3, 4) crosslinking reaction. Measured with Nanodrop (photometer).

#	**Name**	**Concentration**
1	topTGT-SMCC (DNA)	132.35 ng/µl
2	G-protein	60045 ng/µl
3	topTGT-SMCC-Gprotein (protein)	15 ng/l
4	topTGT-SMCC-Gprotein (DNA)	0.10 ng/µl

Aggregates of antibodies or insufficient removal of excess fluorophores could be the reason for the clusters observed in Figure 3.9 A-D. It is also possible that ICAM-Fc attaches to one G-protein multiple times, resulting in signal aggregation over these spots. Using a more moderate SMCC to G-protein ratio as well as repeating the washing steps between functionalization and detection and using a more stable fluorophore dye (Atto647) instead of cy3, were effective solutions. As can be seen in Figure 3.8 C the distribution of G-protein, as visualized by anti-human IgG-Alexa488, is uniform.

In order to exclude false positive signals caused by unspecific interactions between the sensor and the erythrocytes, I performed flow experiments in chambers either lacking ICAM-1 or without the presence of the parasite. The sensor remains intact in flow in presence or absence of erythrocytes (Figure 3.9 A-D). Uninfected erythrocytes do not seem to interact with the ICAM-1 bound sensors (Figure 3.8 C) and infected erythrocytes do not disrupt the sensor (Figure 3.8 B) or interact with any other component of the surface if ICAM-1 is absent (Figure 3.8 B and D). These controls were necessary in order to verify that the signal detected is specific to PfEMP1 – ICAM-1 interactions and is not caused by flow or bulk of cells.

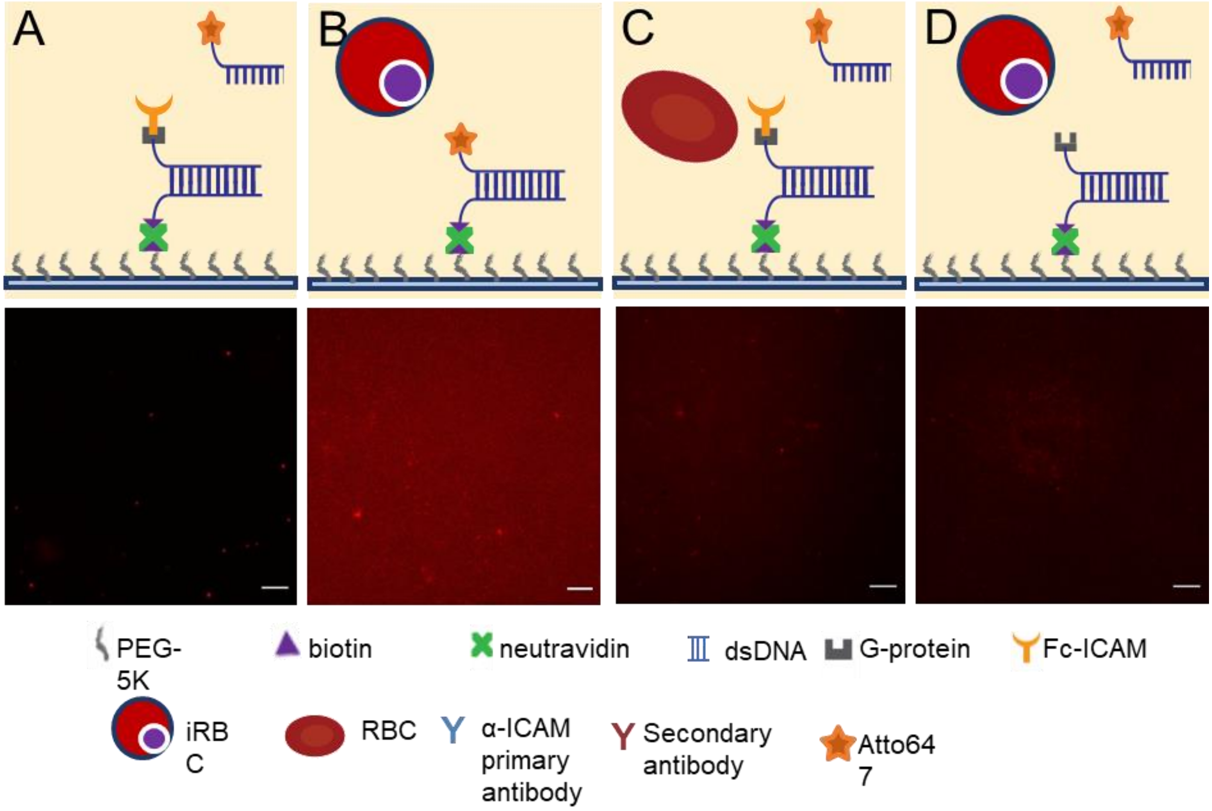

Figure 3. 9: . Negative control and signal specificity experiments. A) Flow experiment of ICAM-1 functionalized surface without cells. B) TGT-functionalized surface flow experiment with Pf-infected HbAA erythrocytes. C) Flow experiment with uninfected HbAA erythrocyte for ICAM-1 functionalized surface. D) Flow experiment of G-protein functionalized flow chamber and Pf-infected HbAA erythrocytes. A complementary strand of fluorescently tagged TGT was used to detect sensor opening. Scale bar is 5 µm.

After validating the surface and ensuring that all negative controls were established and functioning, I noticed that fluorescence quickly plateaued for cy3-coupled sensors and detection of the tracks becoming increasingly difficult with passage of time. In order to counteract this bleaching tendency, I decided to exchange the fluorophore used for the probe (cy3) to a more stable option, namely Atto647. This fluorophore has a longer lifetime and all measurements resulted in higher fluorescence intensity levels with the same exposure conditions during TIRF measurements.

Another improvement that enhanced consistency among different runs of both control and validation experiments was the addition of a diluted glutathione solution (1 %) with BSA (0.5 %) that fixated fluorophores and provided stability for the system during transport to different microscope setups used.

To further ensure that the readouts were comparable for different experimental runs, all measurements were performed consecutively on the same day and all components were stored at -20 °C prior to used, thawed only once on the day of measurement and added immediately after thawing to the flow chambers at room temperature.

3.1.3 Flow chamber experiments of trophozoite and schizont stage parasites within HbAA erythrocytes

After performing all necessary negative control experiments, I used the platform to highlight a specific interaction between ICAM-I and IT4$_{\text{ICAM-1}}$ parasitized erythrocytes.

The interaction between expressed PfEMP1 variant and Fc-ICAM, presented on the surface and attached to a TGT, would result in the unzipping of the TGT. This allowed the detection of all specific interactions using a single-strand probe attached to a fluorophore. Using a precise syringe pump and considering the measurements of the Ibidi$^{0.4}$ flow chambers, the wall shear stress (WSS) was calculated for each experiment.

A total of $2x10^6$ IT4$_{\text{ICAM-1}}$ parasitized erythrocytes were injected into the chamber and washed out at induced sheer stresses increasing gradually from 0.03 to 0.3 Pa. Cell number was optimized to ensure that single tracks were distinguishable and present.

Due to the diversity of PfEMP1 receptors expressed in the cultures used for the assay we can assume that this is the reason that we could not see any specific traces for either trophozoite or schizont stage parasites when performing these experiments with IT2$_{\text{ICAM-1}}$ cultures. Therefore, I installed a platform equipped with sensor-tethered ICAM-1 (as described in Section 2.2.5.2.1) and allowed IT4$_{\text{ICAM}}$ parasites to settle and adhere to the simulated substratum as described in Section 2.2.5.2.2.

3.1.3.1 Reflection Interference Contrast microscopy (RICM) measurements

In order to correlate cell adhesion in flow with the tracks detected, I employed the microscopy technique known as Reflection Interference Contrast Microscopy (RICM). This technique can visualize the geometry of a variety of objects, such as thin films, beads or living cells in close proximity to a planar surface [192, 193]. This allowed the observation of cell shape and contact area (or “area of close proximity”) in relation with the ICAM-1 functionalized surface, without generating interference for the track detection that followed using a different microscope and microscope setup (TIRF) [194].

Of the six available channels of each µ-slide, the first and last channel was used for validation of ICAM-1 functionalization and negative control experiments respectively. Tightly synchronised trophozoites or schizonts were added to each of the remaining channels and allowed to settle for at least 5 min at room temperature.

Each channel was then subsequently connected via plastic tubing to a high precision syringe pump (Harvard Apparatus, Holliston, USA) and a flow rate of 0.03 Pa WSS was generated injecting warm (37°C) binding buffer (BB) into the chamber.

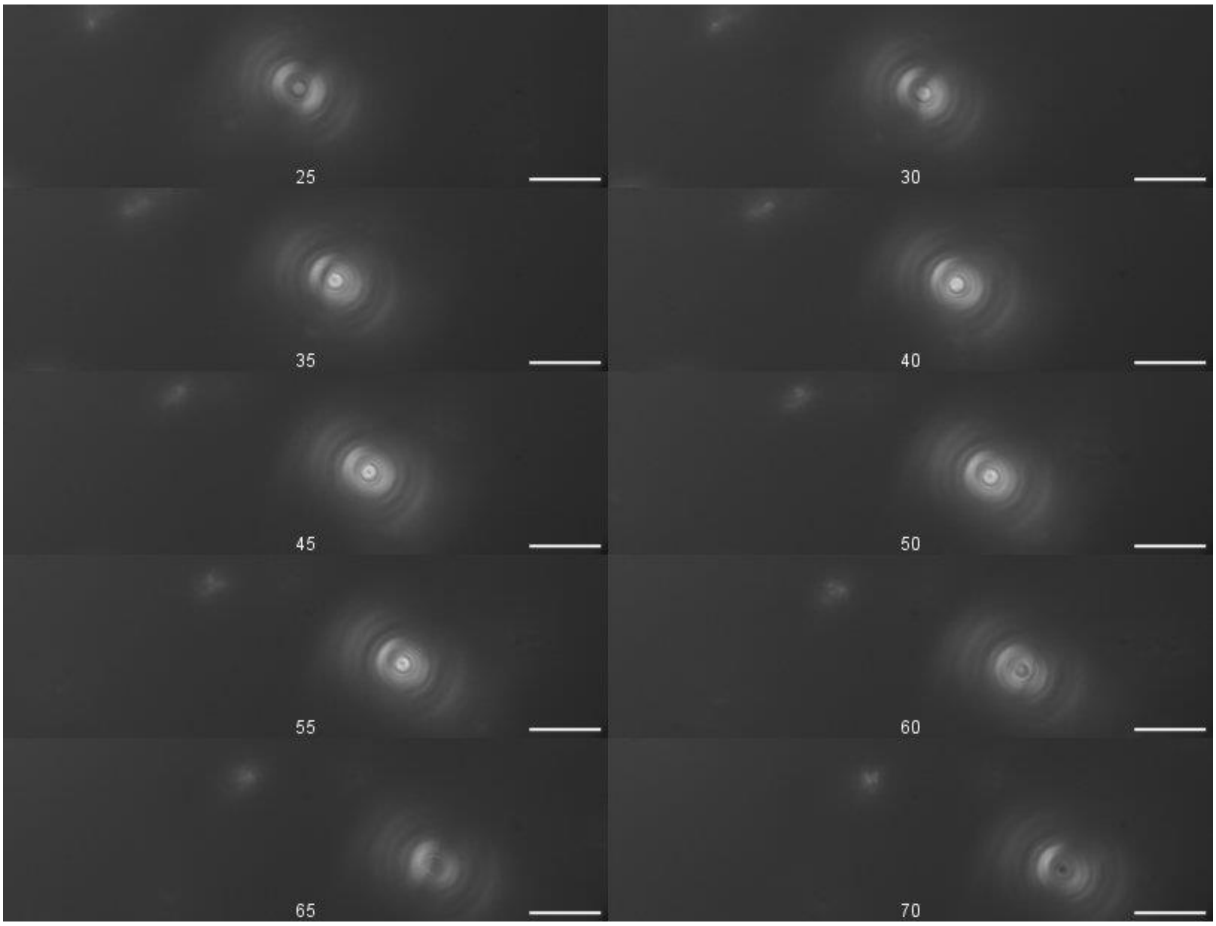

Figure 3. 10: RICM time-lapse of silicon bead incubated with anti-ICAM mouse antibody on surface functionalized with ICAM-TGT. Frame rate: 100 fps. Scale bar is 10 µm.

The objective was re-focused onto the glass surface to record 100 consecutive images with the integration time of 10 ms and multiple positions were chosen within the channel with respect to the inlet and outlet position. The generated WSS were gradually increased to reach 0.3 Pa while changing positions within the channel and recording the adherent cells detected at each rate.

I was able to observe three different types of adhesion within the channel, that mainly fell into the categories of flipping, rolling or sliding motion of the infected erythrocyte on the ICAM-1-functionalized substrate.

Flipping (Figure 3.11 and 3.12): In this type of adhesion, two subtypes could be seen. One where the cells maintained a continuous contact with the substratum, i.e. an area of low light intensity with no fluctuations or fringes while flipping over the surface. The width and length of this area may vary; however, it is consistently visible and measurable during this dynamic adhesion process across the field of view.

The second flipping motion that was detected, showed that some cells only maintain contact with one specific area of the membrane remaining attached while the elastic cell folds and then subsequently binds with a different area of the membrane. The first contact area becomes gradually smaller, as expected for a flipping dynamic adhesion. This type of flipping motion however generates a disrupted signal that cannot be singled out as the track of a single cell. This makes correlation between a single cell and its track difficult. Flipping adhesion was observed for early trophozoites and some late trophozoite stage parasites in HbAA erythrocytes.

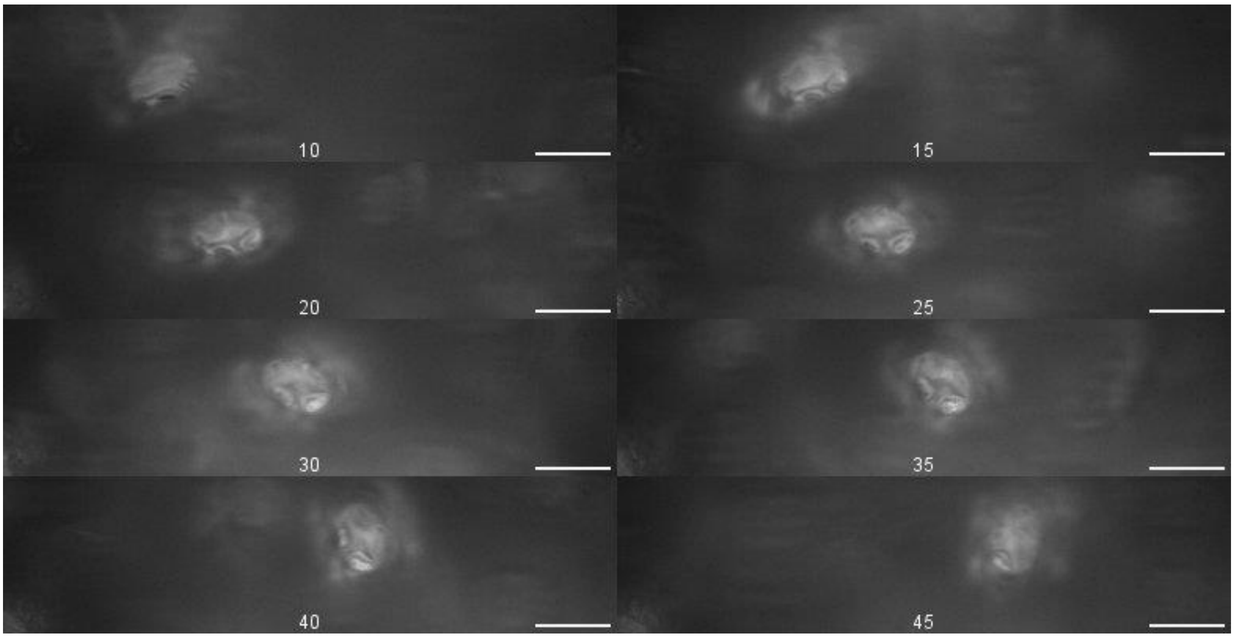

Figure 3. 11: RICM time-lapse of flipping adhesion of trophozoite stage HbAA erythrocyte. Frame rate: 100 fps. Flipping adhesion is the dynamic adhesion motion that best describes these contact areas between the surface and the cell membrane (dark grey). Scale bar is 10 µm.

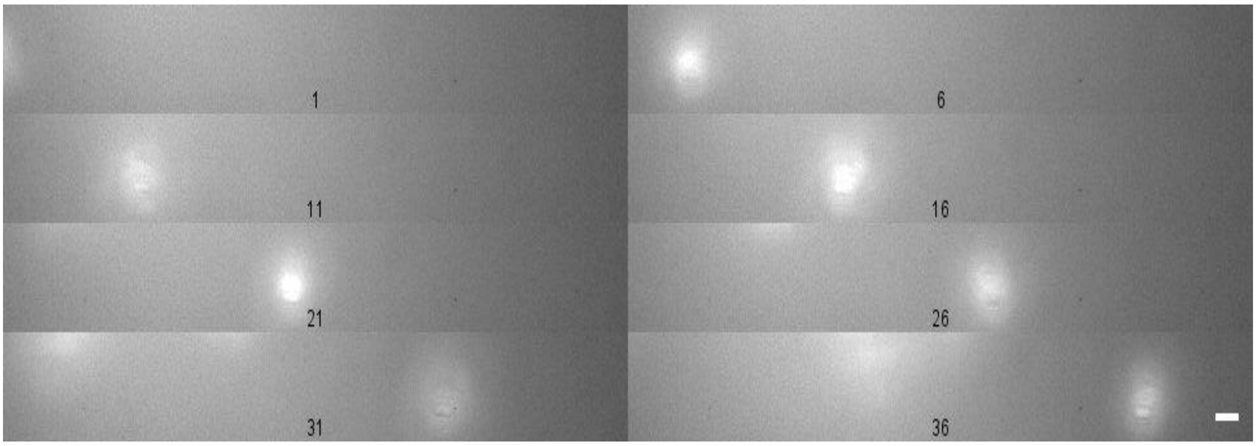

Figure 3. 12: RICM time-lapse of trophozoite-stage parasite in HbAA erythrocyte. Flipping adhesion is the dynamic adhesion motion that best describes these contact areas between the surface and the cell membrane (dark grey). Frame rate: 100 fps. Scale bar is 5 µm.

In some cases, one could observe the erythrocyte only adhering with a smaller contact area, approximately 4 µm initially (Figure 3.12) and not the full flat side of the erythrocyte (approximately 8 µm). This contact would first increase and then gradually decrease with cell movement.

Rolling (Figure 3.13). Schizont stage parasites showed a rolling adhesion, with only a very small contact area, consistent in size and remaining visible throughout its movements across the field of view.

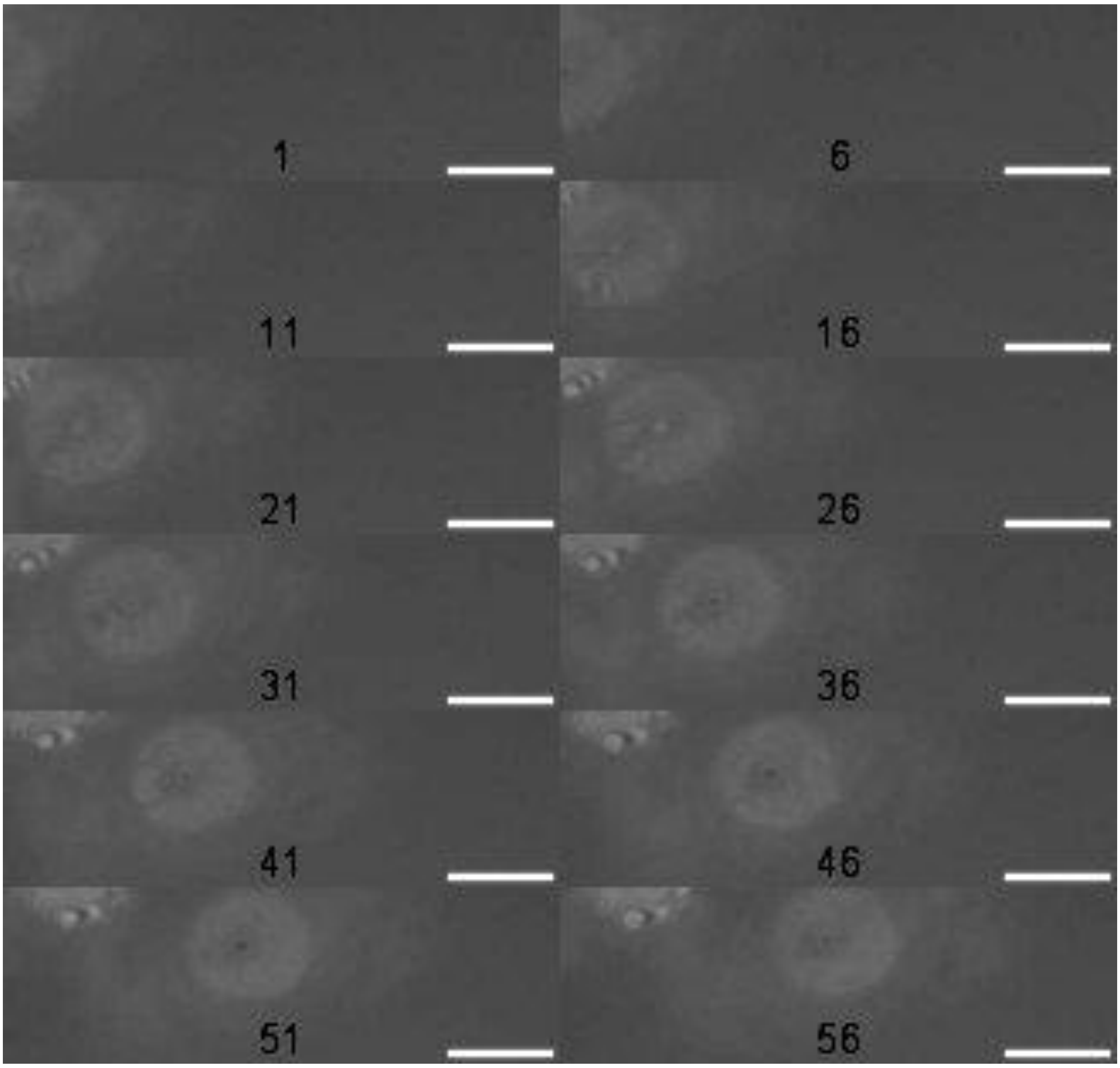

Figure 3. 13: RICM time lapse of cell adhesion of schizont stage HbAA erythrocyte. Rolling is the dynamic adhesion motion that best describes these contact areas between the surface and the cell membrane (dark grey). Frame rate: 100 fps. Scale bar is 5 µm**.**

Sliding (Figure 3.14). An unexpected motion that was also detected was a "sliding" of cells onto the surface. This motion can be best described as the cell being consistently in contact with the surface but remaining only on one side without flipping or rolling. This motion would quickly saturate the receptors interacting with ICAM-1 on this side and would not generate a footprint after this. Varying ligand density did not seem to affect this phenotype. However when the passivation protocol for the chamber was optimized to include not only BSA passivation but also the use of 0.01 % saponin solution in PBS-EDTA, this phenomenon became less frequent.

In some cases, I also observed tight adhesion, where cells could not be washed out under low pressure conditions. Therefore, after each flow experiment, the WSS was increased to 0.5 Pa and washed for at least 10 min to ensure no cells remained in the channel. Before adding fluorescent probes and mounting the slide to the TIRF microscope, it was important that no cells remained on the surface.

The pattern, highlighted by the complementary probe of unzipped DNA-strains, was observed using TIRF microscopy. Due to the instability and fast bleaching of signal that was observed when using cy3-conjugated probes, probes coupled to Atto647 fluorophore were used for all following experiments. This alteration yielded very satisfactory results in terms of signal intensity and stability of signal.

Trophozoite stage parasites (26 ± 6 hpi are more flexible and have been shown to flip on an HDMEC substratum while schizonts (36 ± 6 hpi) are more rigid and round and have been shown to roll on the substratum in flow [102].

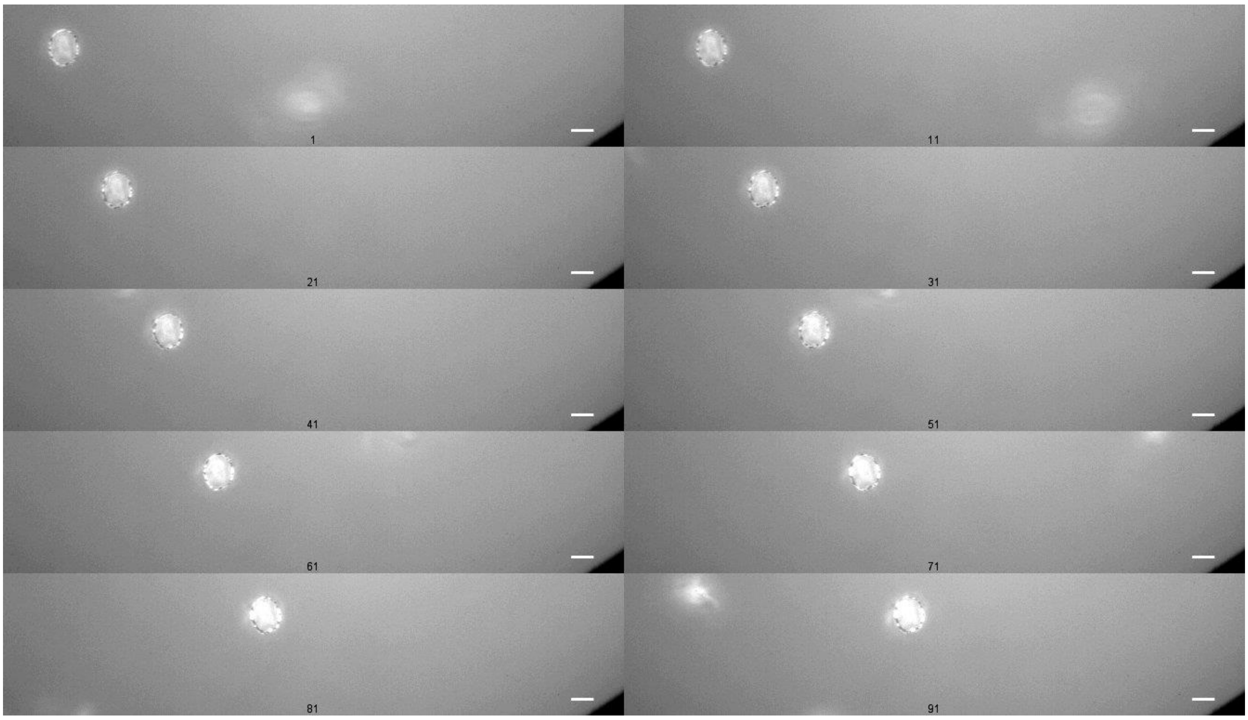

Figure 3. 14: RICM time-lapse of trophozoite-stage HbAA erythrocyte. Sliding is the dynamic adhesion motion that best describes these contact areas between the surface and the cell membrane (dark grey). Frame rate: 100 fps. Scale bar is 5 µm**.**

This setup was successful in providing single tracks of trophozoite and schizont stage parasitized erythrocytes in flow but visualizing the contact areas in a separate step (Figure 3.15). When observing the entire field of view and comparing between the track numbers and track width, it is already evident that there are large differences between trophozoite and schizont-stage parasite adhesion.

Schizont tracks are much more frequent within this field of view, closer together and quite thin. There are also areas of intense signal of larger width that appear almost circular at the start or end of tracks. These areas might be the result of a tighter adhesion, for a longer period of time, allowing PfEMP1 receptors in close proximity to the initial binding regions to also interact with the substrate and unzip the sensors close by. This might result in sequestration of the cell and, if found at the beginning of the track, might continue its movement due to increasing sheer rates exerted experimentally.

Trophozoite tracks are less in numbers in this field of view and much thicker. Denser and more intense signal is seen within each track, which was not predicted by simulations for the same stage [102]. Fewer numbers of singled out trophozoite tracks might also be due to the nature of the platform, where tracks are not seen in real time. Additionally, due to their width, there is overlap between the tracks.

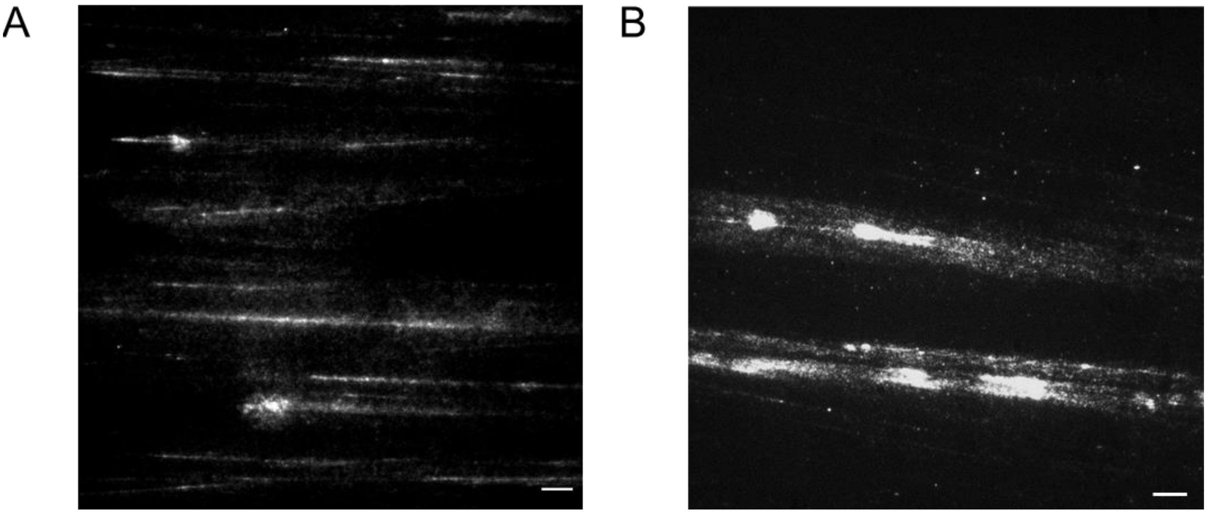

Figure 3. 15: Total reflection interference microscopy (TIRF) images of interaction sites between A) schizont stage and B) trophozoite stage parasites within HbAA erythrocytes and Fc-ICAM-1. Each interaction results in a single oligonucleotide exposure that is conjugated to a complimentary probe attached to Atto647 and highlighted as white signal. Scale bar is 5 µm.

Therefore, I only considered tracks of trophozoites for the statistical analysis and quantification that could be singled out and did not exceed the width of a single HbAA erythrocyte.

3.1.3.2 Analysis of HbAA erythrocyte tracks and quantification

Dr. Pintu Patra provided a script in order to measure track width, length, signal intensity as well as the size of smaller and larger areas of dense signal, termed patches of singled out tracks taken from a large scale TIRF image.

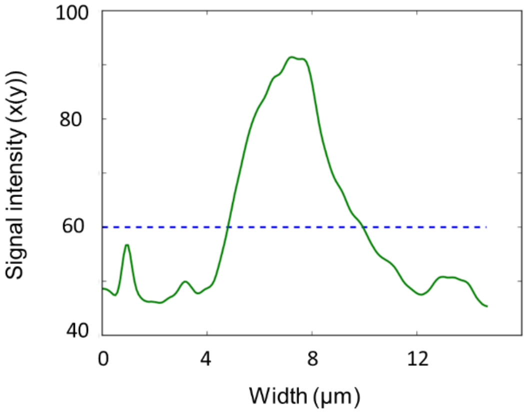

Figure 3. 16: Fluorescence intensity in y (average x values). Cut-off value for background seen as blue line and track boarders set as the green line over the cut-off value.

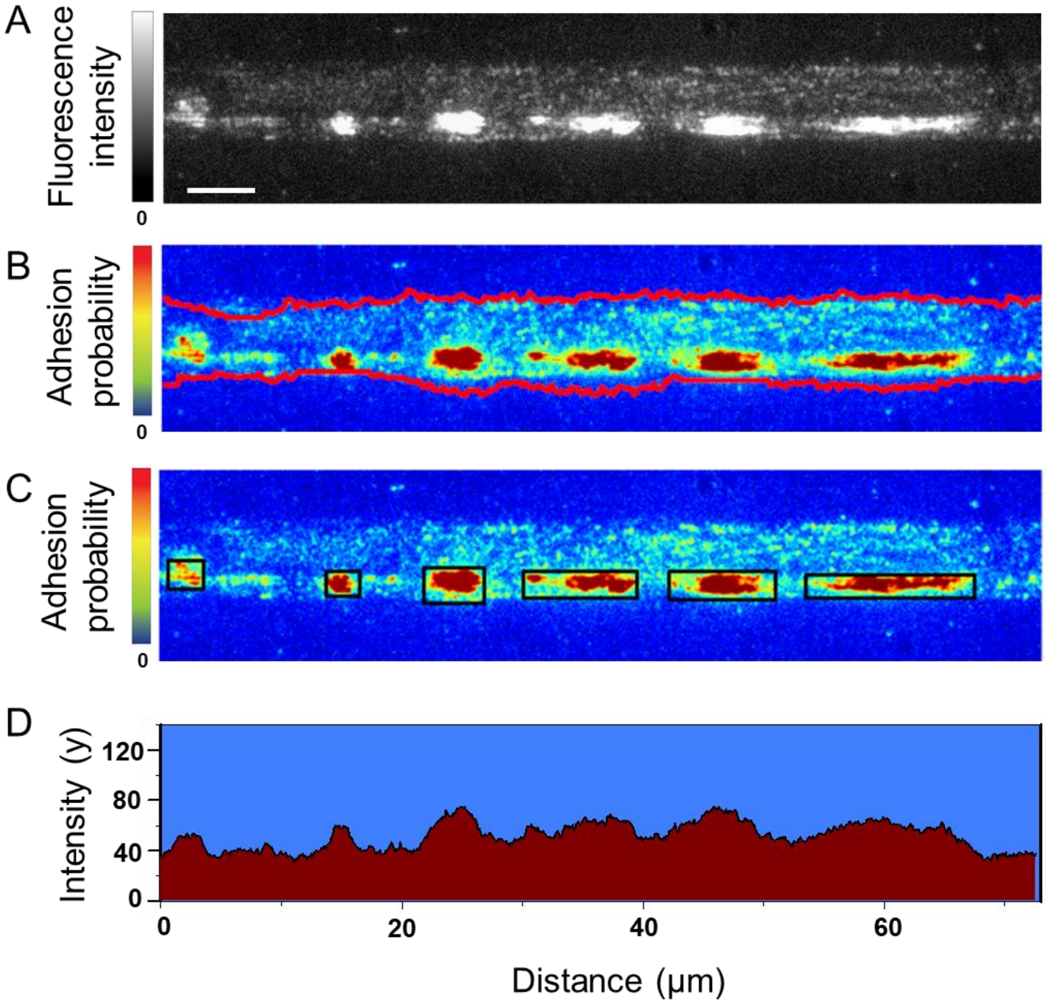

Figure 3. 17: TIRF single track and analysis of trophozoite-stage parasite in HbAA erythrocyte. A) TIRF image obtained with orbital TIRF. Background is set to black and signal to grey to white gradient of intensity and density. B) Analysis of signal intensity from track shown in A) using script detailed in Section 2.2. Heat map of intensity from blue (0) to red (100) along the track. C) Isolated high intensity areas (patches) within track boarders indicated with a black box. D) Average intensity of y along x axis for track seen in A. Scale bar is 5 µm.

For each singled-out track, the noise-to-signal ratio was optimized (as described in Section 2.2.9.1), the track was aligned using ImageJ as needed (Figure 3.17 A) and the image was analysed using the provided script, analysing fluorescence intensity along the track for x and y axis and defining track boarders.

The cut-off value of signal-to-background was set for each individual track and was used to define its upper and lower limits of the track (Figures 3.17 B, 3.18 A and C). In order to visualize these results more effectively and optimize the process, the code produces a heat map of intensity with blue (background) to yellow to red (high intensity) signal readout. The limits of the track-to-background are shown as a red line.

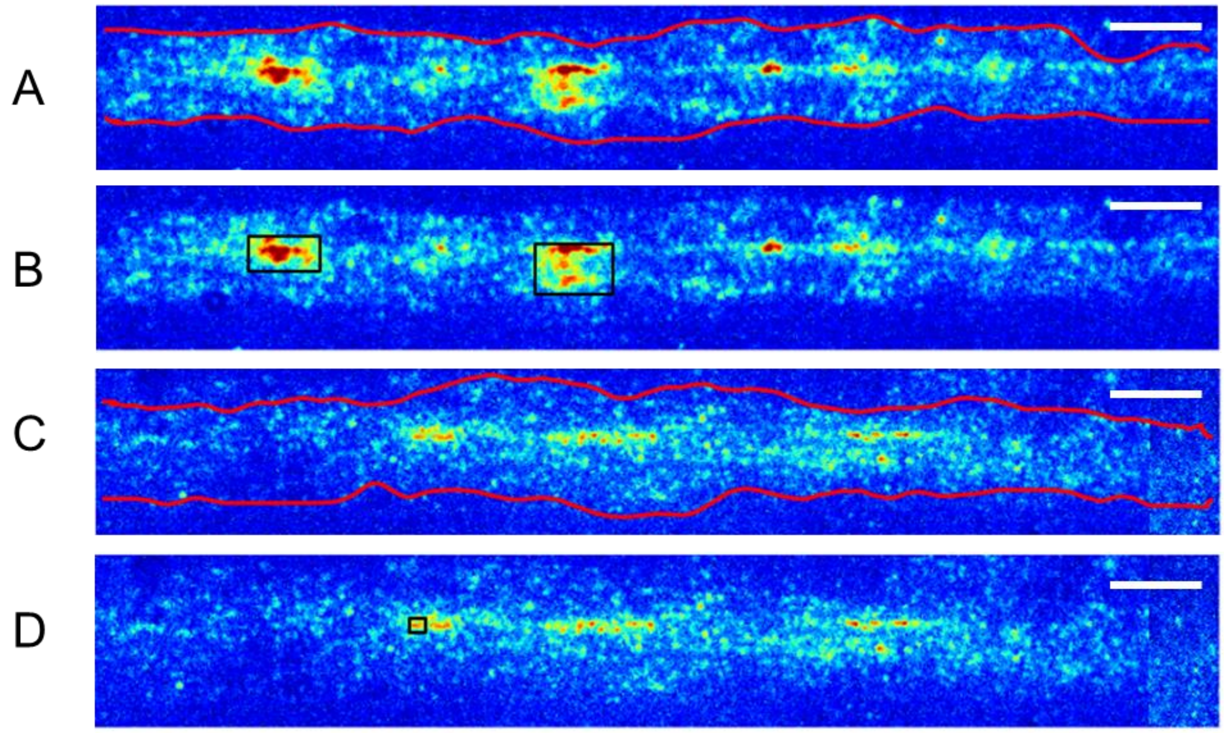

Figure 3. 18: TIRF image analysis of trophozoite-stage parasite in HbAA erythrocyte. Analysis of signal intensity using script detailed in Section 2.2, heat map of intensity from blue (0) to red (100) along the track. A) and C)Track width definition (red lines) based on signal intensity (green to red gradient) B) and D) isolated high intensity areas (patches) within track boarders indicated with a black box.

The script also provided the average intensity for all points on the x axis and was plotted as function of the y axis (Figure 3.17 D). This allows to visualize the path of the cell from a different perspective than the one seen in the analysis above. These data highlighted the differences between the stages even more, as for trophozoite stage parasite tracks there are clear peaks and valleys with varying intensities while schizont-stage parasites seem to be more uniform, with only one clear peak emerging.

Using the data gathered by the analysis described above I was able to determine that the mean width of erythrocytes infected with early trophozoite-stage parasites was 5,9 µm (n = 68). The average width of erythrocytes infected with late trophozoites was determined to be 3 µm (n = 21), while the average width of early schizonts was 2,6 µm (n=78).

From the average track width recorded it can be concluded that while the size of the parasitized cells increases during maturation, the tracks observed for each stage show the opposite trend. This is in good agreement with the RICM measurements and previously postulated hypothesis that the major components affecting contact area are size and morphology of the cell [102, 150].

A pattern of uneven distribution of signal along the tracks of early trophozoites was also detected during analysis. These larger areas of high signal intensity and density (red) were uneven in size, both within the same track as well as compared to different footprints of HbAA trophozoites (Figure 3.17 C, 3.18 B and D). The average size of these larger areas, from now on referred to as patches, was measured at 14,6 µm^2 (n = 24). I noted that the size of the patches differed and seems to follow a normal distribution (Figure 3.19 B):

On the other hand, the distance between the centre of these patches including areas of low signal density seemed to be similar and follow a specific pattern (Figure 3.19).

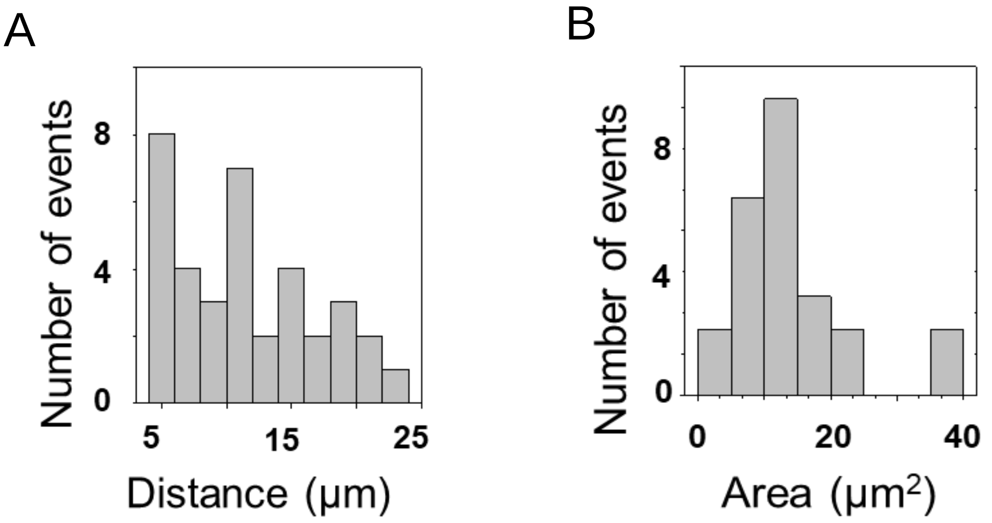

Figure 3. 19: A) Histogram of distance measured between the centre of patches within all tracks of HbAA trophozoites. B) Histogram of the total area of each patch within HbAA trophozoite tracks.

To that end, Dr. Patra provided a script to extract the average change in fluorescence intensity (ACF) and calculate the distance a round object would travel from the centre of the first patch to the next for each track. This resulted in a graph such as the one seen in Figure 3.20A and from these data, as described in Section 2.2.1.9. Dr. Patra could produce a 3D projection of the track and the most probable areas of adhesion on the erythrocyte membrane (Figure 3.20 B). Remaining in the same colour palette for intensity (blue for background, green to yellow to red for signal intensity), the model shows the two areas of the membrane most likely to adhere to the substrate in flow and provide a logical explanation for adhesion patch creation with at the red regions. We adapted the most probable configuration, that also correlated with RICM measurements and flipping dynamic adhesion onto the surface.

The average distance of patches measured at 13,8 µm (n = 7, Figure 3.21), when only taking into account the rolling distance between the two first patches of each recorded track. When assuming a normal distribution of values for these distances, we would expect a peak at this value, but also see a peak at smaller distances of approximately 5 µm (Figure 3.19 A). Assuming a size of 8 µm in diameter for an HbAA erythrocyte, this distance is approximately half the circumference of a trophozoite-stage infected cell (Figure 3.20 B).

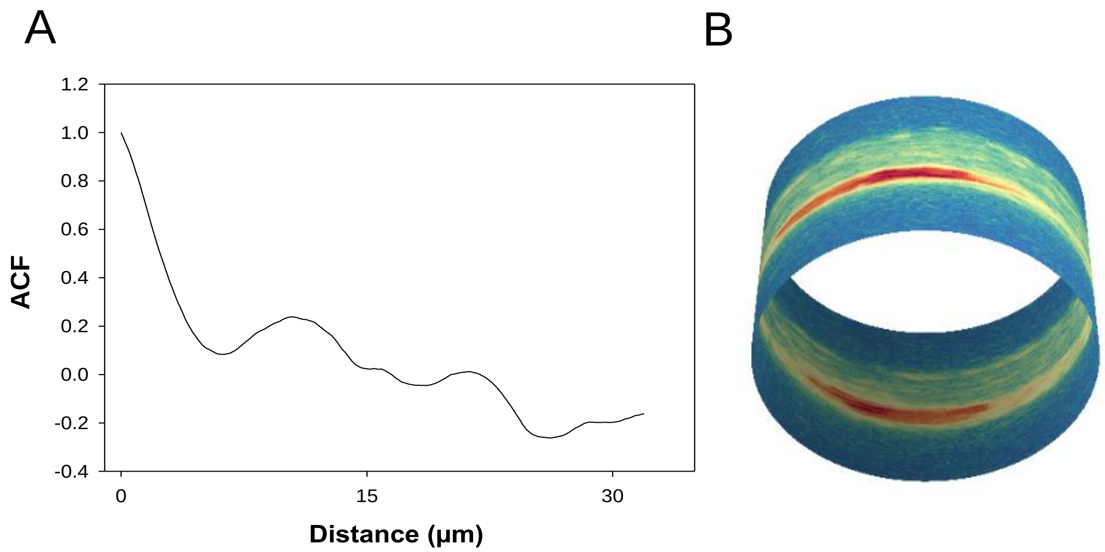

Figure 3. 20: Average change in fluorescence intensity (ACF) fitted to a round object along the x axis of cell movement A) Average change in fluorescence intensity for each x point along the y axis of the track. Each peak correlates to the centre of a detected patch and the black line represents circular distance travelled from the centre of a patch to the next. B) 3D projection of track to fit patch pattern with heat map, ranging from blue (background, no signal) to red (high intensity and density signal).

Based on our analysis and RICM video recordings of flipping adhesion for trophozoite stage parasites, I hypothesize that there are two areas that are found on opposite ends of the cell, with highest probability of adhesion based on the patch placement (Figure 3.20 B).

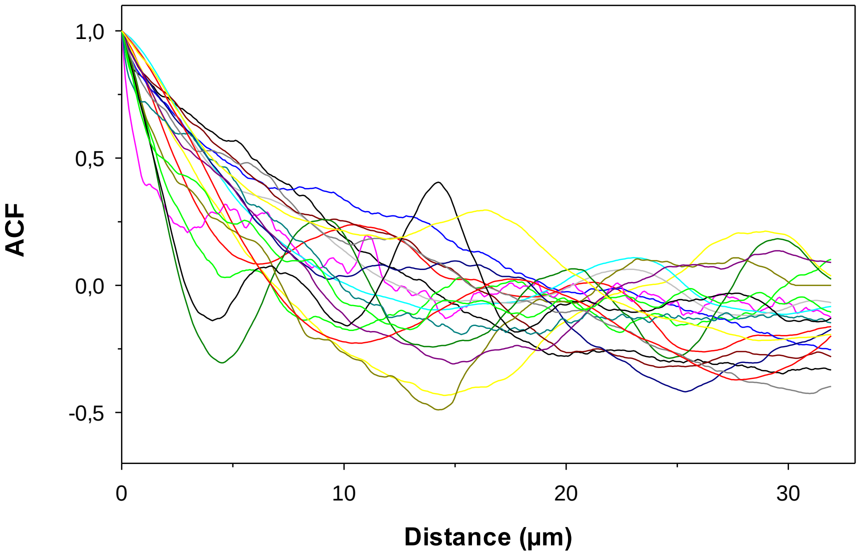

Figure 3. 21: Cumulative graph of average change in fluorescence intensity (ACF) along the x axis of cell movement for all trophozoite tracks. Each peak correlates to the centre of a patch. For this analysis, tracks for 7 different HbAA cells with trophozoite-stage parasites are included, where large patches were identified.

If the flipping adhesion is continuous, the lower signal density correlates with less adhesion probability, likely due to the biconcave shape of the cell and consequently a deterred interaction between cell membrane receptors and ICAM-1 due to distance. It should also be noted that these patches remained in their position within the track and do not seem to cross over at any point as seen in Figure 3.17 C and Figure 3.18 B.

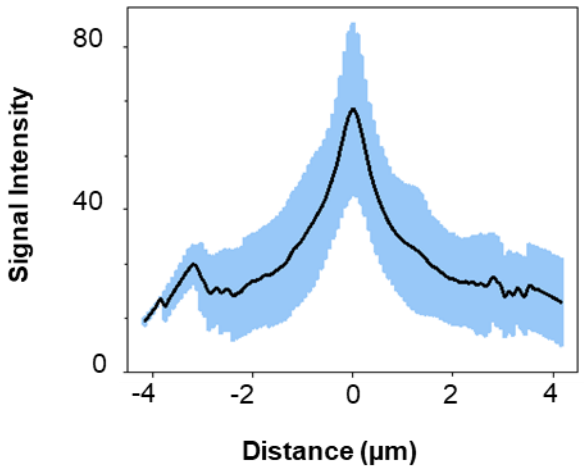

Figure 3. 22: Average width schizont-stage parasites in HbAA erythrocyte. Signal instensity (x average on y axis) identifies the boarders of the track and the width of this area is plotted to define width of schizont track. Average of signal intensity seen as a black line and standard deviation within all schizont tracks (n=78) is seen in blue.

These large patches are absent with further maturation of the parasite, where the track becomes thinner and more uniform (Figure 3.22).

Using the same script, I also analysed all schizont-stage parasite tracks for HbAA erythrocytes and used the same colours codes to analyse track width and fluorescent intensity on x and y axis (Figure 3.23). Smaller spots were still detected but did not meet patch size criteria (Figures 3.24 B and D).

When modelling the adhesion track of an early schizont, it is apparent that the adhesion probability is equal around the circumference of the cell (Figure 3.23 D). This is also in good agreement with the RICM measurements showing primarily rolling adhesion for early schizont-stage parasites.

As mentioned before, the width of schizont stage parasite tracks is significantly reduced and does not have larger patches of adhesion repeating within the borders of the footprint. Isolated tracks were also in general shorter than those measured for trophozoites. Due to the limitation of this platform in providing only secondary detection and not real-time adhesion dynamics, I did not assume track continuation if the signal was interrupted.

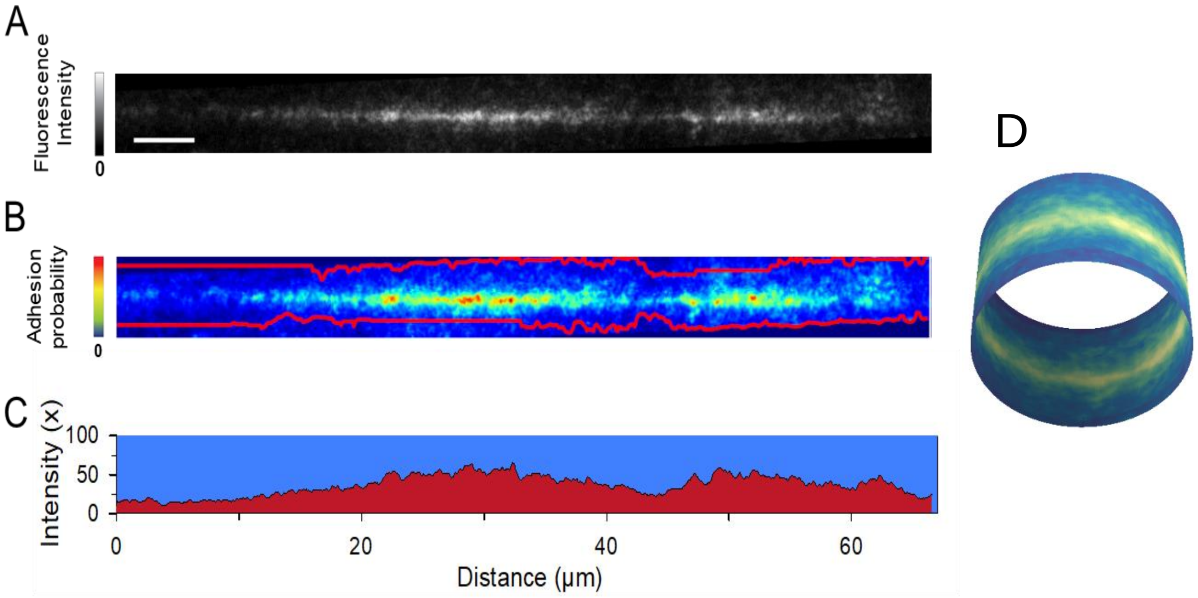

Figure 3. 23: TIRF single track and analysis for early schizont in HbAA erythrocyte. A) TIRF image obtained with orbital TIRF. Background is set to black and signal to grey to white gradient of intensity and density. B) Analysis of signal intensity using script detailed in Section 2.2, heat map of intensity from blue (0) to red (100) along the track. C) Isolated high intensity areas (patches) within track boarders indicated with a black box. D) 3D projection of track onto a cylinder with blue background and green-to yellow signal gradient depending on intensity. Scale bar is 5 µm.

The analysis of parasitized HbAA cell footprints also provided data on isolated smaller high intensity (red) spots in both trophozoite and schizont stage tracks and measured at comparable sizes with approximately 1,6 µm^2. The average length of trophozoite was measured at 0,7 µm and width at 0,6 µm. For schizonts, the average length was slightly increased and measured at 0,8 µm, while the width of the spots decreased to an average of 0,5 µm. These spots are arguably the smallest contact areas detected between the HbAA erythrocyte and the ICAM-1 functionalized surface and are similar for HbAA trophozoites and schizonts.

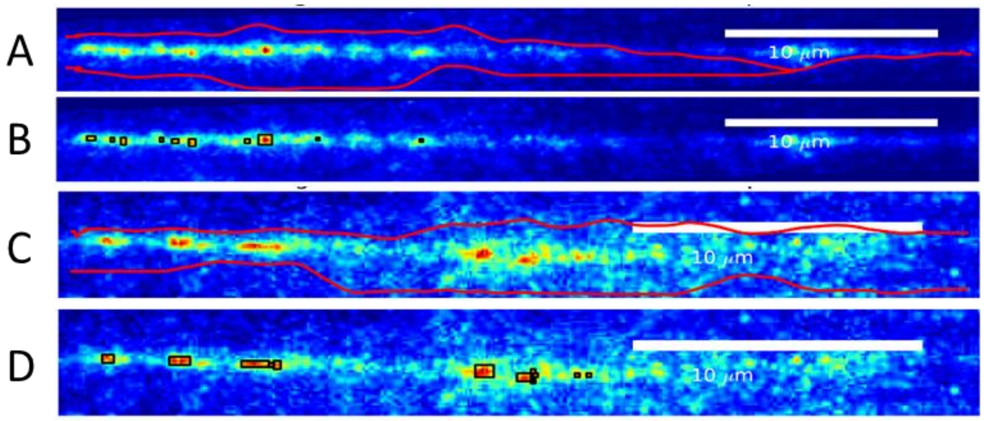

Figure 3. 24: Single track analysis for early schizont in HbAA erythrocyte. A) and C) Analysis of signal intensity using script detailed in Section 2.2, heat map of intensity from blue (0) to red (100) along the track. B) and D) isolated high intensity areas (patches) within track boarders indicated with a black box.

3.1.4 HbAS parasitized erythrocytes

Due to the observed differences in dynamic adhesion between AA and AS cells [102, 155] the project scope was extended to investigate the tracks of haemoglobinopathic compared to wild type parasitized erythrocytes.

To this end, I tested trophozoite and schizont stage parasites in HbAS erythrocytes using the optimized platform described above and under the same conditions in order to determine contact patterns and dynamic adhesion. Due to the reduced infectivity rate that is expected during inoculation of HbAS cell culture with the selected parasite strain, synchronization was performed prior to inoculation and parasites were used immediately at the estimated hour post invasion reflecting maturation stage post invasion. Perfusing the same number of MACS purified cells as for HbAA cells, at the same sheer rates ensured that the tracks recorded were obtained under comparable conditions and differences and similarities were representative of each cell morphology.

Dr. Patra provided an optimized script to analyse HbAA vs HbAS tracks and provide information based on signal intensity and density across a singled-out track (Figure 3.25 A-C)). Modelling this adhesion pattern for trophozoite stage parasites resulted in the 3D projection displayed in Figure 3.25 D. As shown in this model, due to lack of periodicity for patches in these tracks, the probability of adhesion is lower than in HbAA erythrocytes and has larger gaps with low to zero probability of adhesion.

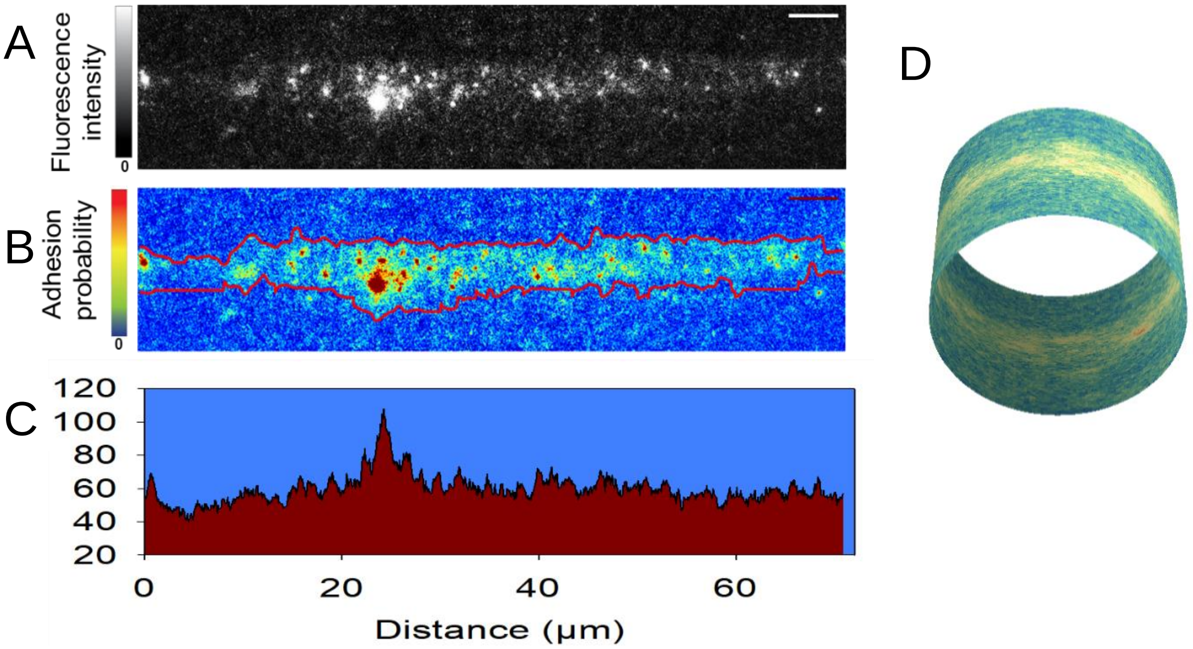

Figure 3. 25: TIRF single track and analysis for early schizont in HbAS erythrocyte. A TIRF image obtained with orbital TIRF. Background is set to black and signal to grey to white gradient of intensity and density. B) Analysis of signal intensity using script detailed in Section 2.2, heat map of intensity from blue (0) to red (100) along the track. C) Average intensity of y along x axis for track seen in A. D) 3D projection of track onto a cylinder with blue background and green-to yellow signal gradient depending on intensity. Scale bar is 5 µm.

The tracks recorded for early trophozoite stage parasites in HbAS erythrocytes were less continuous, with shorter length of tracks recorded. The average width of these was measured at 6,9 µm (n = 39). This size is more comparable to track width of late trophozoite stage in HbAA erythrocytes, despite the parasites used at 26 hpi (early trophozoite stage).

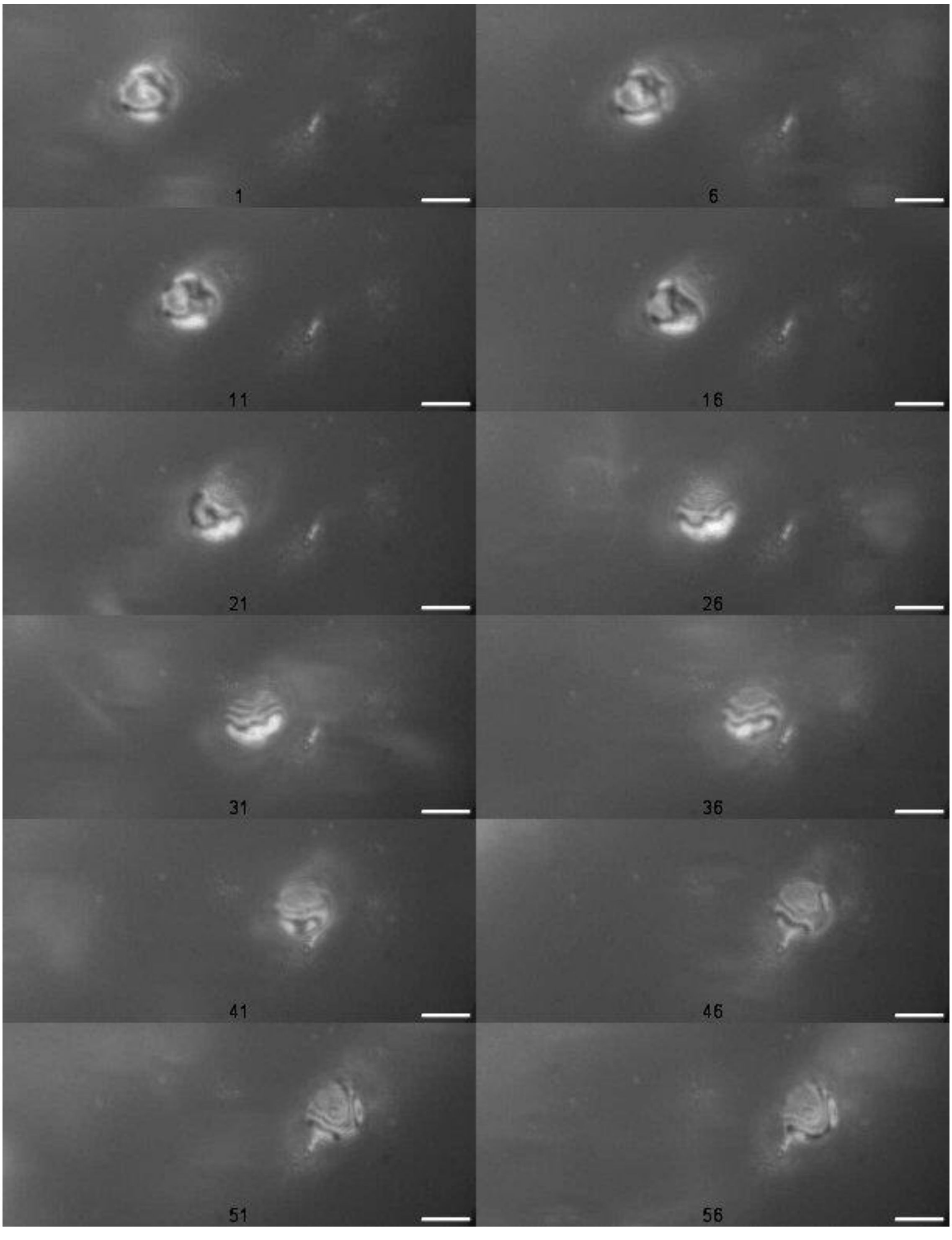

Figure 3. 26: RICM time-lapse of trophozoite stage parasite within HbAS erythrocyte. Flipping adhesion is the dynamic adhesion motion that best describes these contact areas between the surface and the cell membrane (dark grey). Frame rate: 100 fps. Scale bar is 5 µm.

RICM recordings (Figure 3.26) correlate such an adhesion track to a cell flipping onto the substratum with probability of adhesion irregularly distributed across the membrane. The cell seems to attach for a short period of time and then detach in its majority (last frame in Figure 3.26, bottom right). While the recording shows a continuous proximity of the cell to the surface, the larger area of the parasitized erythrocyte does not come in contact with the surface and the contact area decreases over time.

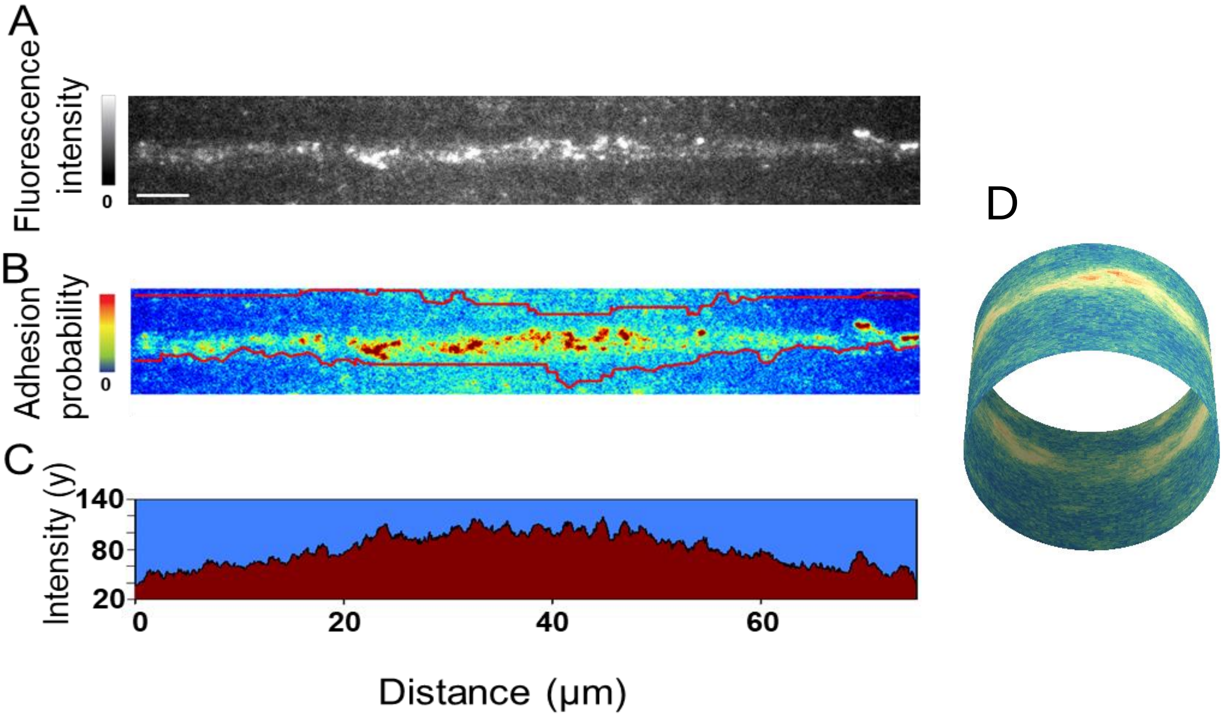

Figure 3. 27: TIRF single track and analysis for early schizont in HbAS erythrocyte. A) TIRF image obtained with orbital TIRF. Background is set to black and signal to grey to white gradient of intensity and density. B) Analysis of signal intensity using script detailed in Section 2.2, heat map of intensity from blue (0) to red (100) along the track. C) Average intensity of y along x axis for track seen in A. D) 3D projection of track onto a cylinder with blue background and green-to yellow signal gradient depending on intensity. Scale bar is 5 µm.

Early schizonts in HbAS cells, also showed a different pattern than HbAA parasitized cells. Areas with higher probability of adhesion seem to be located in the centre of the track. Smaller gaps between patches can be seen here though there is no regularity in these distances. The average track width of schizont stage parasites in HbAS erythrocytes was measured to be 3,4 µm. From these data, it is safe to assume that the trend of reduced contact area width due to parasite maturation the resulting changes in cell morphology is consistent in both HbAA and HbAS cells.

HbAS cell tracks also show more irregular patterns of patches, with patch area averaging at 8,2 µm^2 (n = 139, Figure 3.28). These are present in most recorded tracks, but do not remain in a clear trajectory as seen in HbAA cells. They seem to be irregularly crossing to each side with larger and more irregular gaps of signal (Figure 3.27).

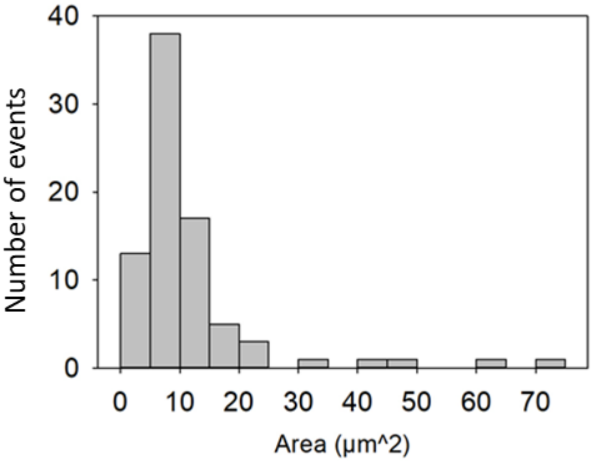

Figure 3. 28: Histogram of patch size (area in µm^2) for all HbAS erythrocytes.

When measuring ACF and distance between patches, there is no periodicity or regular pattern, indicating a much more irregular attachment to the surface for HbAS erythrocytes.

3.2 Aim 2: Quantification of *P. falciparum* PfEMP1 binding strength to its receptor

In order to determine the adhesion strength between VAR2CSA and CSA, I opted for the binding of PfEMP1 VAR2CSA (DBL1-ID2) to the cantilever and CSA to the substrate and performed a series of AFM based force spectroscopy experiments as described in Section 2.2.7. This method can help elucidate single molecule unfolding events that are not detectable in bulk methods. It can be performed in real-time, only requires small amounts of protein (typically only in the µg range) and can be performed in non-denaturing conditions and in aqueous solutions.

3.2.1 Physiosorbed CSA/BSA on plastic

CSA is able to physically resorb on clean tissue culture plastic (TCP), thus forming an arbitrary deposition on the surface. I used CSA at 1 mg/ml concentration to coat TCP, an experimentally determined concentration used for static adhesion assays of infected erythrocytes. In order to determine an optimal concentration for my purposes, I also tested 0,1 mg/ml CSA-coated substrates as well as albumin as a negative control. A non-specific interaction is defined as forces that occur mainly due to steric retention of the proteins on the cantilever rather than bond formation. However, high adhesion frequency and forces that were similar to the interactions were seen on the positive control substrates functionalized with CSA (Figure 3.29).

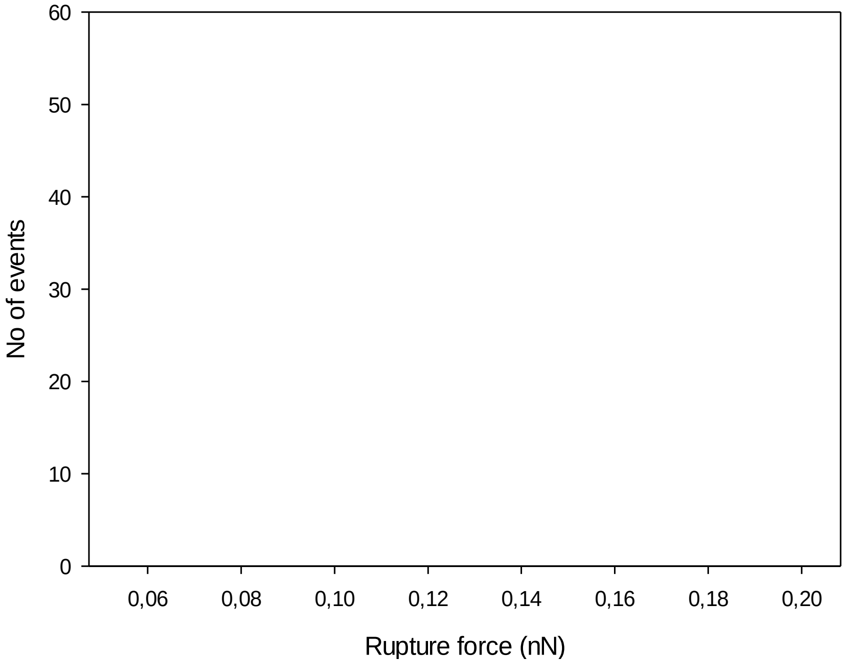

Figure 3. 29: Histogram of recorded rupture forces. Rupture forces were determined in nanonewton (nN) when a cantilever crosslinked to VAR2CSA fragment retracts afters approaching a plastic surface where CSA (1 mg/ml, black), CSA (0.1 mg/ml, light grey) or BSA (1 mg/ml, dark grey) is resorbed. The measurement was repeated 300 times with no dwell time for each approach-retraction cycle.

When calculating the adhesion rate i.e. percentage of force-distance curves that display a peak, I expect a low adhesion frequency and strength for the BSA surface, since all interactions between the surface and VAR2CSA should be non-specific.

However, I observed that the adhesion rate was too high, ranging from 10-36%, with the same conditions at different time points. Therefore, I could not discern the force profiles between CSA positive and BSA negative control surfaces.

Analysis of 300 force-distance curves revealed a 46 % adhesion rate between VAR2CSA and CSA (1 mg/ml) and a 61 % adhesion rate was observed for 0,1 mg/ml CSA. Detachment of VAR2CSA from CSA in high concentration, required approximately 76 pN during retraction. If CSA is present in a lower concentration, these forces were measured at 85 pN on average (45/300 events). However, when testing a BSA substrate (1 mg/ml) as a negative control the adhesion rate was 34 %, 10% and 36% in three non-consecutive measurements. The forces measured during these approach and retraction cycles were measured between 70-85 pN, which is the range measured for the CSA substrates.

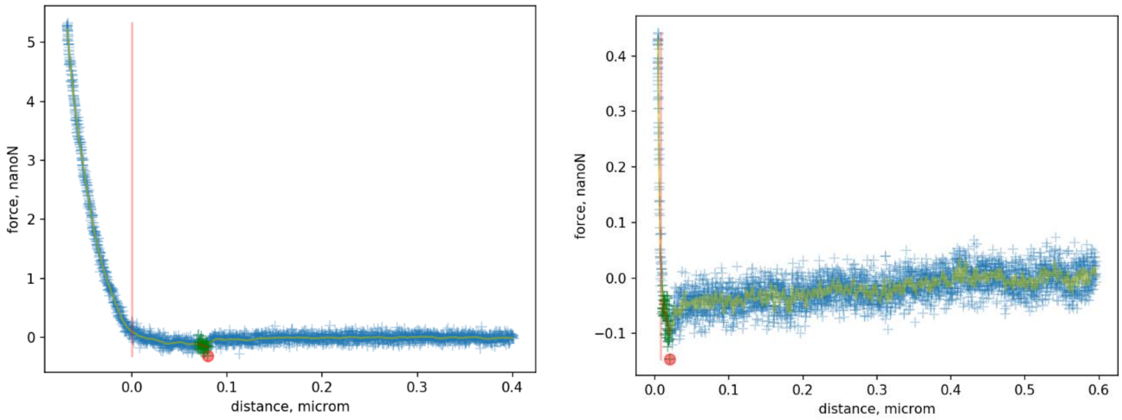

Figure 3. 30: Characteristic force-distance curves recorded for BSA resorbed on plastic. All points of the measurement are indicated as blue crosses. Red line indicates the start of the slope and all points leading to the peak are in green, while the highlighted red cross indicates force measurement peak.

When inspecting individual curves of BSA force distance curves (Figure 3.30), one can abstract the differences between measurements. BSA was approached first, then CSA in low concentration was measured and then BSA again. Compared to the initial measurement the detected noise is increased while force and distance recorded decrease.

3.2.2 Physiosorbed CSA/albumin on glass

After testing plastic surfaces, I tested glass substrates for CSA presentation as well. All other conditions remained constant, to ensure that the observations would be comparable. When using BSA (albumin fraction V), the force profiles recorded were in the same range with those recorded between VAR2CSA-CSA (Figure 3.31).

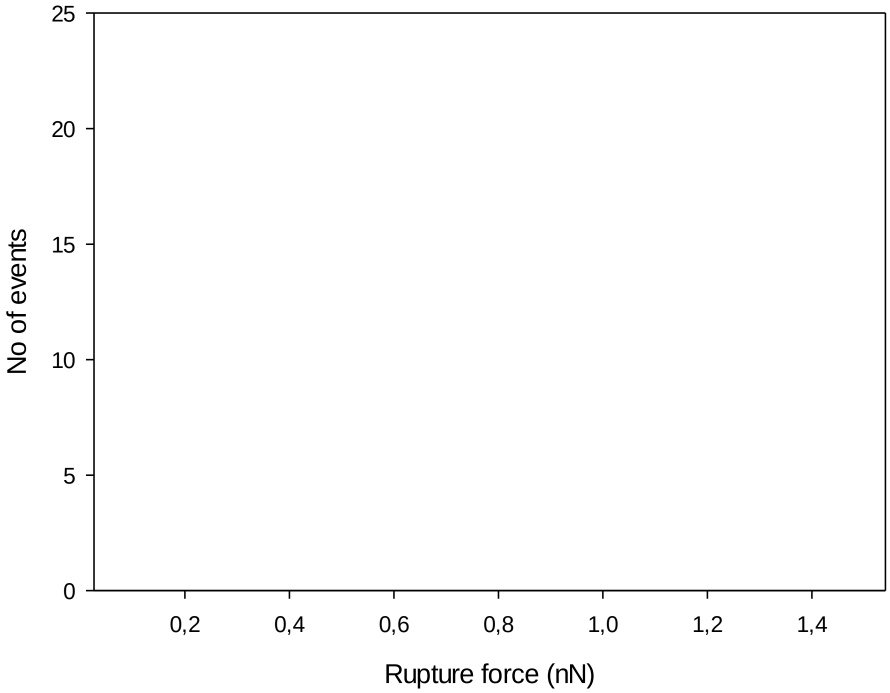

Figure 3. 31: Histogram of recorded rupture forces. Rupture forces were determined in nanonewton (nN) when a cantilever crosslinked to VAR2CSA fragment retracts afters approaching a plastic surface where CSA (1 mg/ml, black), CSA (0,1 mg/ml, light grey) or BSA (1 mg/ml, dark grey) is resorbed. The measurement was repeated 300 times with no dwell time for each approach-retraction cycle.

Forces that were recorded varied vastly depending on the time and date of the experiment. Adhesion with BSA initially was low (1 % adhesion rate, 200 curves), but with increase of dwell time the adhesion rate also increases to 24 % for 200 ms, and to 54 % for 500 ms. The same conditions yielded adhesion rates from 1.1 % (first measurement, 200 curves) to 68 % (third measurement, 1500 curves). Considering that BSA is inhomogeneous and a fraction of various albumin proteins, ovalbumin derived from chicken eggs, which is more homogeneous in composition, was also used.

Nonetheless, I could not detect significant improvements in specificity even when ovalbumin was used, with high adhesion rates ranging from 52 % to 31 % to 22 %. These values were obtained when alternating between positive and negative substrate measurements.

3.2.3 Alternative negative control substrates

I therefore tested other surfaces that are commonly used as negative control substrates due to their inert nature, such as hydrogels, polyethyleneglycol (PEG) coating and non-coated glass. PEG-coated glass surfaces were tested against a VAR2CSA-coated cantilever that unfortunately did not result in the establishment of a non-reactive negative control. The 300 recorded force-distance curves had 2 to 5 peaks per curve (Figure 3.32) and the adhesion rate increased from 68% at no dwell time to 100% when the dwell time was set to 1 second.

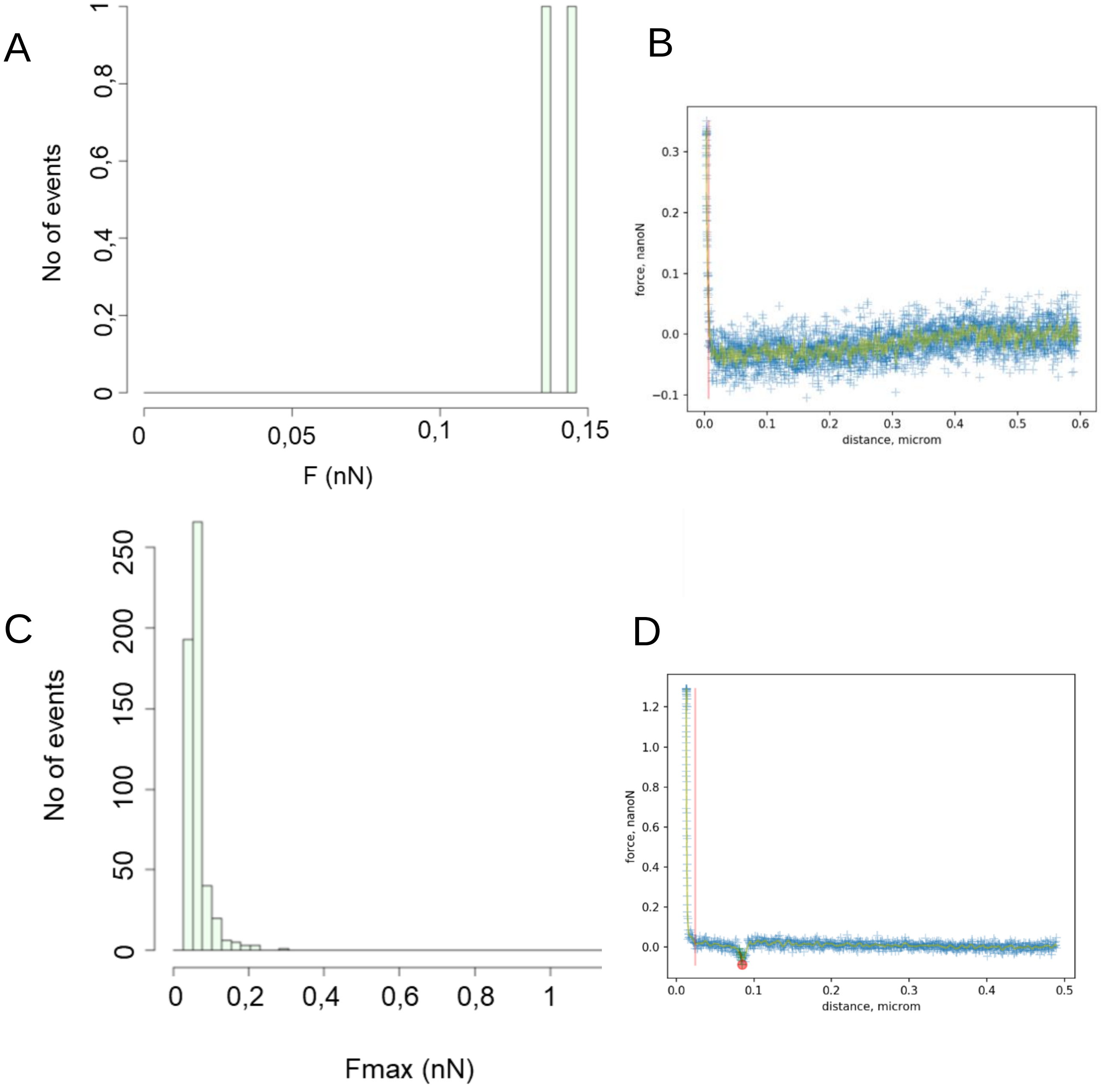

Figure 3. 32: VAR2CSA coated cantilever tip and BSA coated surface. A) Histogram of forces for initial VAR2CSA-BSA AFM. B) Characteristic force-distance measurement for initial VAR2CSA-BSA interaction. C) Histogram of forces measured for VAR2CSA-BSA after contact with a CSA-coated surface. D) Characteristic force-distance curve for second round of VAR2CSA-BSA measurement, after contact of the cantilever with CSA-coated surface. Red cross indicates peak, blue crosses indicate points of the measurement. Red line indicates start of a slope if present. N = 300 for all histograms.

In order to provide a stable negative control, I also tested a VAR2CSA-coated cantilever approaching uncoated glass. When the cantilever approached uncoated glass, the adhesion rate was at 99.9 % at zero dwell time (300 curves) and 100 % with 1 second dwell time. The maximum forces recorded were close to 250 pN, while breakaway distances were over 200 nm. This resulted in a clear dismissal of uncoated surfaces as negative controls, since they do not possess the desired characteristics of an inert substrate.

I further tested a hydrogel-coated surface, which is more uniform in composition, yet softer than glass or plastic, therefore willing to record lower forces at smaller distances at a low occurrence.

A spycatcher-coated cantilever was tested against a BSA-hydrogel-coated surface, high adhesion rates (40 %) even for measurements with no dwell times and high adhesion forces (up to 500 pN) were recorded. When testing this cantilever against a CSA-coated hydrogel surface, adhesion rates increased to 50 %, which was unexpected for this pair, as it should not interact at such a high rate. When dwell time was increased to 200 ms, adhesion rates reached almost 100 % for both BSA and CSA-coated hydrogels. This led to the dismissal of hydrogel coated surfaces, as the background measurements were already too frequent to provide a reliable background for positive control measurements. It is possible that due to the softness of the matrix, the conducted measurements recorded the changes in indentation compared to a harder surface.

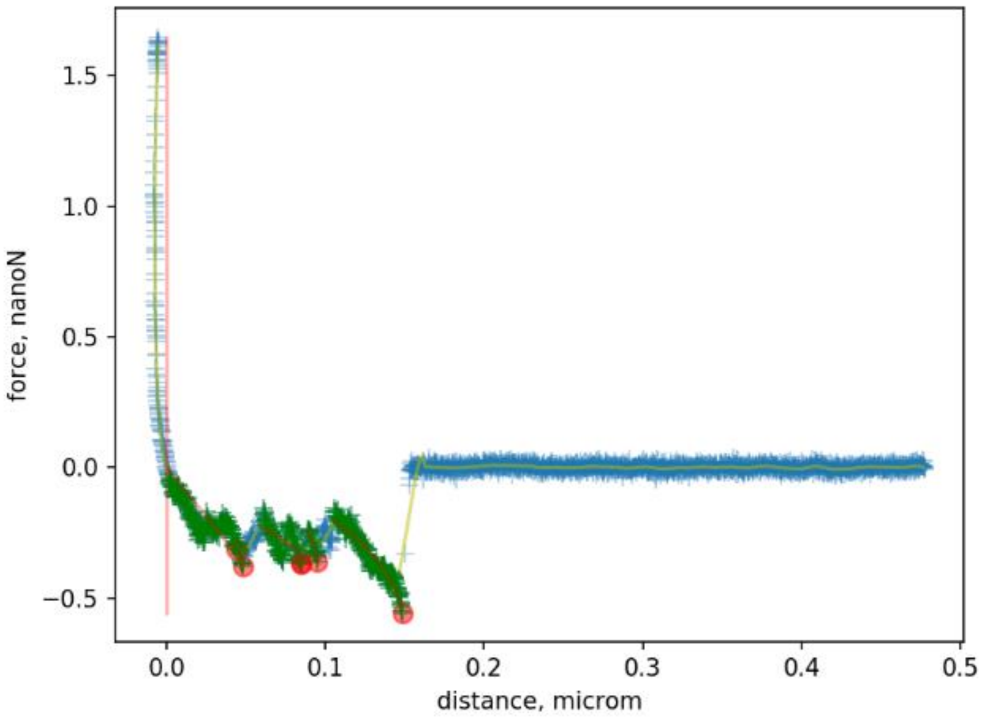

Figure 3. 33: Characteristic force-distance curve of a VAR2CSA-functionalized cantilever against a PEG-ylated surface with no dwell time at the surface. Peaks are indicated by red crosses, events recorded by blue crosses, and green crosses indicate all events leading to a peak if present. Red line indicates start of slope.

3.2.4 Biotin/Streptavidin

In order to exclude problems of the microscope and reduced sensitivity due to external factors such as outside noise, I used an established protocol on a known and well-characterized receptor-ligand pair, namely biotin/streptavidin**.**

The setup of VAR2CSA is not directly comparable to the biotin setup, as the protocols used are not identical. However, it is an attempt to validate a standard and confirm the correct function of the measurement. Biotin-BSA and PEG_{500}-biotin (Laysan Bio) are commercially available compounds and can be obtained in abundance, while our compound is rare, not-commercially available and requires a further modification of a spytag and the crosslinking of a spycatcher to the PEG-linker. Differences in the characteristic force-distance curves reflected the expected interactions between biotin-biotin (Figure 3.34 A) and biotin-streptavidin (Figure 3.34 B).

This approach provided valuable insights into the issues of the current setup. When measuring with this interaction pair, to obtain a set of clearly positive (biotin-streptavidin) and negative (biotin-biotin) interactions, with high (67,6 %) and low (6%) adhesion rates respectively.

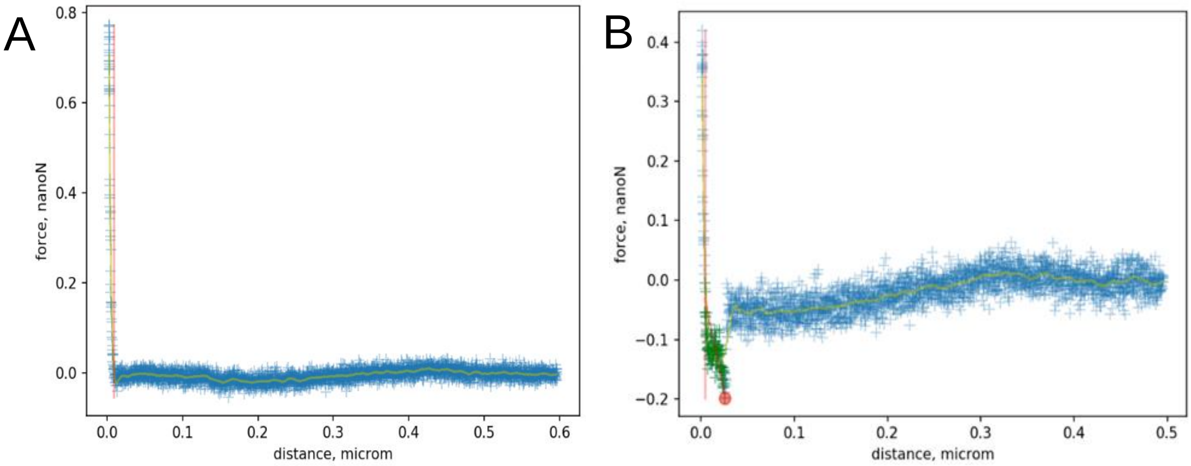

Figure 3. 34: Characteristic force distance curves for A) biotin-coated cantilever and biotin (physiosorbed) on TCP and B) biotin-streptavidin coated TCP. Peaks are indicated by red crosses, events recorded by blue crosses and green crosses indicate all events leading to a peak if present. Red line indicates start of slope.

Since PEG-biotin was used for these measurements as well, it is an indication that the PEG-linker molecule was effectively attached to the cantilever and did not specifically interact with BSA. Breakaway distances were also recorded and the results showcase once more the differences between biotin-biotin interaction (Figure 3.35 A) and biotin-streptavidin interaction (Figure 3.35 B).

These results point to the stability and reliability of AFM-based force spectroscopy, by showcasing single-molecule interaction force at 20 pN and breakaway distances of 5 nm on average.

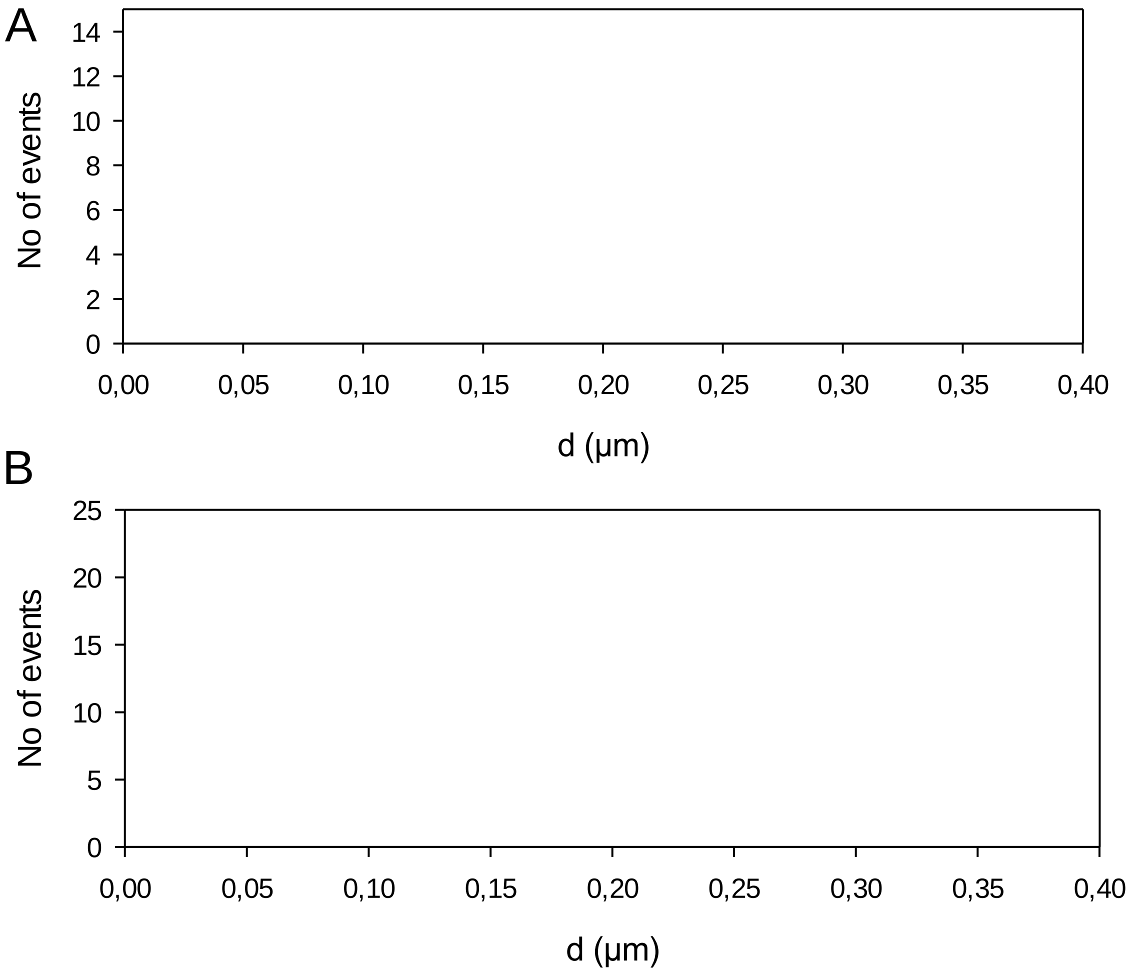

Figure 3. 35: Histogram of maximal breakaway distances for A) biotin-biotin interaction and B) biotin-streptavidin interaction.

3.2.5 Adhesion rate and dwell time

Even in setups where concentrations, dwell time and approach/retract rate were kept constant, adhesion rates between VAR2CSA and CSA (1 mg/ml) varied from 100 % to 29,6 % in four different measurements and the breakaway forces also varied from 50-200 pN, as seen in Figure 3.33.

When the dwell time was increased, I noticed an increase in adhesion in most cases. For example, when measuring on CSA, the adhesion rate of the VAR2CSA functionalized tip increased 10 %, from 88 % (no dwell time) to 99,6 % (1 s dwell time) in a consecutive measurement. On a different date, the same setup yielded an increase in adhesion rate of 80 %, when dwell time was increased from zero to 250 ms. This can be explained by the higher probability of bond formation due to an increased interaction time. However, when dwell time was increased even further, to 500 ms, the adhesion rate dropped approximately 20 %, (from 83 % to 64 %). This result could however be due to an oversaturation of the cantilever with CSA molecules, from previous measurements on the day.

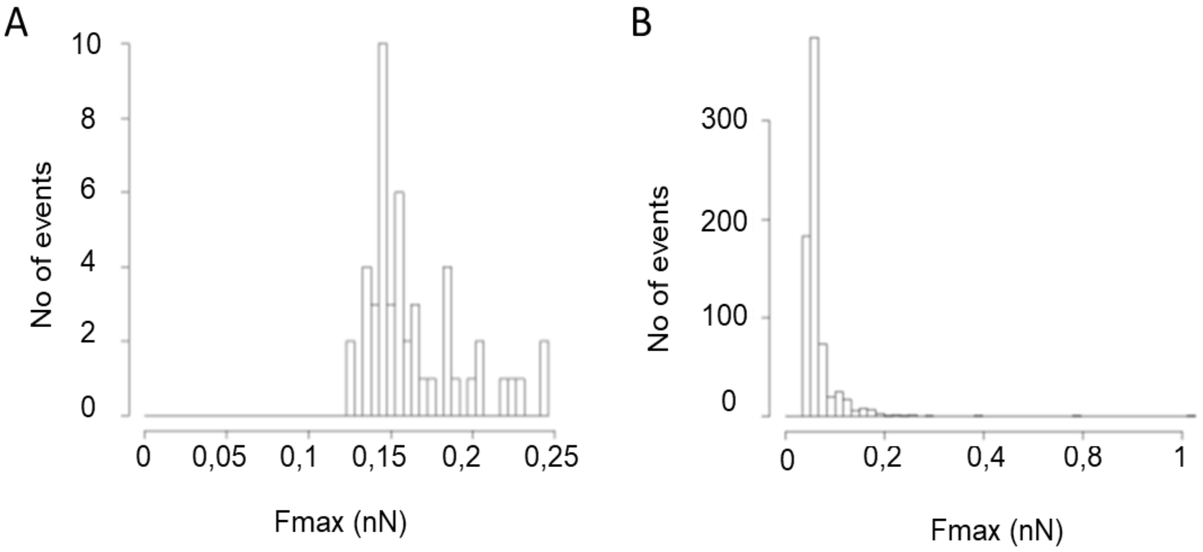

Figure 3. 36: Histogram of breakaway forces for CSA-VAR2CSA, 0 ms dwell time. Measured on A) 5.09.2019 or B) 8.8.2019. 300 approach-retract cycles per experiments were measured.

Even when measuring a substrate such as BSA or ovalbumin, we noticed a non-linear increase in adhesion when the dwell time was increased. In this case, when increasing dwell time from zero to 1s, the adhesion increased from 17,6% to 100%. However, when the increase was more gradual, increasing to 250 milliseconds (ms), and then 500ms in consecutive measurements we noticed that the adhesion rate first increased from 5% to 68% and then to 72,3%.

3.2.6 Negative control cantilever

When comparing spycatcher and substrate interaction, I noticed that the absence of VAR2CSA fragment did not have a significant effect in the measured values. Adhesion rates between a spycatcher-tagged cantilever and an uncoated glass surface was measured at 69% and low adhesion forces.

Interaction rates between ovalbumin and spycatcher were measured at 18 % while interaction with CSA was at 21 %. A CSA-coated hydrogel with covalently bound CSA, also interacted with the cantilever at a 52% rate. These rates are indicative of an interaction with high adhesion rates and low forces, under 20 pN, which complicated interpretation of spycatcher-spytagged var2csa and any substrate (Figure 3.37 and 3.38).

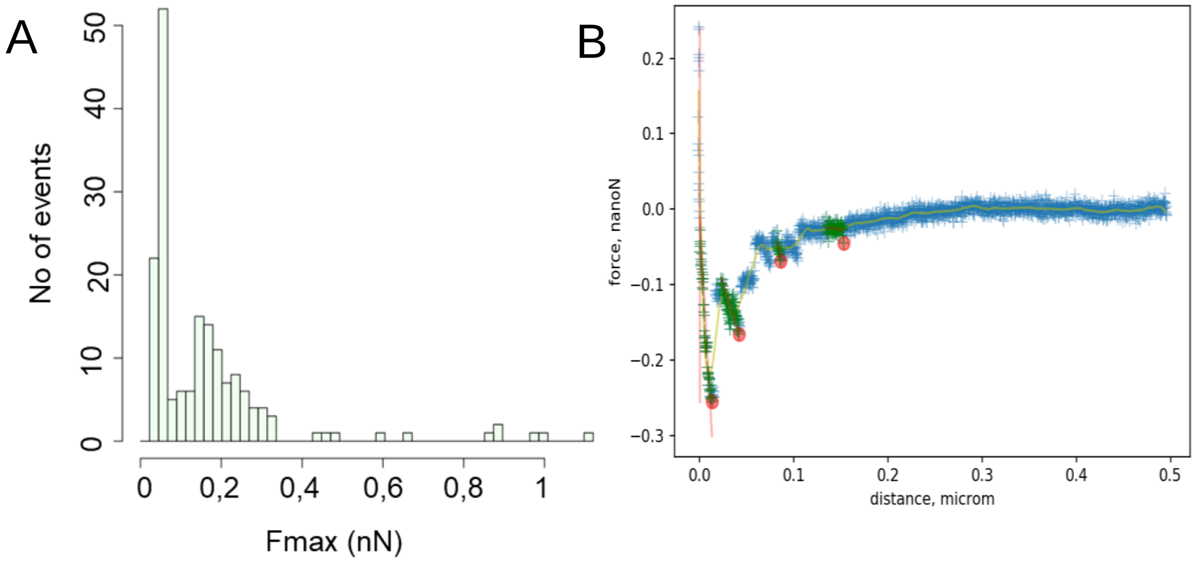

Figure 3. 37: A)Histogram of recorded maximal forces and B) force-distance curve for spycatcher-coated cantilever and CSA (1 mg/ml, physisorbed) on TCP during 300 approach-retract cycles with no dwell time.

Therefore, we cannot exclude the possibility that specific interactions with a lower adhesion force are obscured by unspecific interactions of the flexible PEG-spycatcher arm attached to VAR2CSA. In both cases, multiple peaks were detected in a majority of the recorded force-distance measurements, pointing to multiple interaction sites at relatively short distances (less than 200nm, Figures 3.37 B and 3.38 B).

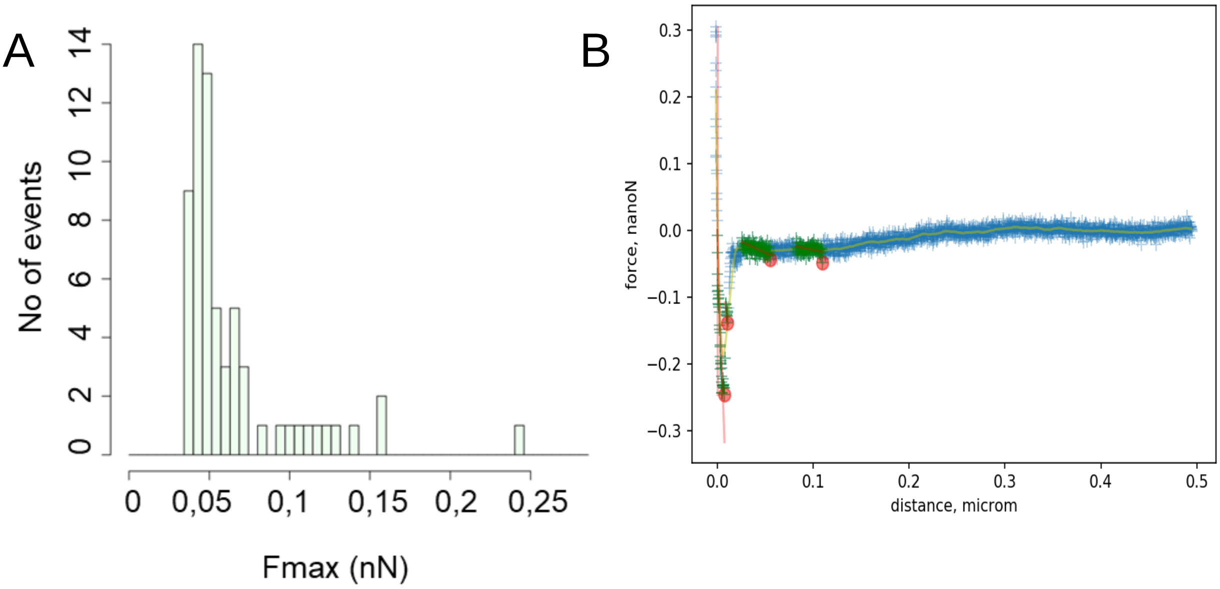

Figure 3. 38: A) Histogram of recorded maximal forces for spycatcher coated cantilever and BSA (physiosorbed) on TCP during 300 approach-retract cycles with no dwell time. B) Characteristic force-distance curve for measurement between spycatcher-coated cantilever and BSA (physiosorbed) on TCP.

3.3 Aim 3: Rosette position in flow

Rosettes form spontaneously in culture and rosetting frequency was monitored and increased through frequent rounds of gelatine flotation and observation. Rosettes can contain more than one parasitized erythrocyte attached to two or more uninfected erythrocytes. Some characteristic rosette clusters can be seen in Figure 3.39.

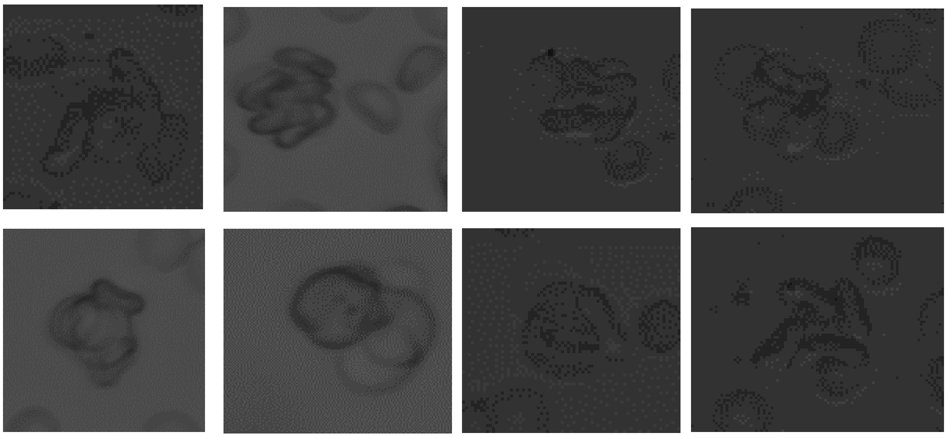

Figure 3. 39: Rosette formation in culture. Brightfield images captured with 100x oil-immersion microscope (KERN).

3.3.1 Rosetting culture and frequency

Rosetting frequency was estimated as described in Section 2.2.3.6. Rosetting frequency was lower than expected before enrichment and measured between 30-40 % after only a few replication cycles. Frequency never reached 100%, but increased to 75% after at least four rounds of gelatine flotation. Rosette frequency was not affected by blood type and remained at the same levels when using O+ or A+ packed erythrocytes. MACS purification of rosettes did result in some disrupted rosettes, nonetheless flow chamber experiments following this selection could be performed without further need for rosette isolation and rosettes were not disrupted by the introduction of flow.

3.3.2 Effect of blood type on rosette formation

We also observed differences in rosette size when using packed O+ erythrocytes or packed A+ erythrocytes for the same strain of rosetting parasites. As documented in literature [195], A+ rosettes are larger in size, often composed of 5 or more erythrocytes, while O+ rosettes are smaller in size, on average composed of 3-5 erythrocytes.

3.3.3 Multiple infectivity and invasion rate of rosetting cultures

Infectivity rates and multiple invasion were also measured in cultures of rosetting parasites and A+ erythrocytes. For this strain, multiple invasion was the norm both for ring stage parasites but also multiple surviving up to schizont stage within one erythrocyte (Figure 3.40).

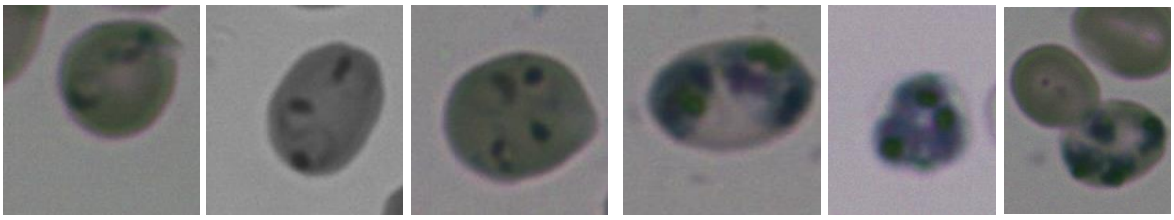

Figure 3. 40: Multiple infections in single erythrocytes of rosetting strain. From left to right: Giemsa stained ring stages of two, three and four parasites, and trophozoite stages of two, three and four parasites.

3.3.4 Rosette behaviour in flow

While rosette formation and occlusion of small microcapillaries by these structures has been observed, it is not clear how rosettes behave in broader vessels with higher flow rates. Different haematocrit conditions had to be set up in order to provide reliable data on the position and behaviour of rosettes in correlation with surrounding blood components and increasing erythrocyte concentration. In order to determine the hydrodynamic behaviour of rosettes, I set up a platform to observe their composition and position under a given shear rate**.** Using a narrow flow channel (Ibidi µ-slide 0.1 VI), I was able to record the behaviour of rosetting erythrocytes. Non-fixated rosettes can be seen under a microscope (40x, Brightfield) without the need for fluorescent markers (Figure 3. 41).

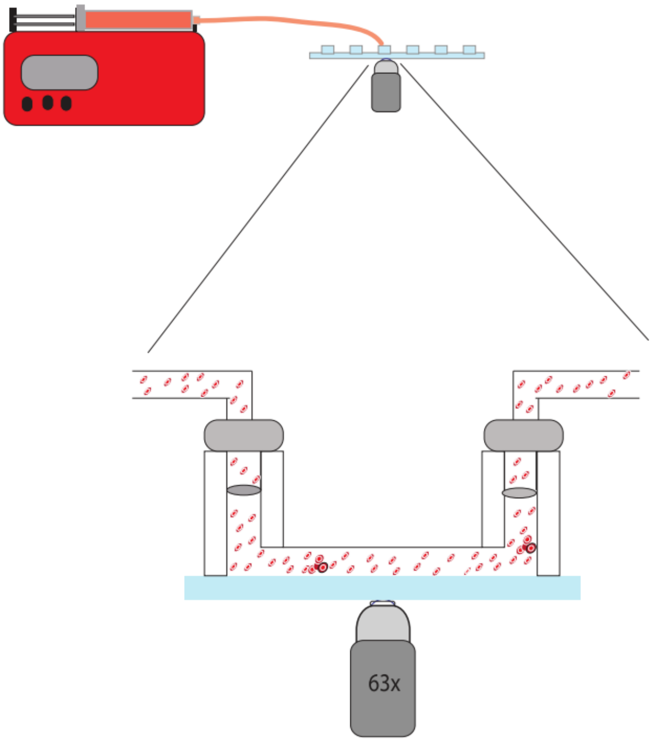

Figure 3. 41: Setup for observation of rosettes in flow. A syringe containing rosettes at given haematocrit is connected to a Harvard pump apparatus and a 0.1 Ibidi flow chamber with a glass substrate is placed on the stage of an inverted ZEISS Axiovert microscope and observed at 63x magnification. Adapted from manuscript in preparation.

In a low haematocrit setting of cell culture conditions it was possible to measure rosetting frequency and separate rosetting parasites from non-infected erythrocytes. However, when the haematocrit was adjusted to 13 %, it was already not possible to objectively distinguish the rosettes from non-clustered erythrocytes (Figure 3.42).

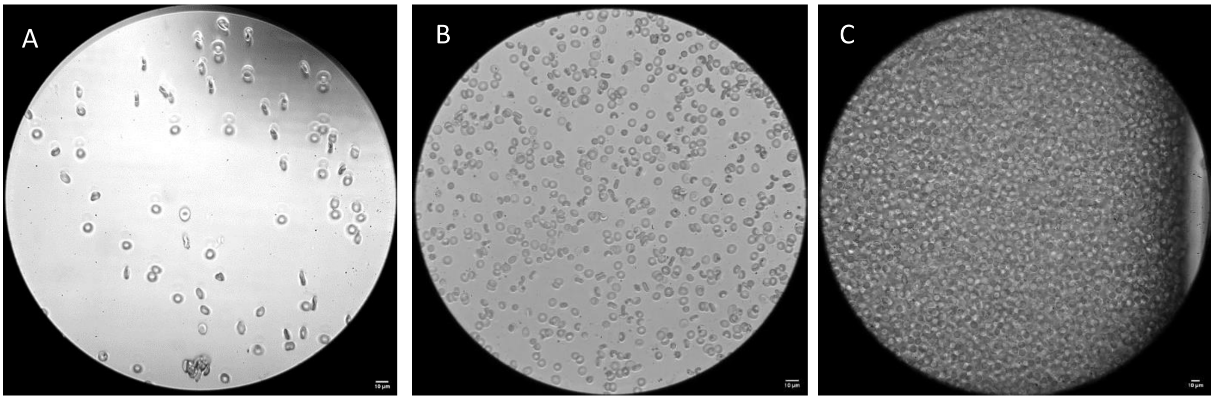

Figure 3. 42: Brightfield image of flow chamber with A) low, B) intermediate and C) high haematocrit values with rosettes. 63x oil immersion objective. Scale bar is 10 µm.

I then devised a strategy that would allow the detection of a rosette within the channel even in a higher haematocrit and faster flow rates. This required a fluorescent tag of the erythrocyte membrane to distinguish between a rosette and stacked erythrocytes under flow. Another requirement that had to be met is the use of a highspeed camera, capable to perform these imaging techniques with clarity even during high pressure flow (Figure 3.42). To prevent large numbers of cells sticking to the channel, prior to use, the Ibidi channels were incubated with 1 % BSA and then washed using a syringe pump containing binding buffer. The rosettes were separated via MACS purification and stained with CellBrite^{TM} membrane staining (644/665 nm). Rosette separation via gelatine flotation or Percol protocols were not considered as a large number of uninfected erythrocytes were included in the fractions with the rosettes and did not result in an effective rosette enrichment suitable for experimental purposes.

The staining protocol provided by the manufacturer was followed and the incubation time was optimized with regard to infected erythrocytes in rosettes. The rosettes were first imaged in static conditions within a 0.1 mm Ibidi channel. Subsequently, a constant wall shear stress of 0,05 Pa was set and the passing rosettes were recorded with regards to their composition (number of erythrocytes) and height position in the channel. In order to approach *in vivo* conditions more closely, the haematocrit was adjusted to 20 % and 40 %, with AA packed erythrocytes added to the MACS separated rosettes and imaged in the 547 nm channel (Figure 3.43). The stained erythrocytes could be captured in flow, after finding a balance between frame rate and resolution. Intensive experiments runs using low flow rates resulted in sedimentation of both uninfected erythrocytes and rosettes within the plastic tubing and increased with higher haematocrit values. These problems could be avoided by intermittent increase of flow and change of flow direction (push/pull) between recordings, or by shorter recording times.

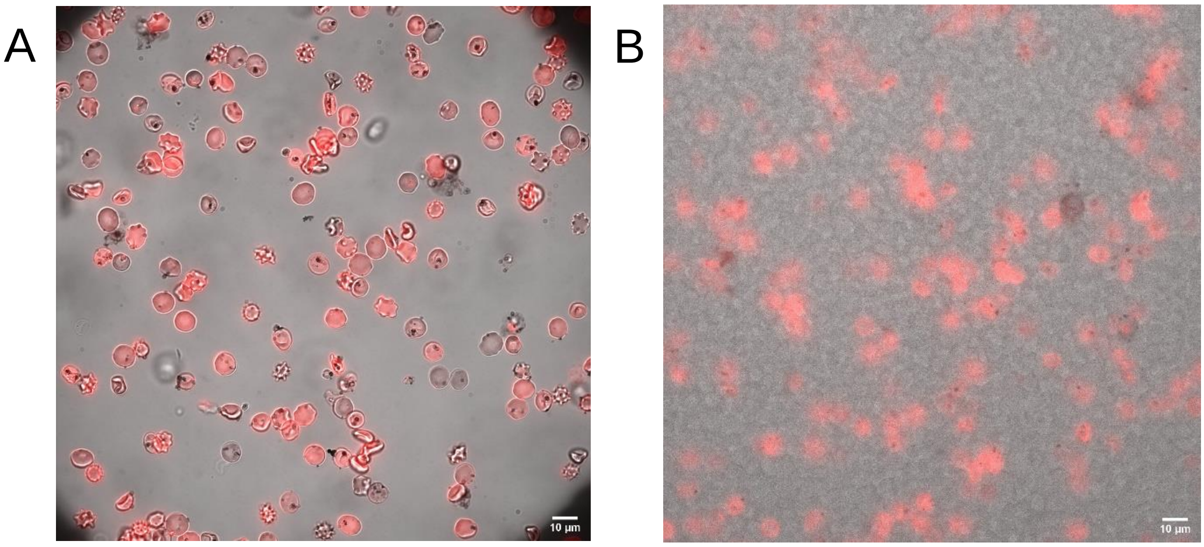

Figure 3. 43: Detection of rosettes at high haematocrits and low flow rates. A) Stained rosettes after MACS purification. B) Composite of brightfield and channel 547 nm (orange) to visualize stained rosettes in non-labelled, highly concentrated erythrocyte solution. Scale bar is 10 µm.

In experiments with high haematocrit values (> 10 %), images of rosettes were only captured in satisfactory numbers after several hours of imaging and several sessions and were much smaller in size (average of 3 cells) than those measured in low haematocrit values. The majority of captured rosettes were larger in size, with some recorded to have a composition of over 7 erythrocytes in intermediate and low haematocrit concentration.

Initially starting the measurement at the glass surface termed 0, I recorded the number of rosettes observed at each height and recorded their z, y, and x coordinates for low and high haematocrit values (Figures 3.44 and 3.45). Refining the setup when measuring intermediate haematocrit to increase the statistical power of the respective, I kept x and y coordinates constant while only varying z coordinates to identify margination (Figure 3.46). In non-physiological haematocrit (average 7.5%), I saw a slight tendency for margination but still not as pronounced as is seen in single infected erythrocytes (Section 3.1)

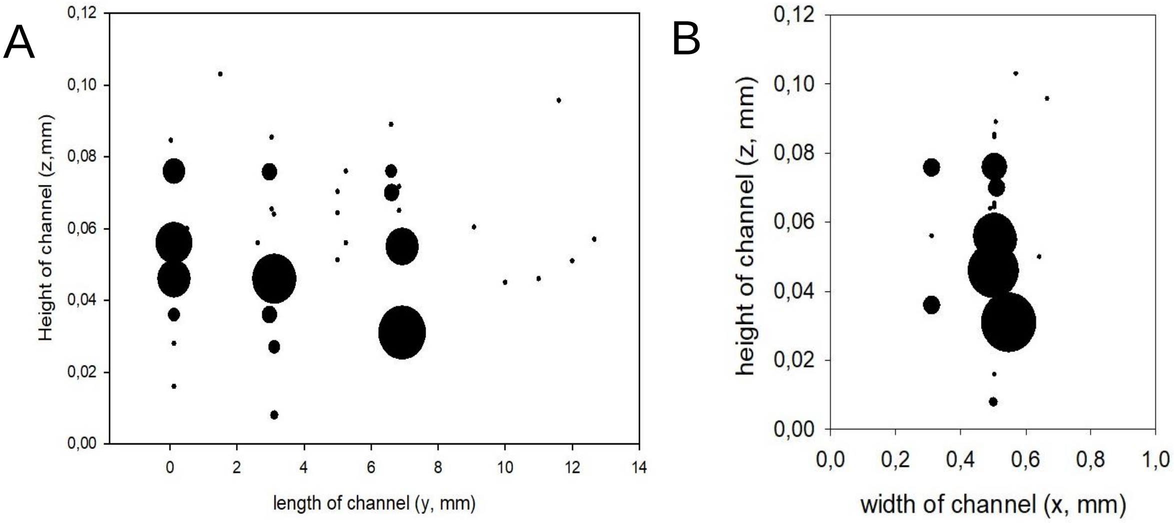

Figure 3. 44: Bubble plots of A) height (z) and length (y), and B) height (z) and width (x) coordinates of rosette tracked in channel. Walls of the channel were at positions 0 to 0.2 mm and 0.8 to 1mm and total channel length was 14mm. (N = 94) **.** Haematocrit was at 7.5% on average and WSS at calculated to be 0.05 Pa within the channel.

In non-pathological haematocrit values (40 %), rosettes were recorded within the centre of the channel, mainly away from the walls when considering z position in the flow chamber (Figure 3.45 A). However, when considering x position, I observed rosettes closer to the edges of the channel at 0 to 0.2 mm (Figure 3.45 B). It is possible that this is an artifact of the chamber, with an obstruction in the x axis causing changes in the position of the rosette only in this aspect.

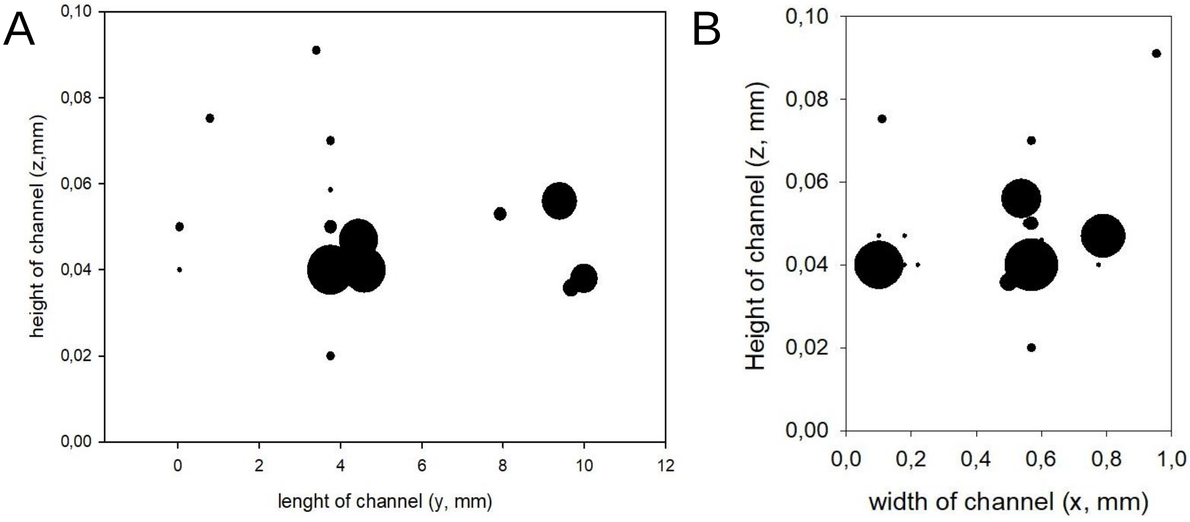

Figure 3. 45: Bubble plots of A) height (z) and length (y), and B) height (z) and width (x) coordinates of rosette tracked in channel. Walls of the channel were at positions 0 to 0.2 mm and 0.8 to 1mm and total channel length was 14mm**.** (N=87). Haematocrit was at 40 % on average and WSS at calculated to be 0.05 Pa within the channel.

There is also a difference in recorded rosettes at the y axis, as compared to larger rosettes seen at lower haematocrits in the inlet of the channel (position 0 for y axis, Figure 3.44 A). This is not the case for the smaller rosettes seen at the highest haematocrit values (Figure 3.45 A). I also observed differences in the x axis position, where in lower haematocrits rosettes were remaining in the centre of the x axis (0.5 mm, x, Figure 3.44 B), while for high haematocrit (40 %, Figure 3.45 B) this was not the case.

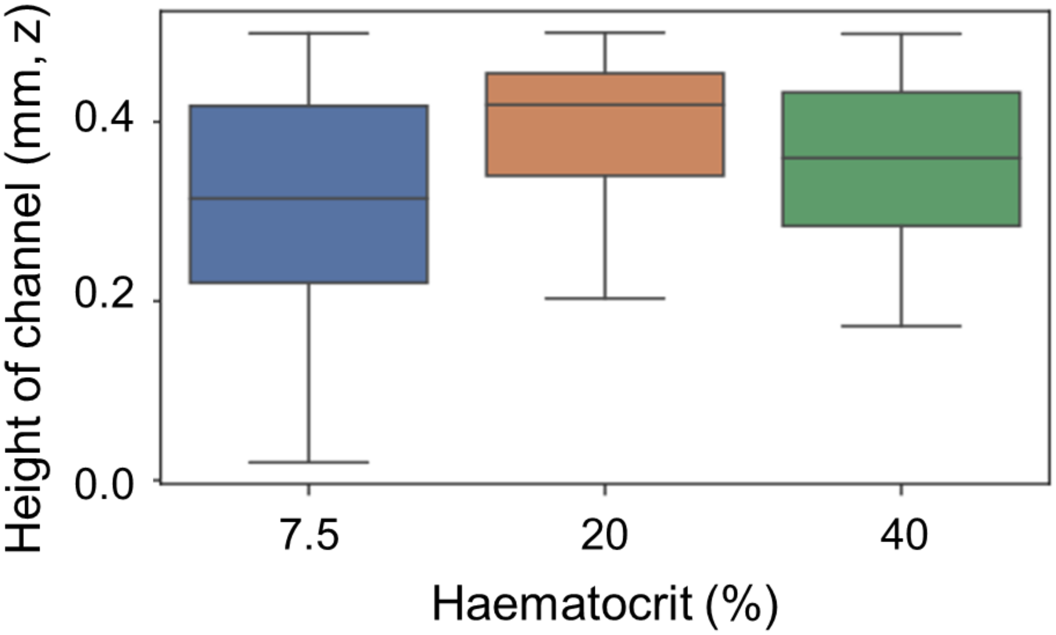

Figure 3. 46: Rosette position for z axis (height of channel) at three different haematocrit values. Z coordinates measured in narrow Ibidi flow chamber and randomised within three layers from the wall (0 mm) to the centre of the channel (0.5 mm). For low haematocrit (7.5 %) N = 94. For intermediate haematocrit (20 %) N = 174, and for high haematocrit (40 %) N = 84. Standard deviation and median shown with black lines within the box plot. Analysis performed by Dr. Anil Dasanna (manuscript in preparation).

Cell mass was expected to be a main factor favouring margination. Thus, the most important parameter to observe was the position at the z axis, as this is the one affected by gravitational forces. In a cumulative plot (Figure 3.46), adapted from Dr. Anil Dasanna´s publication draft (in process), it is clear that rosettes do not marginate towards the wall of the channel (0 to 0.2 mm, z) but rather remain in intermediate positions (0.2 to 0.4 mm, z) for lower haematocrits at 0.05 Pa WSS. For 40 % haematocrit values, rosettes also do not marginate to the wall but are found in the centre of flow (0.4 to 0.6 mm, z). These experimental data are in good agreement with simulations performed by Dr. Anil Dasanna at the same haematocrit and WSS values (data not shown, publication manuscript in process).

4. Discussion

In the ongoing battle against the spread of malaria infections, it is crucial to understand the mechanisms that contribute to the survival of the parasite in order to identify future drug targets and develop strategies to counteract the prevalence of the parasite in the human host. Cytoadhesion is vital for the survival and asexual propagation of the parasite and has been the subject of many studies over the years, attempting to understand this process and targeting the involved interactions as a way to decrease parasite load in the case of infection.

P. falciparum infected erythrocytes are able to adhere to the endothelium by expressing adhesins on the surface of the host cell that enable the sequestration of the cell onto the endothelium, thus evading splenic clearance. While the interaction is well-known, the phenomenon is still poorly understood as most studies focus only on static adhesion assays to identify the molecular players. It is however very important to also consider that adhesion takes place in flow in the human body. Therefore, it is key to understand the effects of sheer stress, cell morphology and rheology in microvessels, and achieving a closer simulation of *in vivo* adhesion with *in vitro* techniques can help in that sense. Obviously this is a very complex interplay with several varying factors that need to be considered, therefore I approached these questions with three different aims in mind.

4.1 Aim 1: Adaptation of platform to visualize contact area for mature stage parasites in HbAA and HbAS *Pf* infected erythrocytes

Within this project, I optimized a platform originally developed to study molecular interactions between leucocytes [177] and the endothelium in flow, and adapted it to investigate the interactions between infected erythrocytes and the endothelial receptor ICAM-1 in flow. Additionally, I used the platform to evaluate the differences between adhesion tracks of mature-stage parasites within haemoglobinopathic (HbAS) and wild type (HbAA) erythrocytes. Based on previous studies and simulations [102, 150, 155], it was shown that altering physiological properties of the membrane rigidity and tension has an effect on the dynamic adhesion of parasitized erythrocytes. It was also shown before that there are significant differences in the adhesion in flow of parasitized HbAA and HbAS erythrocytes. These differences were attributed to the differences in membrane tension and rigidity as well as the differences in expression of adhesins on the surface of parasitized cells [87, 102, 155].

For the first time, I was able to show the contact area of a *P. falciparum* infected HbAA and HbAS erythrocyte onto ICAM-1, a protein constitutively expressed on the surface of the endothelium of blood vessels. Based on the results of this study, the contact area during dynamic adhesion, from heron referred to as track, varies between parasite stages and is influenced primarily by the cell shape and rigidity of the membrane (Figure 3.17 and Figure 3.23). While simulations performed previously [102] were in good agreement with HbAA width and overall density, I observed areas of high adhesion probability with a large amount of receptors in close proximity involved.

These areas, termed spots and patches (Figure 3.18) depending on their size, were not predicted. Patches seem to be weighted to one side for HbAA (Figures 3.17 and 3.18) while for HbAS (Figure 3.25) erythrocytes they seem to cross or remain in the centre of the track.

4.1.1: The platform setup and optimization

The main limitation but also an advantage of our system was identifying the track and correlating it to a particular dynamic adhesion behaviour. As the platform employs a secondary detection step for the tracks, these are easier to identify and measure without having the impact from sheer stress and flow. However, this is also an inherent problem of the setup as it is not possible to identify the track in real time. Therefore, each TIRF image has to be very carefully considered as to what can be termed an adhesion track. Due to this, in order to ensure that the tracks recorded are indeed the result of specific dynamic adhesion of mature stage infected erythrocytes, several validation and negative control experiments had to be designed and performed (Figure 3.1.8 and 3.1.9). Considering the possibility of non-specific interactions between cells and the setup, I tested parasitized HbAA cells with all components of the platform except for ICAM-1 (Figure 3.1.9). The lack of a specific signal highlights that there were no interactions with components of the surface as well as the specificity that PfEMP1 adhesins show towards ICAM-1. Uninfected erythrocytes and beads were also tested in the same conditions with sensors, as well as ICAM-1 presence, to exclude the possibility that tracks are created not by specific adhesin interaction but rather by mechanical stress exerted by erythrocytes in flow. It is interesting to note that while being able to detect strong signal that validates the platform, the signal for TGT containing surfaces displays a grainier quality with some aggregations (bigger, more intense spots) spread throughout the sample. In some cases of images taken for validation purposes, while the signal was evenly distributed from top to bottom, there appeared a slight gradient that could not be avoided due to irregularities in the glass substrate from left to right. TIRF measurements are highly sensitive to even the slightest protrusions, leading to a shade gradient.

Recording the surface of our platform using RICM allowed us to interpret the differences in simulated and experimentally recorded tracks as well as to formulate a hypothesis on how membrane morphology and adhesin presentation influences the contact area and motion of the cell during dynamic adhesion in flow.

As discussed above, the platform is powerful due to the relative binarity of the signal (Figure 3.17 A, black and white) that facilitates the signal interpretation and further analysis of the track. However, due to the problems that arise because of the secondary detection step, one possibility is to employ a more complex sensor, emitting a signal that can be measured in real time [196, 197]. Signal intensity could then be correlated to adhesion strength, thus further approaching its quantification at specific sheer rates. However, due to the nature of these bonds, these changes require a highly sensitive detection system. The introduction of flow during the measurement of fluorescent intensity will also further complicate matters , as it requires a camera with a fast shutter speed that can capture changes in intensity occurring at very short time frames. In addition, the current system has the advantage of the sensors being irreversibly unzipped regardless of interaction strength and time, highlighting every interaction point that surpassed the threshold of 12 pN binding force.

While having a lot of advantages, data obtained with this setup had to be carefully interpreted, as one cannot make a safe assumption regarding non-continuous tracks with similar or the same trajectory. This led to the isolation of only continuous tracks, since interrupted tracks could be the result of a different cell in the same trajectory at a later or earlier timepoint.

4.1.2: HbAA infected erythrocytes: correlation between cell track and motion

For trophozoite-stage parasites, both RICM and TIRF data correlate well, following transient adhesion patterns of a flipping cell motion [175]. The appearance of patches weighted to one side at lower sheer rates results in a flipping motion of the cell, while the less dense but still present signal indicates a continuous contact of the erythrocyte to the surface. In order to remain close to the wall and eventually sequester onto the endothelium, the cell has to attach with a high number of receptors. Therefore, these results confirm the specific and continuous adhesion of PfEMP1 receptors to ICAM-1 when sheer stress is applied.

Schizont-stage maturation of the parasite results in a rounder and stiffer cell [150], presenting PfEMP1 molecules in similar amounts as trophozoite stage infected erythrocytes. Our results indicate that the circumference of those rounder cells is in constant contact with the surface and these tracks most likely correspond to rolling adhesion [175]. Since the average size of the recorded tracks for schizonts is approximately half the size of trophozoite tracks (2,6 µm and 5,8 µm respectively), these results highlight the importance of cell morphology during dynamic adhesion to the endothelium. The higher number of recorded tracks in a single TIRF image, as shown in section 3.1.3.2, could be the result of more frequent contact of schizonts with the surface. This phenomenon could be due to the changes in rheological behaviour of a stiffer cell, marginating out of the centre of flow with higher probability. Contact area reduces with maturation, as evidenced by the comparison from early to late trophozoites and schizonts. Late schizonts cannot be measured as they tend to rupture during measurement or even during MACS purification.

As the cells come in contact with the surface, the PfEMP1-protein attachment unzips the sensors, detaching ICAM-1 molecules from the surface. We cannot anticipate how long this interaction lasts and whether the receptors are accumulating on the surface of the erythrocyte or not. This accumulation can be safely assumed for the initial unzipping of the sensors, nonetheless bond lifetime cannot be estimated. Therefore, one should also consider the possibility of PfEMP1 adhesins remaining attached to ICAM-1 for the duration of the experiment and being blocked from further interaction. During the dynamic adhesion *in vivo*, interaction with the endothelium most possibly does not result in a dislodging of ICAM-1 during adhesion and is rather forming bonds with a short lifetime in order to continue its motion.

Analysis of smaller patches resulted in spots still too large to correlate to one knob alone (approximately 80 nm [87]). Due to the fact that several PfEMP1 molecules can be found in one knob, resolution is not corresponding to a single knob, but rather to several ones in very close proximity and cannot be resolved further in this imaging setup. That led to the conclusion that, while providing high resolution, this technique has its limitations and cannot resolve a single-molecule or single-knob to sensor interaction.

Cells were effectively washed out after measurement at high sheer rates, to ensure signal integrity. During measurements within the WSS parameters recorded for microvessels, some cells would still remain at the same spot, either mechanically restrained at this position or more likely tightly adhering to the receptors of the surface. In order to remove these cells, sheer rate was gradually increased until all cells were removed from the surface. Addition of a TGT-probe to detect ruptured oligonucleotides was performed, as discussed, in a secondary step. Ensuring that the introduction of flow alone, even when applying higher sheer rates was critical and did not result in a specific or strong signal (Figure 3.9 A). While an advantage for signal interpretation and ease of use, this procedure cannot correlate a specific sheer rate to a specific track. For further use, this is an important trade-off to consider and respective concessions have to be made.

4.1.3 AA infected erythrocytes: correlation between cell track and motion

While HbAA cell tracks were in good agreement with previous observations and simulations performed for the respective stages of parasite maturation, tracks and videos of HbAS infected erythrocytes are difficult to interpret. Overall, track width shows a reduction in width as the parasite matures, a trend also observed in HbAA erythrocytes. However, when considering the length of recorded tracks, it appears that contact with the surface is not as continuous for parasitized AS erythrocytes. Gaps and larger adhesion patches correlate to stronger adhesion at fewer larger areas. Considering that knob number most likely decreases while knob size increases, the patches within the tracks correspond to these changes, with a less dense track containing more patches. These patches are likely to act as temporary anchors as the cell rolls over the endothelium.

Surprisingly, as seen in RICM videos, I observed a small number of cells that appeared to follow a sliding motion rather than a flipping adhesion. Sliding could be described as a cell not flipping or rolling onto the surface, but rather remaining in contact with the same surface areas exposed continuously during the measurement. This is a curious phenomenon, because while this motion can be characterized in terms of rheological behaviour of a membranous structure, the interaction of a parasitized erythrocyte with ICAM-1 in terms of biological possibility is challenging. While it is unusual, sliding behaviour might possibly also provide an explanation as to the position of patches within the track. A cell that remains in contact with the surface from the same side and is rigid, possessing a higher membrane tension than HbAA erythrocytes, exposes the same receptors on the one side of the cell. Due to the saturation of exposed PfEMP1-

receptors on one side of the membrane, the track is either interrupted or non-saturated PfEMP1 located in proximity are more likely to interact. This could be a plausible reason for the observed position shift of patches seen in some of the recorded AS tracks for trophozoite stage parasites. Patches were much more frequent but smaller on average compared to HbAA. A possible reasoning for this result is the morphology of the cell, with AS erythrocytes being less flexible even at trophozoite stage compared to AA erythrocytes. Thus, accessibility of the presented receptors is also altered. The tracks for schizont-stage infection in HbAS cells were less frequently recorded than in HbAA cells. Comparing a wide field of view, HbAA schizont adhesion occurred more often and in higher numbers. This observation is in agreement with the hypothesis that due to less efficient adhesion, infected HbAS erythrocytes circulate longer in the blood and therefore would be more likely to be cleared.

4.1.4: Conclusion and future experiments

The results of this project highlight the importance of sheer flow and cell morphology in binding dynamics of parasitized erythrocytes. While static adhesion assays would showcase similar amounts of cells adhering in different maturation stages, when observed in flow, this picture changes drastically. Trophozoite stage parasites seem to bind less frequently but more efficiently onto the simulated endothelium. Also, schizont stage parasites alter the cell morphology to such an extent that adhesion is more likely but with less contact area and density of involved receptors. Changes in the membrane morphology between AA and AS erythrocytes also underline the significance of receptor presentation and accessibility influencing binding efficiency. Therefore, it is imperative that further studies performed include measurements of flow and rheological behaviour of adhering parasites. In the future, when developing strategies to combat severe malaria after infection, it might be worth considering that inducing changes in the membrane morphology might result in a reduced cytoadhesion.

If developed further, this platform could also be employed to standardize adhesion quantification and characterize adhesive behaviour of other strains of *Plasmodium*, or other aberrant phenotypes of cell structure. How this setup is structured makes it possible to alter the exposed protein without the need for optimization. Different receptors, such as CD-36 or EPCR can then be tested. The introduction of flow would also highlight the specific adhesion dynamics between these receptors and their PfEMP1 ligands, providing valuable insights into the interplay of sheer stress and ligand affinity. In this setup, only ICAM-1 in its recombinant form was employed. This was done in order to observe the specific interaction between this protein and PfEMP1, and to provide qualitative data of this interaction. However, there are arguments that suggest a cooperative binding onto different receptors, which in some cases can facilitate adhesion of infected erythrocytes. Therefore, it would be interesting to investigate this further with the introduction of a second receptor onto the substrate with a different sensor. It is possible that the interplay is required for more efficient cytoadhesion and sequestration, and using our optimized setup as a template for these investigations would add valuable insights to the field.

4.2 Aim 2: Quantification of *P. falciparum* PfEMP1 binding strength to its receptor

When investigating single molecule dynamics, the optimal setup to observe adhesion dynamics when the force profile is not known is AFM based force spectroscopy [198-200]. This microscopy technique is the preferred scanning electron microscopy technique for biological applications. It is often selected due to its operating simplicity and ability to measure nanomechanical properties of macromolecules at piconewton (pN) sensitivity and for distances at Angstrom (Å) resolution [201]. It is however complicated to interpret measurements and one needs to consider limitations and parameters that could affect measurements [200, 202].

Reduced or impaired adherence to endothelial cell receptors has been proven to reduce the risk of severe malaria. Aim 2 of this thesis was to extend these conclusions by simulating adhesion of VAR2CSA receptor to its substrate CSA and monitoring the adhesion strength and specificity using force spectroscopy by AFM. In contrast to PfEMP1 ligands, other protein binding and folding mechanisms as well as receptor-ligand pairs have been characterized in detail [203-207]. However, even studies on well-characterized pairs like as biotin-streptavidin, are not in agreement with the literature regarding the recorded forces, highlighting the effect of the apparatus and setup used , crosslinking protocols of respective partner proteins and conditions of the measurement on recorded values [208].

To my surprise, in my experiments the first challenge was to establish a protocol for blank non-reactive surface to use as a reference point for further measurements. However, when testing non-coated surfaces, I recorded high forces, in a frequency and range not common for biomolecules [209]. This is most likely due to the forceful impact of a coated tip against a hard surface such as glass or plastic, during approach. Commonly used as a reference for non-specific interactions, hydrogel coated surfaces were also tested in our setup. As these surfaces are much less rigid, only forces of indentation in a soft matter could be recorded. The high forces and high adhesion rates observed, even with passivated or non-functionalized substrates, may be due to non-specific interactions occurring between the cantilever and the surface. These interactions could include mechanical retention of the cantilever by larger aggregations of protein, interaction between uncoated surfaces of either the cantilever or the substrate, or a less characterized specific interaction of the fragment of VAR2CSA with long side chains contained in passivated or functionalized surfaces. Therefore, establishing a standard for measurements is critical and has to be repeated for all measurements in order to obtain the unbiased force measurements of specific protein-protein interactions.

Using Albumin fraction IV or ovalbumin to passivate a surface is common practice in many biologically related tests as it is inert against a multitude of proteins and is able to resorb easily on glass or plastic. It forms a relatively uniform layer, coating the surface and effectively blocking interaction between the material and the added proteins (e.g. Western Blots, ELISA). Increasing the interaction time between coated cantilever and surface from 0 to 250 ms increased the adhesion rate dramatically. This increase indicates that the interaction between VAR2CSA and albumin is stronger than anticipated and is dependent on the loading rate. It is conceivable that VAR2CSA also interacts with albumin molecules; as ovalbumin contains glycoproteins, similar but not identical to CSA structure, and that these are recognized by VAR2CSA, binding promiscuously to sulfurylated glycoproteins is a possible scenario. The group of Salanti *et al.* [32, 60] argued that VAR2CSA interacts with a variety of proteoglycans albeit with lower affinity that CSA. Therefore, valuable and representative data for the specific interaction between CSA and VAR2CSA cannot be mined when using albumin as a negative control, as the recorded adhesion frequency and forces are similar.

We received the recombinant fragment of VAR2CSA that includes regions DBL-1 and DBL-2 that showed the highest affinity to CSA when tested in SPR experiments [60]. This fragment was produced recombinantly in insect cells and contained a “spy” moiety that specifically adheres to a spycatcher moiety, ensuring that the fragment is available in its entirety and correctly oriented. This allows for the optimal interaction between the receptor and respective functionalized or passivated surfaces. While the protein fragment of the receptor remains intact, our method of immobilization on the cantilever had to be optimized and might hinder the specific attachment of the spy-spycatcher molecules in a desirable orientation. While measurements with biotin-streptavidin where successful as a positive control (Section 3.2.4), spycatcher and spy-tagged surfaces did not yield any measurable forces. This could be due to their interaction forces being lower that the limit of detection for the AFM or a result of a malorientation of substrate VAR2CSA-spy moiety, making it inaccessible to the spycatcher moiety.

On the other hand, one also has to consider the effect of CSA presentation during AFM measurements. All experiments were performed with CSA diluted in PBS and allowed to form a layer stochastically. Minimizing the incubation time as well as the protein concentration on both substrate and tip seemed to improve my measurements. The formation of a multi-layer of amorphous CSA chains for longer incubation times or higher concentrations is a very likely possibility and can be somewhat lessened by shortening the incubation time and optimizing protein concentration. The formation of a multilayer could prevent the free interaction with CSA chains as correct orientation and presentation could be difficult to achieve. A good comparison is the formation of a BSA-multilayer that is commonly used to passivate surfaces in biological experiments and is non-reactive towards most biological samples. It is possible that even after forming a single layer of CSA, the interaction does not occur due to steric hinderance between interaction partners. To circumvent this issue, one could choose to use dextran, a protein containing CSA side chains that allows the upright presentation of CSA. However, use of this substrate also introduces other proteins in the system and a specific or non-specific interaction with a different part of the compound cannot be excluded.

Due to repeated exposure between ligand and receptor, one cannot exclude saturation of the interaction pair over time, as it is an inherent flaw of the method (Section 3.2.5).

It is rather an anticipated effect that limits the use of a single cantilever and tip over extended amounts of time. An increase in binding probability over time could be therefore attributed to saturation of interaction partners on either side. It is also likely that CSA chains that are only physiologically resorbed on the surface and not chemically crosslinked, are taken up by the cantilever during retraction. This can be due to a specific bond or mechanical force, lifting these chains and removing them from the substrate. This makes interpretation of the force profile more difficult over time as the non-specific interactions are not distinguishable from the forces of specific binding and unbinding events occurring possibly at the same time during retraction. Therefore, distinguishing between force of detachment between protein interaction partners (VAR2CSA-CSA), detachment of CSA chains from the surface due to a specific interaction or a forceful non-specific detachment caused mechanically by the cantilever indentation and subsequent retraction was not possible for this setup.

4.2.1 Conclusion and future experiments

Despite the technical difficulties, there are two main points to argue for the results obtained when considering the proteins and the interactions *in vivo*. This system simplified to measure single molecule interactions is differing from the naturally occurring proteins in two aspects: length of protein and structure. VAR2CSA cannot be produced easily with classic methods for recombinant proteins and is rather rare to obtain in its full length recombinantly.

Following recent publications and the resolved structure of VAR2CSA, the formation of a pocket by the full-length protein is crucial to facilitate CSA binding [55, 56, 59]. This pocket formation is most-likely not occurring in our setup, as the protein fragment was produced recombinantly. While the DBL2-domain is still believed to be the main interaction partner between VAR2CSA and CSA, the specific structure as well as charge of the protein plays a vital part to facilitate binding [55, 59]. Mutations that change the charge or fold seem to abolish binding almost completely, highlighting their importance during interaction. Based on current sentience, it is possible that VAR2CSA undergoes several post-translational modifications that are not facilitated in the expression system used for the fragment used. Post-translational modifications can greatly affect both the charge and the structure of a region of a protein and there is very little known about these changes in most PfEMP1 proteins. Therefore, a more common practise is to not use the recombinant protein but rather an infected erythrocyte with a specific PfEMP1 expression profile.

4.3 Aim 3: Rosette position in flow

In this study I have shown that rosette clusters have a significantly reduced ability to marginate to the walls of blood vessels compared to single infected erythrocytes. At low flow rates and various haematocrit values (non-physiological, intermediate and physiological [210, 211]), I observed that regardless of number of cells forming these clusters, rosettes will remain in flow away from the walls of a narrow channel. That leads to the conclusion that rosetting is not occurring to instigate Pf-infected erythrocyte sequestration through margination and rosettes do not disassemble in higher haematocrit or due to increased sheer rate.

Interestingly, there are several forces at interplay that would increase or decrease marginalization. The size and stiffness can affect the position of a cell or cluster in a flow channel as well as lift forces and gravity [212, 213]. Due to its size and the presence of a stiff, infected erythrocyte in the rosette cluster, one could anticipate margination and disassociation of the uninfected erythrocytes and initiation of the cytoadhesion procedure. The results display that this was not the case. Stiffer cells tend to marginate better as is evident by *Pf*-infected erythrocytes and leucocytes [212]. This enables adhesin interaction that results in sequestration or dynamic adhesion onto the endothelial wall of blood vessels. This process seems to be crucial for parasite survival and leucocyte activation. However, observing rosettes led to the surprising conclusion that they do not marginate to vessel walls. One could argue that this phenomenon is due to the fact that the stiffer *Pf*-infected cell is surrounded by softer, more elastic uninfected erythrocytes that do not marginate and remain in the centre of the flow. Uninfected erythrocytes should not show great margination tendencies and only marginate due to displacement in a higher haematocrit value.

At low, non-physiologically relevant haematocrit (7.5 %) rosettes seem to be more equally distributed in the channel, however rarely marginating to the wall of the narrow chamber. Increasing the number of surrounding erythrocytes seems to have the opposite effect than expected, with the rosette maintaining their position near the centre of the flow. Larger rosettes also show an increased tendency to remain close to the centre of the channel and are much less likely to marginate. If observed strictly from the standpoint of rheology and aspiration of cells through a narrow channel, the initial position of the rosette can be explained through lift forces that despite the size of the rosette, push the cluster of flexible cells to the centre of flow and away from the walls. If only the size of the rosette is considered, gravity would most probably be the ruling force, leading the rosette to marginate. However, observing rosettes in a narrow flow chamber showed that this is not the case. A plausible explanation for this phenomenon is that larger more flexible objects are more likely to maintain momentum in flow and are subject to larger lift forces, placing them in the centre of flow and away from the walls.

It seems that within the channel there is a tendency for the rosette to move out of the centre of flow (0.5 mm) and while not marginating, preferring the intermediate position between the centre of flow and the wall of the channel. If one considers classic wall sheer stress (WSS) in a rectangular chamber, these positions also correspond to a lower shear stress value, reducing from the centre towards the walls. It was interesting to observe that rosettes in low haematocrits were mostly found within those positions.

Another interesting phenomenon that I was able to observe was the dissociation of large rosettes in 40 % haematocrit, and the presence of solely rosettes with small coordination number of uninfected erythrocytes. This phenomenon could have two possible explanations. On the one hand, one could argue that if rosettes benefit from the elastic properties of attached uninfected erythrocytes, rosette formation could be more beneficial with less stiff cells [214]. It can be assumed that larger rosette clusters contain more than one *Pf*-infected erythrocyte and are therefore stiffer. Dissociating into smaller, more flexible clusters allows the rosette to remain in the centre of flow and not to marginate in higher haematocrit values. This, however, would contradict the long standing hypothesis that rosettes form to obstruct vascular perfusion and therefore, the larger clusters would be more effective [215, 216]. A different approach to the dissociation phenomenon could be that there is a greater chance of exchange between the rosette-attached erythrocytes and the surrounding single uninfected erythrocytes.

Based on the platform used in these experiments, cell membranes are dyed with a common lipophilic fluorophore that is integrated into the membrane of erythrocytes that form a rosette. This dye is integrated into the lipid rafts of the erythrocyte membrane and could result in a slight increase in the stiffness due to this integration. This might trigger the infected erythrocyte to sense this change and lead to its release from a stiffer, attached cell, resulting in a smaller rosette. It is also plausible that the cell is replaced with the attachment of a more flexible, non-dyed uninfected erythrocyte that cannot be seen using the current microscopy setup.

One must consider not only effect but also the cause of this phenotype and it is intriguing to think about the benefit of such a phenomenon to the parasite. Initially it was thought plausible that rosettes are formed in order to lead to margination of the infected erythrocyte faster and its subsequent sequestration onto the endothelium. A larger cluster of cells could form to counter lift forces and enable margination to initiate sequestration, leading to benefits discussed for Aim 1. However, this was not the case and I observed the opposite trend in intermediate and low haematocrit values. Taking into account all measurements performed, margination does not seem to be a driving factor for rosette formation.

Considering the results of our microfluidic channel measurements as well as cell culture, rosettes appear to form stochastically for *Plasmodium falciparum* [217]. The phenotype itself has to be subjected to frequent selection to increase rosetting frequency. It was not yet possible to record the formation of a rosette and attempts to reconstruct a rosette with the help of optical tweezers did not yield a satisfactory result. Uninfected erythrocytes that were forcefully detached form the infected cell did not reattach within the timepoint of the experiment even when brought in close proximity.

The use of anti-rosetting agents, such as heparin and fucoidan, permanently disrupts rosettes and this appears to have similar effects than receptor-specific antibodies [66, 216]. Therefore, it is not possible to conclude the reasoning for rosette formation by triggering disruption, since these do not appear to form within the same life cycle iteration. It was also possible to determine these facts, by observing disruption of rosettes during MACS isolation, where the yield also included single infected erythrocytes even in cultures with over 90% rosetting frequency.

It has been postulated as a probability that rosettes form to shield the infected erythrocyte in flow from detection by the immune system [62, 219]. My results add to this assumption that there is an added benefit to the parasite by forming rosettes, in that not only is it shielded by uninfected erythrocytes, it also gains properties closer to healthy erythrocytes that enable them to stay in circulation for longer.

Another possibility for rosette formation is the closer proximity of potential targets for invasion by merozoites [219, 220]. When one considers a non-pathological haematocrit, this does not seem likely as erythrocytes are abundant and in quite close proximity [221]. Furthermore, the velocity of merozoites enable it to invade erythrocytes that are not close by, albeit increasing exposure time to other elements of whole blood and probability of detection by the immune system components [219, 221].

While less probable, it could be a reasoning for the non-margination of rosettes, as healthy erythrocytes are forming a cell-free zone close to the walls of blood vessels. Therefore, by remaining in the centre of the blood vessel or away from the walls, the parasite increases chances of successful invasion by increasing the radius that released merozoites could travel after maturation. This is however, less likely if one considers the structure of rosettes even in schizont stage infected erythrocytes, with large areas of the infected cells still covered by attached uninfected erythrocytes. These closed structures were also seen in flow and under sheer stress conditions.

4.3.1 Conclusion and future experiments

The rosetting phenotype has been linked to severe malaria and is seen in all four *Plasmodium* species. In this study, I have shown that regardless of haematocrit values and rosette size, these cells will not marginate towards the walls of the channel. This conclusion argues against the hypothesis of a rosette forming in order to contribute to parasite sequestration as seen in single infected erythrocytes. Experiments in various haematocrits highlight the importance of measurements performed in near-physiological conditions and provide new information about rosette formation and behaviour in flow. Due to its simplicity, this setup can be employed easily with little optimization to further characterize the rosetting phenotype.

It might be interesting to observe the effect of anti-rosetting agents or anti-malarial drugs on rosette integrity and rheological behaviour employing this setup. Perhaps the only improvement to our setup would be the elasticity and shape of the channel. If one would opt for a different microscopy technique such as 2D photon, using a softer material such as a hydrogel within a tube would bring the measurements even closer to in vivo conditions. Varying the diameter of the tubing would also allow for approximation of circulation in the microvasculatory system and provide further evidence of rosette formation and behaviour in flow.

Literature

1. *World Malaria report 2021* 2021, World Health Organization.
2. Alan F. Cowman; Julie Healer, D.M., Kevin Marsh, *Malaria: Biology and Disease.* Cell, 2016. **167**(3): p. 610-624.
3. *World Malaria Report 2016*. 2016, World Health Organization
4. von Seidlein, L., et al., *Predicting the clinical outcome of severe falciparum malaria in african children: findings from a large randomized trial.* Clin Infect Dis, 2012. **54**(8): p. 1080-90.
5. Phillips, M.A., et al., *Malaria.* Nat Rev Dis Primers, 2017. **3**: p. 17050.
6. Fowkes, F.J., P. Boeuf, and J.G. Beeson, *Immunity to malaria in an era of declining malaria transmission.* Parasitology, 2016. **143**(2): p. 139-53.
7. Weiss, D.J., et al., *Mapping the global prevalence, incidence, and mortality of Plasmodium falciparum, 2000-17: a spatial and temporal modelling study.* Lancet, 2019. **394**(10195): p. 322-331.
8. Amino, R., et al., *Quantitative imaging of Plasmodium transmission from mosquito to mammal.* Nat Med, 2006. **12**(2): p. 220-4.
9. Battista, A., F. Frischknecht, and U.S. Schwarz, *Geometrical model for malaria parasite migration in structured environments.* Phys Rev E Stat Nonlin Soft Matter Phys, 2014. **90**(4): p. 042720.
10. Valenciano, A.L., et al., *In vitro models for human malaria: targeting the liver stage.* Trends Parasitol, 2022. **38**(9): p. 758-774.
11. Lindner, S.E., J.L. Miller, and S.H. Kappe, *Malaria parasite pre-erythrocytic infection: preparation meets opportunity.* Cell Microbiol, 2012. **14**(3): p. 316-24.
12. Maier, A.G., et al., *Plasmodium falciparum.* Trends Parasitol, 2019. **35**(6): p. 481-482.
13. Hopp, C.S., et al., *Longitudinal analysis of Plasmodium sporozoite motility in the dermis reveals component of blood vessel recognition.* Elife, 2015. **4**.
14. Smith, J.D., *The role of PfEMP1 adhesion domain classification in Plasmodium falciparum pathogenesis research.* Mol Biochem Parasitol, 2014. **195**(2): p. 82-7.
15. Pino, P., et al., *Plasmodium falciparum--infected erythrocyte adhesion induces caspase activation and apoptosis in human endothelial cells.* J Infect Dis, 2003. **187**(8): p. 1283-90.
16. Yeo, T.W., et al., *Impaired nitric oxide bioavailability and L-arginine reversible endothelial dysfunction in adults with falciparum malaria.* J Exp Med, 2007. **204**(11): p. 2693-704.
17. Weinberg, J.B., et al., *Arginine, nitric oxide, carbon monoxide, and endothelial function in severe malaria.* Curr Opin Infect Dis, 2008. **21**(5): p. 468-75.
18. Wilson, N.O., et al., *Soluble factors from Plasmodium falciparum-infected erythrocytes induce apoptosis in human brain vascular endothelial and neuroglia cells.* Mol Biochem Parasitol, 2008. **162**(2): p. 172-6.
19. Adams, S., H. Brown, and G. Turner, *Breaking down the blood-brain barrier: signaling a path to cerebral malaria?* Trends Parasitol, 2002. **18**(8): p. 360-6.
20. Adams, S., et al., *Differential binding of clonal variants of Plasmodium falciparum to allelic forms of intracellular adhesion molecule 1 determined by flow adhesion assay.* Infect Immun, 2000. **68**(1): p. 264-9.
21. Francischetti, I.M., et al., *Plasmodium falciparum-infected erythrocytes induce tissue factor expression in endothelial cells and support the assembly of multimolecular coagulation complexes.* J Thromb Haemost, 2007. **5**(1): p. 155-65.
22. Tripathi, A.K., D.J. Sullivan, and M.F. Stins, *Plasmodium falciparum-infected erythrocytes decrease the integrity of human blood-brain barrier endothelial cell monolayers.* J Infect Dis, 2007. **195**(7): p. 942-50.
23. Jambou, R., et al., *Plasmodium falciparum adhesion on human brain microvascular endothelial cells involves transmigration-like cup formation and induces opening of intercellular junctions.* PLoS Pathog, 2010. **6**(7): p. e1001021.
24. Brown, H., et al., *Evidence of blood-brain barrier dysfunction in human cerebral malaria.* Neuropathol Appl Neurobiol, 1999. **25**(4): p. 331-40.

25. Brown, H.C., et al., *Blood-brain barrier function in cerebral malaria and CNS infections in Vietnam.* Neurology, 2000. **55**(1): p. 104-11.
26. Storm, J., et al., *Cerebral malaria is associated with differential cytoadherence to brain endothelial cells.* EMBO Mol Med, 2019. **11**(2).
27. Shaffer, N., et al., *Tumor necrosis factor and severe malaria.* J Infect Dis, 1991. **163**(1): p. 96-101.
28. Miller, L.H., et al., *The pathogenic basis of malaria.* Nature, 2002. **415**(6872): p. 673-9.
29. Scherf, A., et al., *Antigenic variation in malaria: in situ switching, relaxed and mutually exclusive transcription of var genes during intra-erythrocytic development in Plasmodium falciparum.* Embo j, 1998. **17**(18): p. 5418-26.
30. Kyes, S., P. Horrocks, and C. Newbold, *Antigenic variation at the infected red cell surface in malaria.* Annu Rev Microbiol, 2001. **55**: p. 673-707.
31. Pasternak, N.D., Dzikowski, Ron, *PfEMP1: An antigen that plays a key role in the pathogenicity and immune evasion of the malaria parasite Plasmodium falciparum.* The International Journal of Biochemistry & Cell Biology, 2009. **41**(7): p. 1463-1466.
32. Andersen, P., et al., *Structural Insight into Epitopes in the Pregnancy-Associated Malaria Protein VAR2CSA.* PLoS pathogens, 2008. **4**: p. e42.
33. Kraemer, S.M. and J.D. Smith, *Evidence for the importance of genetic structuring to the structural and functional specialization of the Plasmodium falciparum var gene family.* Mol Microbiol, 2003. **50**(5): p. 1527-38.
34. Voss, T.S., et al., *Genomic distribution and functional characterisation of two distinct and conserved Plasmodium falciparum var gene 5' flanking sequences.* Mol Biochem Parasitol, 2000. **107**(1): p. 103-15.
35. Kyes, S.A., S.M. Kraemer, and J.D. Smith, *Antigenic variation in Plasmodium falciparum: gene organization and regulation of the var multigene family.* Eukaryot Cell, 2007. **6**(9): p. 1511-20.
36. Lavstsen, T., et al., *Sub-grouping of Plasmodium falciparum 3D7 var genes based on sequence analysis of coding and non-coding regions.* Malar J, 2003. **2**: p. 27.
37. Jiang, L., et al., *PfSETvs methylation of histone H3K36 represses virulence genes in Plasmodium falciparum.* Nature, 2013. **499**(7457): p. 223-7.
38. Smith, J.D., et al., *Decoding the language of var genes and Plasmodium falciparum sequestration.* Trends Parasitol, 2001. **17**(11): p. 538-45.
39. Rask, T.S., et al. *Plasmodium falciparum erythrocyte membrane protein 1 diversity in seven genomes--divide and conquer*. PLoS computational biology, 2010. **6**, DOI: 10.1371/journal.pcbi.1000933.
40. Lavstsen, T., et al., *Plasmodium falciparum erythrocyte membrane protein 1 domain cassettes 8 and 13 are associated with severe malaria in children.* Proc Natl Acad Sci U S A, 2012. **109**(26): p. E1791-800.
41. Hiller, N.L., et al., *A host-targeting signal in virulence proteins reveals a secretome in malarial infection.* Science, 2004. **306**(5703): p. 1934-7.
42. Gardner, M.J., et al., *Genome sequence of the human malaria parasite Plasmodium falciparum.* Nature, 2002. **419**(6906): p. 498-511.
43. Kraemer, S.M., et al., *Patterns of gene recombination shape var gene repertoires in Plasmodium falciparum: comparisons of geographically diverse isolates.* BMC Genomics, 2007. **8**: p. 45.
44. Smith, J.D., et al., *Classification of adhesive domains in the Plasmodium falciparum erythrocyte membrane protein 1 family.* Mol Biochem Parasitol, 2000. **110**(2): p. 293-310.
45. Robinson, B.A., T.L. Welch, and J.D. Smith, *Widespread functional specialization of Plasmodium falciparum erythrocyte membrane protein 1 family members to bind CD36 analysed across a parasite genome.* Mol Microbiol, 2003. **47**(5): p. 1265-78.
46. Wu, Y., et al., *Amplification of P. falciparum Cytoadherence through induction of a pro-adhesive state in host endothelium.* PLoS One, 2011. **6**(10): p. e24784.

47. Higgins, M.K., *The structure of a chondroitin sulfate-binding domain important in placental malaria.* J Biol Chem, 2008. **283**(32): p. 21842-6.
48. Jespersen, J.S., et al., *Plasmodium falciparum var genes expressed in children with severe malaria encode CIDRα1 domains.* EMBO Mol Med, 2016. **8**(8): p. 839-50.
49. Kaestli, M., et al., *Virulence of malaria is associated with differential expression of Plasmodium falciparum var gene subgroups in a case-control study.* J Infect Dis, 2006. **193**(11): p. 1567-74.
50. Goyal, A., S. Goel, and D.C. Gowda, *Plasmodium falciparum: Assessment of parasite-infected red blood cell binding to placental chondroitin proteoglycan and bovine tracheal chondroitin sulfate A.* Exp Parasitol, 2009. **123**(2): p. 105-10.
51. Nunes, M.C. and A. Scherf, *Plasmodium falciparum during pregnancy: a puzzling parasite tissue adhesion tropism.* Parasitology, 2007. **134**(Pt 13): p. 1863-9.
52. Fried, M. and P.E. Duffy, *Adherence of Plasmodium falciparum to chondroitin sulfate A in the human placenta.* Science, 1996. **272**(5267): p. 1502-4.
53. Avril, M., et al., *Evidence for globally shared, cross-reacting polymorphic epitopes in the pregnancy-associated malaria vaccine candidate VAR2CSA.* Infect Immun, 2008. **76**(4): p. 1791-800.
54. Sander, A.F., et al., *Multiple var2csa-type PfEMP1 genes located at different chromosomal loci occur in many Plasmodium falciparum isolates.* PLoS One, 2009. **4**(8): p. e6667.
55. Wang, K., et al., *Cryo-EM reveals the architecture of placental malaria VAR2CSA and provides molecular insight into chondroitin sulfate binding.* Nat Commun, 2021. **12**(1): p. 2956.
56. Doritchamou, J.Y.A., et al., *A single full-length VAR2CSA ectodomain variant purifies broadly neutralizing antibodies against placental malaria isolates.* Elife, 2022. **11**.
57. Hviid, L. and A.T. Jensen, *PfEMP1 - A Parasite Protein Family of Key Importance in Plasmodium falciparum Malaria Immunity and Pathogenesis.* Adv Parasitol, 2015. **88**: p. 51-84.
58. Dorin-Semblat, D., et al., *Phosphorylation of the VAR2CSA extracellular region is associated with enhanced adhesive properties to the placental receptor CSA.* PLoS biology, 2019. **17**(6): p. e3000308-e3000308.
59. Ma, R., et al., *Structural basis for placental malaria mediated by Plasmodium falciparum VAR2CSA.* Nat Microbiol, 2021. **6**(3): p. 380-391.
60. Clausen, T.M., et al., *Structural and functional insight into how the Plasmodium falciparum VAR2CSA protein mediates binding to chondroitin sulfate A in placental malaria.* J Biol Chem, 2012. **287**(28): p. 23332-45.
61. Rowe, J.A., et al., *P. falciparum rosetting mediated by a parasite-variant erythrocyte membrane protein and complement-receptor 1.* Nature, 1997. **388**(6639): p. 292-5.
62. Wahlgren, M., et al., *Why do Plasmodium falciparumm-infected erythrocytes form spontaneous erythrocyte rosettes?* Parasitol Today, 1989. **5**(6): p. 183-5.
63. Doumbo, O.K., et al., *High levels of Plasmodium falciparum rosetting in all clinical forms of severe malaria in African children.* Am J Trop Med Hyg, 2009. **81**(6): p. 987-93.
64. Lowe, B.S., M. Mosobo, and P.C. Bull, *All four species of human malaria parasites form rosettes.* Trans R Soc Trop Med Hyg, 1998. **92**(5): p. 526.
65. Udomsanpetch, R., et al., *Rosette formation by Plasmodium vivax.* Trans R Soc Trop Med Hyg, 1995. **89**(6): p. 635-7.
66. Carlson, J., et al., *Human cerebral malaria: association with erythrocyte rosetting and lack of anti-rosetting antibodies.* Lancet, 1990. **336**(8729): p. 1457-60.
67. Cockburn, I.A., et al., *A simple method for accurate quantification of complement receptor 1 on erythrocytes preserved by fixing or freezing.* J Immunol Methods, 2002. **271**(1-2): p. 59-64.
68. Niang, M., et al., *STEVOR is a Plasmodium falciparum erythrocyte binding protein that mediates merozoite invasion and rosetting.* Cell Host Microbe, 2014. **16**(1): p. 81-93.
69. Goel, S., et al., *RIFINs are adhesins implicated in severe Plasmodium falciparum malaria.* Nat Med, 2015. **21**(4): p. 314-7.

70. Claessens, A., et al., *Design of a variant surface antigen-supplemented microarray chip for whole transcriptome analysis of multiple Plasmodium falciparum cytoadherent strains, and identification of strain-transcendent rif and stevor genes.* Malar J, 2011. **10**: p. 180.
71. Carlton, J.M., et al., *Comparative genomics of the neglected human malaria parasite Plasmodium vivax.* Nature, 2008. **455**(7214): p. 757-63.
72. Janssen, C.S., et al., *Plasmodium interspersed repeats: the major multigene superfamily of malaria parasites.* Nucleic Acids Res, 2004. **32**(19): p. 5712-20.
73. Pain, A., et al., *The genome of the simian and human malaria parasite Plasmodium knowlesi.* Nature, 2008. **455**(7214): p. 799-803.
74. Fernandez, V., et al., *Small, clonally variant antigens expressed on the surface of the Plasmodium falciparum-infected erythrocyte are encoded by the rif gene family and are the target of human immune responses.* J Exp Med, 1999. **190**(10): p. 1393-404.
75. Kyes, S.A., et al., *Rifins: a second family of clonally variant proteins expressed on the surface of red cells infected with Plasmodium falciparum.* Proc Natl Acad Sci U S A, 1999. **96**(16): p. 9333-8.
76. Petter, M., et al., *Variant proteins of the Plasmodium falciparum RIFIN family show distinct subcellular localization and developmental expression patterns.* Mol Biochem Parasitol, 2007. **156**(1): p. 51-61.
77. Christian W. Wang, L.H., *Rifins, rosetting, and red blood cells.* Trends in Parasitology, 2015. **31**(7): p. 285-286.
78. Blythe, J.E., et al., *Plasmodium falciparum STEVOR proteins are highly expressed in patient isolates and located in the surface membranes of infected red blood cells and the apical tips of merozoites.* Infect Immun, 2008. **76**(7): p. 3329-36.
79. Khattab, A. and S. Meri, *Exposure of the Plasmodium falciparum clonally variant STEVOR proteins on the merozoite surface.* Malar J, 2011. **10**: p. 58.
80. McRobert, L., et al., *Distinct trafficking and localization of STEVOR proteins in three stages of the Plasmodium falciparum life cycle.* Infect Immun, 2004. **72**(11): p. 6597-602.
81. Blythe, J.E., T. Surentheran, and P.R. Preiser, *STEVOR--a multifunctional protein?* Mol Biochem Parasitol, 2004. **134**(1): p. 11-5.
82. Sanyal, S., et al., *Plasmodium falciparum STEVOR proteins impact erythrocyte mechanical properties.* Blood, 2012. **119**(2): p. e1-8.
83. Gruenberg, J., D.R. Allred, and I.W. Sherman, *Scanning electron microscope-analysis of the protrusions (knobs) present on the surface of Plasmodium falciparum-infected erythrocytes.* J Cell Biol, 1983. **97**(3): p. 795-802.
84. Quadt, K.A., et al., *The density of knobs on Plasmodium falciparum-infected erythrocytes depends on developmental age and varies among isolates.* PLoS One, 2012. **7**(9): p. e45658.
85. McMillan, P.J., et al., *Spatial and temporal mapping of the PfEMP1 export pathway in Plasmodium falciparum.* Cell Microbiol, 2013. **15**(8): p. 1401-18.
86. Pologe, L.G. and J.V. Ravetch, *A chromosomal rearrangement in a P. falciparum histidine-rich protein gene is associated with the knobless phenotype.* Nature, 1986. **322**(6078): p. 474-7.
87. Sanchez, C.P., et al., *Single-molecule imaging and quantification of the immune-variant adhesin VAR2CSA on knobs of Plasmodium falciparum-infected erythrocytes.* Communications biology, 2019. **2**: p. 172-172.
88. Watermeyer, J.M., et al., *A spiral scaffold underlies cytoadherent knobs in Plasmodium falciparum-infected erythrocytes.* Blood, 2016. **127**(3): p. 343-51.
89. Cooke, B.M., et al., *Assignment of functional roles to parasite proteins in malaria-infected red blood cells by competitive flow-based adhesion assay.* Br J Haematol, 2002. **117**(1): p. 203-11.
90. Cutts, E.E., et al., *Structural analysis of P. falciparum KAHRP and PfEMP1 complexes with host erythrocyte spectrin suggests a model for cytoadherent knob protrusions.* PLoS Pathog, 2017. **13**(8): p. e1006552.

91. Magowan, C., et al., *Plasmodium falciparum histidine-rich protein 1 associates with the band 3 binding domain of ankyrin in the infected red cell membrane.* Biochim Biophys Acta, 2000. **1502**(3): p. 461-70.
92. Oh, S.S., et al., *Plasmodium falciparum erythrocyte membrane protein 1 is anchored to the actin-spectrin junction and knob-associated histidine-rich protein in the erythrocyte skeleton.* Mol Biochem Parasitol, 2000. **108**(2): p. 237-47.
93. Maier, A.G., et al., *Exported proteins required for virulence and rigidity of Plasmodium falciparum-infected human erythrocytes.* Cell, 2008. **134**(1): p. 48-61.
94. Subramani, R., et al., *Plasmodium falciparum-infected erythrocyte knob density is linked to the PfEMP1 variant expressed.* mBio, 2015. **6**(5): p. e01456-15.
95. McHugh, E., et al., *Role of Plasmodium falciparum Protein GEXP07 in Maurer's Cleft Morphology, Knob Architecture, and P. falciparum EMP1 Trafficking.* mBio, 2020. **11**(2).
96. Carmo, O.M.S., et al., *Deletion of the Plasmodium falciparum exported protein PTP7 leads to Maurer's clefts vesiculation, host cell remodeling defects, and loss of surface presentation of EMP1.* PLoS Pathog, 2022. **18**(8): p. e1009882.
97. Diehl, M., et al., *Co-chaperone involvement in knob biogenesis implicates host-derived chaperones in malaria virulence.* PLoS Pathog, 2021. **17**(10): p. e1009969.
98. Chakravorty, S.J. and A. Craig, *The role of ICAM-1 in Plasmodium falciparum cytoadherence.* Eur J Cell Biol, 2005. **84**(1): p. 15-27.
99. Yang, Y., et al., *Structural basis for dimerization of ICAM-1 on the cell surface.* Mol Cell, 2004. **14**(2): p. 269-76.
100. Turner, G.D., et al., *An immunohistochemical study of the pathology of fatal malaria. Evidence for widespread endothelial activation and a potential role for intercellular adhesion molecule-1 in cerebral sequestration.* Am J Pathol, 1994. **145**(5): p. 1057-69.
101. Elhassan, I.M., et al., *Evidence of endothelial inflammation, T cell activation, and T cell reallocation in uncomplicated Plasmodium falciparum malaria.* Am J Trop Med Hyg, 1994. **51**(3): p. 372-9.
102. Lansche, C., et al., *The sickle cell trait affects contact dynamics and endothelial cell activation in Plasmodium falciparum-infected erythrocytes.* Communications Biology, 2018. **1**(1): p. 211.
103. Tripathi, A.K., et al., *Plasmodium falciparum-infected erythrocytes induce NF-kappaB regulated inflammatory pathways in human cerebral endothelium.* Blood, 2009. **114**(19): p. 4243-52.
104. Clark, I.A., et al., *Induction of HO-1 in tissue macrophages and monocytes in fatal falciparum malaria and sepsis.* Malar J, 2003. **2**(1): p. 41.
105. Bengtsson, A., et al., *A novel domain cassette identifies Plasmodium falciparum PfEMP1 proteins binding ICAM-1 and is a target of cross-reactive, adhesion-inhibitory antibodies.* J Immunol, 2013. **190**(1): p. 240-9.
106. Olsen, R.W., et al., *Natural and Vaccine-Induced Acquisition of Cross-Reactive IgG-Inhibiting ICAM-1-Specific Binding of a Plasmodium falciparum PfEMP1 Subtype Associated Specifically with Cerebral Malaria.* Infect Immun, 2018. **86**(4).
107. Jun, C.D., et al., *Ultrastructure and function of dimeric, soluble intercellular adhesion molecule-1 (ICAM-1).* J Biol Chem, 2001. **276**(31): p. 29019-27.
108. Avril, M., et al., *A restricted subset of var genes mediates adherence of Plasmodium falciparum-infected erythrocytes to brain endothelial cells.* Proc Natl Acad Sci U S A, 2012. **109**(26): p. E1782-90.
109. Claessens, A., et al., *A subset of group A-like var genes encodes the malaria parasite ligands for binding to human brain endothelial cells.* Proc Natl Acad Sci U S A, 2012. **109**(26): p. E1772-81.
110. Fernandez-Reyes, D., et al., *A high frequency African coding polymorphism in the N-terminal domain of ICAM-1 predisposing to cerebral malaria in Kenya.* Hum Mol Genet, 1997. **6**(8): p. 1357-60.

111. Bellamy, R., D. Kwiatkowski, and A.V. Hill, *Absence of an association between intercellular adhesion molecule 1, complement receptor 1 and interleukin 1 receptor antagonist gene polymorphisms and severe malaria in a West African population.* Trans R Soc Trop Med Hyg, 1998. **92**(3): p. 312-6.
112. Kun, J.F., et al., *Association of the ICAM-1Kilifi mutation with protection against severe malaria in Lambaréné, Gabon.* Am J Trop Med Hyg, 1999. **61**(5): p. 776-9.
113. Ohashi, J., et al., *Absence of association between the allele coding methionine at position 29 in the N-terminal domain of ICAM-1 (ICAM-1(Kilifi)) and severe malaria in the northwest of Thailand.* Jpn J Infect Dis, 2001. **54**(3): p. 114-6.
114. Lennartz, F., et al., *Structural insights into diverse modes of ICAM-1 binding by Plasmodium falciparum-infected erythrocytes.* 2019. **116**(40): p. 20124-20134.
115. Barnwell, J.W., et al., *A human 88-kD membrane glycoprotein (CD36) functions in vitro as a receptor for a cytoadherence ligand on Plasmodium falciparum-infected erythrocytes.* J Clin Invest, 1989. **84**(3): p. 765-72.
116. Howell, D.P., et al., *Mapping a common interaction site used by Plasmodium falciparum Duffy binding-like domains to bind diverse host receptors.* Mol Microbiol, 2008. **67**(1): p. 78-87.
117. Beeson, J.G., et al., *Plasmodium falciparum isolates from infected pregnant women and children are associated with distinct adhesive and antigenic properties.* J Infect Dis, 1999. **180**(2): p. 464-72.
118. Barber, N.M., et al., *Structure-Guided Design of a Synthetic Mimic of an Endothelial Protein C Receptor-Binding PfEMP1 Protein.* mSphere, 2021. **6**(1).
119. Jensen, A.R., Y. Adams, and L. Hviid, *Cerebral Plasmodium falciparum malaria: The role of PfEMP1 in its pathogenesis and immunity, and PfEMP1-based vaccines to prevent it.* Immunological reviews, 2020. **293**(1): p. 230-252.
120. Mkumbaye, S.I., et al., *The Severity of Plasmodium falciparum Infection Is Associated with Transcript Levels of var Genes Encoding Endothelial Protein C Receptor-Binding P. falciparum Erythrocyte Membrane Protein 1.* Infect Immun, 2017. **85**(4).
121. Semblat, J.P., et al., *Identification of the minimal binding region of a Plasmodium falciparum IgM binding PfEMP1 domain.* Mol Biochem Parasitol, 2015. **201**(1): p. 76-82.
122. Gleeson, E.M., J.S. O'Donnell, and R.J. Preston, *The endothelial cell protein C receptor: cell surface conductor of cytoprotective coagulation factor signaling.* Cell Mol Life Sci, 2012. **69**(5): p. 717-26.
123. Turner, L., et al., *Severe malaria is associated with parasite binding to endothelial protein C receptor.* Nature, 2013. **498**(7455): p. 502-5.
124. Baruch, D.I., et al., *Plasmodium falciparum erythrocyte membrane protein 1 is a parasitized erythrocyte receptor for adherence to CD36, thrombospondin, and intercellular adhesion molecule 1.* Proc Natl Acad Sci U S A, 1996. **93**(8): p. 3497-502.
125. Metwally, N.G., et al., *Characterisation of Plasmodium falciparum populations selected on the human endothelial receptors P-selectin, E-selectin, CD9 and CD151.* Sci Rep, 2017. **7**(1): p. 4069.
126. Berger, S.S., et al., *Plasmodium falciparum expressing domain cassette 5 type PfEMP1 (DC5-PfEMP1) bind PECAM1.* PLoS One, 2013. **8**(7): p. e69117.
127. Tilly, A.K., et al., *Type of in vitro cultivation influences cytoadhesion, knob structure, protein localization and transcriptome profile of Plasmodium falciparum.* Sci Rep, 2015. **5**: p. 16766.
128. Discher, D.E., N. Mohandas, and E.A. Evans, *Molecular maps of red cell deformation: hidden elasticity and in situ connectivity.* Science, 1994. **266**(5187): p. 1032-5.
129. Lux, S.E.t., *Anatomy of the red cell membrane skeleton: unanswered questions.* Blood, 2016. **127**(2): p. 187-99.
130. Suresh, S., et al., *Connections between single-cell biomechanics and human disease states: gastrointestinal cancer and malaria.* Acta Biomater, 2005. **1**(1): p. 15-30.
131. Diez-Silva, M., et al., *Shape and Biomechanical Characteristics of Human Red Blood Cells in Health and Disease.* MRS Bull, 2010. **35**(5): p. 382-388.

132. Dintenfass, L., *Internal viscosity of the red cell and a blood viscosity equation.* Nature, 1968. **219**(5157): p. 956-8.
133. Mohandas, N. and P.G. Gallagher, *Red cell membrane: past, present, and future.* Blood, 2008. **112**(10): p. 3939-48.
134. Quinn, D.J., et al., *Combined simulation and experimental study of large deformation of red blood cells in microfluidic systems.* Ann Biomed Eng, 2011. **39**(3): p. 1041-50.
135. Li, J., et al., *Spectrin-level modeling of the cytoskeleton and optical tweezers stretching of the erythrocyte.* Biophys J, 2005. **88**(5): p. 3707-19.
136. Tomaiuolo, G. and S. Guido, *Start-up shape dynamics of red blood cells in microcapillary flow.* Microvasc Res, 2011. **82**(1): p. 35-41.
137. Risinger, M. and T.A. Kalfa, *Red cell membrane disorders: structure meets function.* Blood, 2020. **136**(11): p. 1250-1261.
138. Nagel, R.L., M.E. Fabry, and M.H. Steinberg, *The paradox of hemoglobin SC disease.* Blood Rev, 2003. **17**(3): p. 167-78.
139. Nash, G.B., C.S. Johnson, and H.J. Meiselman, *Mechanical properties of oxygenated red blood cells in sickle cell (HbSS) disease.* Blood, 1984. **63**(1): p. 73-82.
140. Chien, S., S. Usami, and J.F. Bertles, *Abnormal rheology of oxygenated blood in sickle cell anemia.* J Clin Invest, 1970. **49**(4): p. 623-34.
141. Silva, D.G.H., et al., *Oxidative stress in sickle cell disease: an overview of erythrocyte redox metabolism and current antioxidant therapeutic strategies.* Free Radic Biol Med, 2013. **65**: p. 1101-1109.
142. Hebbel, R.P., *Beyond hemoglobin polymerization: the red blood cell membrane and sickle disease pathophysiology.* Blood, 1991. **77**(2): p. 214-37.
143. Piel, F.B., et al., *The distribution of haemoglobin C and its prevalence in newborns in Africa.* Sci Rep, 2013. **3**: p. 1671.
144. Chotivanich, K., et al., *Hemoglobin E: a balanced polymorphism protective against high parasitemias and thus severe P falciparum malaria.* Blood, 2002. **100**(4): p. 1172-6.
145. Taylor, S.M., C. Cerami, and R.M. Fairhurst, *Hemoglobinopathies: slicing the Gordian knot of Plasmodium falciparum malaria pathogenesis.* PLoS Pathog, 2013. **9**(5): p. e1003327.
146. Modiano, D., et al., *Haemoglobin C protects against clinical Plasmodium falciparum malaria.* Nature, 2001. **414**(6861): p. 305-8.
147. Aidoo, M., et al., *Protective effects of the sickle cell gene against malaria morbidity and mortality.* Lancet, 2002. **359**(9314): p. 1311-2.
148. Cooke, B.M., N. Mohandas, and R.L. Coppel, *The malaria-infected red blood cell: structural and functional changes.* Adv Parasitol, 2001. **50**: p. 1-86.
149. Thomas, S.L. and V.L. Lew, *Plasmodium falciparum and the permeation pathway of the host red blood cell.* Trends Parasitol, 2004. **20**(3): p. 122-5.
150. Waldecker, M., et al., *Differential time-dependent volumetric and surface area changes and delayed induction of new permeation pathways in P. falciparum-infected hemoglobinopathic erythrocytes.* Cellular Microbiology, 2017. **19**(2).
151. Mauritz, J.M., et al., *The homeostasis of Plasmodium falciparum-infected red blood cells.* PLoS Comput Biol, 2009. **5**(4): p. e1000339.
152. Cranston, H.A., et al., *Plasmodium falciparum maturation abolishes physiologic red cell deformability.* Science, 1984. **223**(4634): p. 400-3.
153. Suwanarusk, R., et al., *The deformability of red blood cells parasitized by Plasmodium falciparum and P. vivax.* J Infect Dis, 2004. **189**(2): p. 190-4.
154. Park, Y., et al., *Refractive index maps and membrane dynamics of human red blood cells parasitized by Plasmodium falciparum.* Proc Natl Acad Sci U S A, 2008. **105**(37): p. 13730-5.
155. Fröhlich, B., et al., *Hemoglobin S and C affect biomechanical membrane properties of P. falciparum-infected erythrocytes.* Commun Biol, 2019. **2**: p. 311.
156. Hosseini, S.M. and J.J. Feng, *How malaria parasites reduce the deformability of infected red blood cells.* Biophys J, 2012. **103**(1): p. 1-10.

157. Zhang, Y., et al., *Multiple stiffening effects of nanoscale knobs on human red blood cells infected with Plasmodium falciparum malaria parasite.* Proc Natl Acad Sci U S A, 2015. **112**(19): p. 6068-73.
158. Glenister, F.K., et al., *Contribution of parasite proteins to altered mechanical properties of malaria-infected red blood cells.* Blood, 2002. **99**(3): p. 1060-3.
159. Smith, E.W. and J.R. Krevans, *Clinical manifestations of hemoglobin C disorders.* Bull Johns Hopkins Hosp, 1959. **104**(1): p. 17-43.
160. Hill, A.V., et al., *Common west African HLA antigens are associated with protection from severe malaria.* Nature, 1991. **352**(6336): p. 595-600.
161. Agarwal, A., et al., *Hemoglobin C associated with protection from severe malaria in the Dogon of Mali, a West African population with a low prevalence of hemoglobin S.* Blood, 2000. **96**(7): p. 2358-63.
162. Cyrklaff, M., et al., *Hemoglobins S and C interfere with actin remodeling in Plasmodium falciparum-infected erythrocytes.* Science, 2011. **334**(6060): p. 1283-6.
163. Archer, N.M., et al., *Resistance to Plasmodium falciparum in sickle cell trait erythrocytes is driven by oxygen-dependent growth inhibition.* Proc Natl Acad Sci U S A, 2018. **115**(28): p. 7350-7355.
164. Fairhurst, R.M., et al., *Aberrant development of Plasmodium falciparum in hemoglobin CC red cells: implications for the malaria protective effect of the homozygous state.* Blood, 2003. **101**(8): p. 3309-15.
165. Fairhurst, R.M., et al., *Abnormal display of PfEMP-1 on erythrocytes carrying haemoglobin C may protect against malaria.* Nature, 2005. **435**(7045): p. 1117-21.
166. Carlson, J., et al., *Natural protection against severe Plasmodium falciparum malaria due to impaired rosette formation.* Blood, 1994. **84**(11): p. 3909-14.
167. Cholera, R., et al., *Impaired cytoadherence of Plasmodium falciparum-infected erythrocytes containing sickle hemoglobin.* Proc Natl Acad Sci U S A, 2008. **105**(3): p. 991-6.
168. Dasanna, A.K., et al., *Rolling Adhesion of Schizont Stage Malaria-Infected Red Blood Cells in Shear Flow.* Biophysical Journal, 2017. **112**(9): p. 1908-1919.
169. Gong, L., et al., *Biochemical and immunological mechanisms by which sickle cell trait protects against malaria.* Malar J, 2013. **12**: p. 317.
170. Taylor, S.M., C.M. Parobek, and R.M. Fairhurst, *Haemoglobinopathies and the clinical epidemiology of malaria: a systematic review and meta-analysis.* Lancet Infect Dis, 2012. **12**(6): p. 457-68.
171. Gerhardt, T. and K. Ley, *Monocyte trafficking across the vessel wall.* Cardiovasc Res, 2015. **107**(3): p. 321-30.
172. Sundd, P., et al., *Biomechanics of leukocyte rolling.* Biorheology, 2011. **48**(1): p. 1-35.
173. Middleton, J., et al., *Leukocyte extravasation: chemokine transport and presentation by the endothelium.* Blood, 2002. **100**(12): p. 3853-60.
174. Caputo, K.E. and D.A. Hammer, *Effect of microvillus deformability on leukocyte adhesion explored using adhesive dynamics simulations.* Biophys J, 2005. **89**(1): p. 187-200.
175. Helms, G., et al., *Modeling cytoadhesion of Plasmodium falciparum-infected erythrocytes and leukocytes—common principles and distinctive features.* FEBS Letters, 2016. **590**(13): p. 1955-1971.
176. Dembo, M., et al., *The reaction-limited kinetics of membrane-to-surface adhesion and detachment.* Proc R Soc Lond B Biol Sci, 1988. **234**(1274): p. 55-83.
177. Li, I.T.S., T. Ha, and Y.R. Chemla, *Mapping cell surface adhesion by rotation tracking and adhesion footprinting.* Scientific Reports, 2017. **7**: p. 44502.
178. Fu, P., P. Li, and Y. Hu, *A general numerical model of leukocyte adhesion in microchannels.* Int J Numer Method Biomed Eng, 2022. **38**(7): p. e3606.
179. Rieger, H., et al., *Cytoadhesion of Plasmodium falciparum-infected erythrocytes to chondroitin-4-sulfate is cooperative and shear enhanced.* Blood, 2015. **125**(2): p. 383-91.

180. Lubiana, P., et al., *Adhesion between P. falciparum infected erythrocytes and human endothelial receptors follows alternative binding dynamics under flow and febrile conditions.* Sci Rep, 2020. **10**(1): p. 4548.
181. Lim, Y.B., et al., *Single molecule and multiple bond characterization of catch bond associated cytoadhesion in malaria.* Scientific Reports, 2017. **7**(1): p. 4208.
182. Nash, G.B., et al., *Rheological analysis of the adhesive interactions of red blood cells parasitized by Plasmodium falciparum.* Blood, 1992. **79**(3): p. 798-807.
183. Yipp, B.G., et al., *Differential roles of CD36, ICAM-1, and P-selectin in Plasmodium falciparum cytoadherence in vivo.* Microcirculation, 2007. **14**(6): p. 593-602.
184. Fedosov, D.A., et al., *Multiscale modeling of red blood cell mechanics and blood flow in malaria.* PLoS Comput Biol, 2011. **7**(12): p. e1002270.
185. Fedosov, D.A., B. Caswell, and G.E. Karniadakis, *Wall shear stress-based model for adhesive dynamics of red blood cells in malaria.* Biophys J, 2011. **100**(9): p. 2084-93.
186. Dasanna, A.K. and U.S. Schwarz, *Adhesion-based sorting of blood cells: an adhesive dynamics simulation study.* Soft Matter, 2018. **14**(44): p. 9061-9070.
187. Lambros, C. and J.P. Vanderberg, *Synchronization of Plasmodium falciparum erythrocytic stages in culture.* J Parasitol, 1979. **65**(3): p. 418-20.
188. Goodyer, I.D., et al., *Purification of mature-stage Plasmodium falciparum by gelatine flotation.* Ann Trop Med Parasitol, 1994. **88**(2): p. 209-11.
189. Avril, M., et al., *DC8 and DC13 var genes associated with severe malaria bind avidly to diverse endothelial cells.* PLoS Pathog, 2013. **9**(6): p. e1003430.
190. Saha, K., F. Bender, and E. Gizeli, *Comparative study of IgG binding to proteins G and A: nonequilibrium kinetic and binding constant determination with the acoustic waveguide device.* Anal Chem, 2003. **75**(4): p. 835-42.
191. Boulanger, M.D., et al., *Bioaffinity-based surface immobilization of antibodies to capture endothelial colony-forming cells.* PLoS One, 2022. **17**(8): p. e0269316.
192. Wiegand, G., K.R. Neumaier, and E. Sackmann, *Microinterferometry: Three-Dimensional Reconstruction of Surface Microtopography for Thin-Film and Wetting Studies by Reflection Interference Contrast Microscopy (RICM).* Appl Opt, 1998. **37**(29): p. 6892-905.
193. Higaki, Y., et al., *Ion-Specific Modulation of Interfacial Interaction Potentials between Solid Substrates and Cell-Sized Particles Mediated via Zwitterionic, Super-Hydrophilic Poly(sulfobetaine) Brushes.* J Phys Chem B, 2017. **121**(6): p. 1396-1404.
194. Fish, K.N., *Total internal reflection fluorescence (TIRF) microscopy.* Curr Protoc Cytom, 2009. **Chapter 12**: p. Unit12.18.
195. Jötten, A.M., et al., *Blood group and size dependent stability of P. falciparum infected red blood cell aggregates in capillaries.* Biomicrofluidics, 2020. **14**(2): p. 024104.
196. Zhao, Y., A. Sarkar, and X. Wang, *Peptide nucleic acid based tension sensor for cellular force imaging with strong DNase resistance.* Biosens Bioelectron, 2020. **150**: p. 111959.
197. Tian, Q., P. Keshri, and M. You, *Recent developments in DNA-based mechanical nanodevices.* Chem Commun (Camb), 2022. **58**(30): p. 4700-4710.
198. Petrosyan, R., A. Narayan, and M.T. Woodside, *Single-Molecule Force Spectroscopy of Protein Folding.* J Mol Biol, 2021. **433**(20): p. 167207.
199. Ott, W., et al., *Single-molecule force spectroscopy on polyproteins and receptor-ligand complexes: The current toolbox.* J Struct Biol, 2017. **197**(1): p. 3-12.
200. Galera-Prat, A., et al., *Understanding biology by stretching proteins: recent progress.* Curr Opin Struct Biol, 2010. **20**(1): p. 63-9.
201. Sumbul, F. and F. Rico, *Single-Molecule Force Spectroscopy: Experiments, Analysis, and Simulations.* Methods Mol Biol, 2019. **1886**: p. 163-189.
202. Boehr, D.D., R. Nussinov, and P.E. Wright, *The role of dynamic conformational ensembles in biomolecular recognition.* Nat Chem Biol, 2009. **5**(11): p. 789-96.
203. Fernandez, J.M. and H. Li, *Force-clamp spectroscopy monitors the folding trajectory of a single protein.* Science, 2004. **303**(5664): p. 1674-8.

204. Willemsen, O.H., et al., *Simultaneous height and adhesion imaging of antibody-antigen interactions by atomic force microscopy.* Biophys J, 1998. **75**(5): p. 2220-8.
205. Schmitt, L., et al., *A metal-chelating microscopy tip as a new toolbox for single-molecule experiments by atomic force microscopy.* Biophys J, 2000. **78**(6): p. 3275-85.
206. Sagvolden, G., *Protein adhesion force dynamics and single adhesion events.* Biophys J, 1999. **77**(1): p. 526-32.
207. Jobst, M.A., et al., *Resolving dual binding conformations of cellulosome cohesin-dockerin complexes using single-molecule force spectroscopy.* Elife, 2015. **4**.
208. Johnson, K.C. and W.E. Thomas, *How Do We Know when Single-Molecule Force Spectroscopy Really Tests Single Bonds?* Biophys J, 2018. **114**(9): p. 2032-2039.
209. Merkel, R., et al., *Energy landscapes of receptor-ligand bonds explored with dynamic force spectroscopy.* Nature, 1999. **397**(6714): p. 50-3.
210. Koram, K., et al., *Population based reference intervals for common blood haematological and biochemical parameters in the akuapem north district.* Ghana Med J, 2007. **41**(4): p. 160-6.
211. Sowunmi, A., et al., *Therapeutic efficacy and effects of artemisinin-based combination treatments on uncomplicated Plasmodium falciparum malaria -associated anaemia in Nigerian children during seven years of adoption as first-line treatments.* Infect Dis Poverty, 2017. **6**(1): p. 36.
212. Hou, H.W., et al., *Deformability based cell margination--a simple microfluidic design for malaria-infected erythrocyte separation.* Lab Chip, 2010. **10**(19): p. 2605-13.
213. Chen, Y., et al., *Margination of Stiffened Red Blood Cells Regulated By Vessel Geometry.* Sci Rep, 2017. **7**(1): p. 15253.
214. Zhang, R., et al., *Rheopathologic Consequence of Plasmodium vivax Rosette Formation.* PLoS Negl Trop Dis, 2016. **10**(8): p. e0004912.
215. Kaul, D.K., et al., *Rosetting of Plasmodium falciparum-infected red blood cells with uninfected red blood cells enhances microvascular obstruction under flow conditions.* Blood, 1991. **78**(3): p. 812-9.
216. Adams, Y. and J.A. Rowe, *The effect of anti-rosetting agents against malaria parasites under physiological flow conditions.* PLoS One, 2013. **8**(9): p. e73999.
217. Long, M., et al., *Probabilistic modeling of rosette formation.* Biophys J, 2006. **91**(1): p. 352-63.
218. Ch'ng, J.H., et al., *Rosette-Disrupting Effect of an Anti-Plasmodial Compound for the Potential Treatment of Plasmodium falciparum Malaria Complications.* Sci Rep, 2016. **6**: p. 29317.
219. Deans, A.M. and J.A. Rowe, *Plasmodium falciparum: Rosettes do not protect merozoites from invasion-inhibitory antibodies.* Exp Parasitol, 2006. **112**(4): p. 269-73.
220. McQuaid, F. and J.A. Rowe, *Rosetting revisited: a critical look at the evidence for host erythrocyte receptors in Plasmodium falciparum rosetting.* Parasitology, 2020. **147**(1): p. 1-11.
221. Abkarian, M., et al., *A novel mechanism for egress of malarial parasites from red blood cells.* Blood, 2011. **117**(15): p. 4118-24.

Supplementary

Bead of 8 µm diameter with a-ICAM-1 (anti-human mouse) antibody at 0.03 Pa WSS in contact with ICAM-1 functionalized surface (100fps, RICM) (gif, scale bar 10 µm)

Flipping adhesion of trophozoite-stage parasitized HbAA erythrocyte onto ICAM-1 functionalized surface (100fps, RICM) (gif, scale bar 10 µm)

Sliding adhesion of trophozoite-stage parasitized HbAA erythrocyte onto ICAM-1 functionalized surface (100fps, RICM) (gif, scale bar 5 µm)

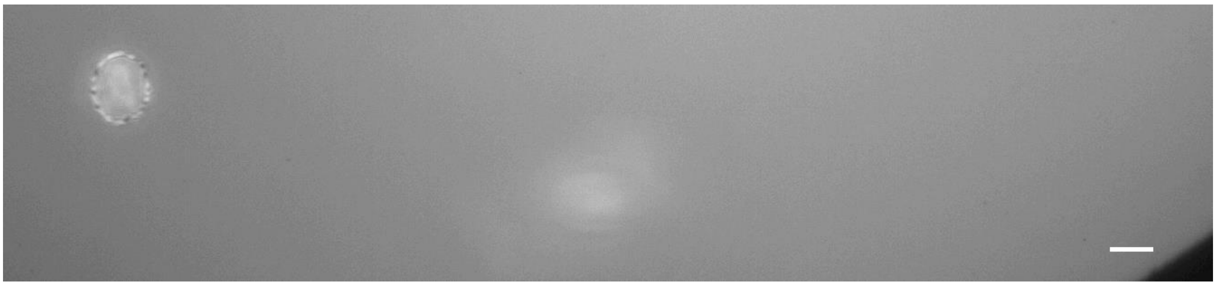

Rolling adhesion of schizont-stage parasitized HbAA erythrocyte onto ICAM-1 functionalized surface (100fps, RICM) (gif, scale bar 5 µm)

Flipping adhesion of trophozoite-stage parasitized HbAS erythrocyte onto ICAM-1 functionalized surface (100fps, RICM) (gif, scale bar is 5 µm)